UNIVERSITÀ DEGLI STUDI DI ROMA
"TOR VERGATA"

DOTTORATO DI RICERCA IN INGEGNERIA INDUSTRIALE

XXIX CICLO

Setup and Validation of High Fidelity Aeroelastic Analysis Methods Based on RBF Mesh Morphing

Ubaldo Cella

A.A. 2015/16

Docente Guida/Tutor : Prof. Marco Evangelos Biancolini
Coordinatore : Prof. Roberto Montanari

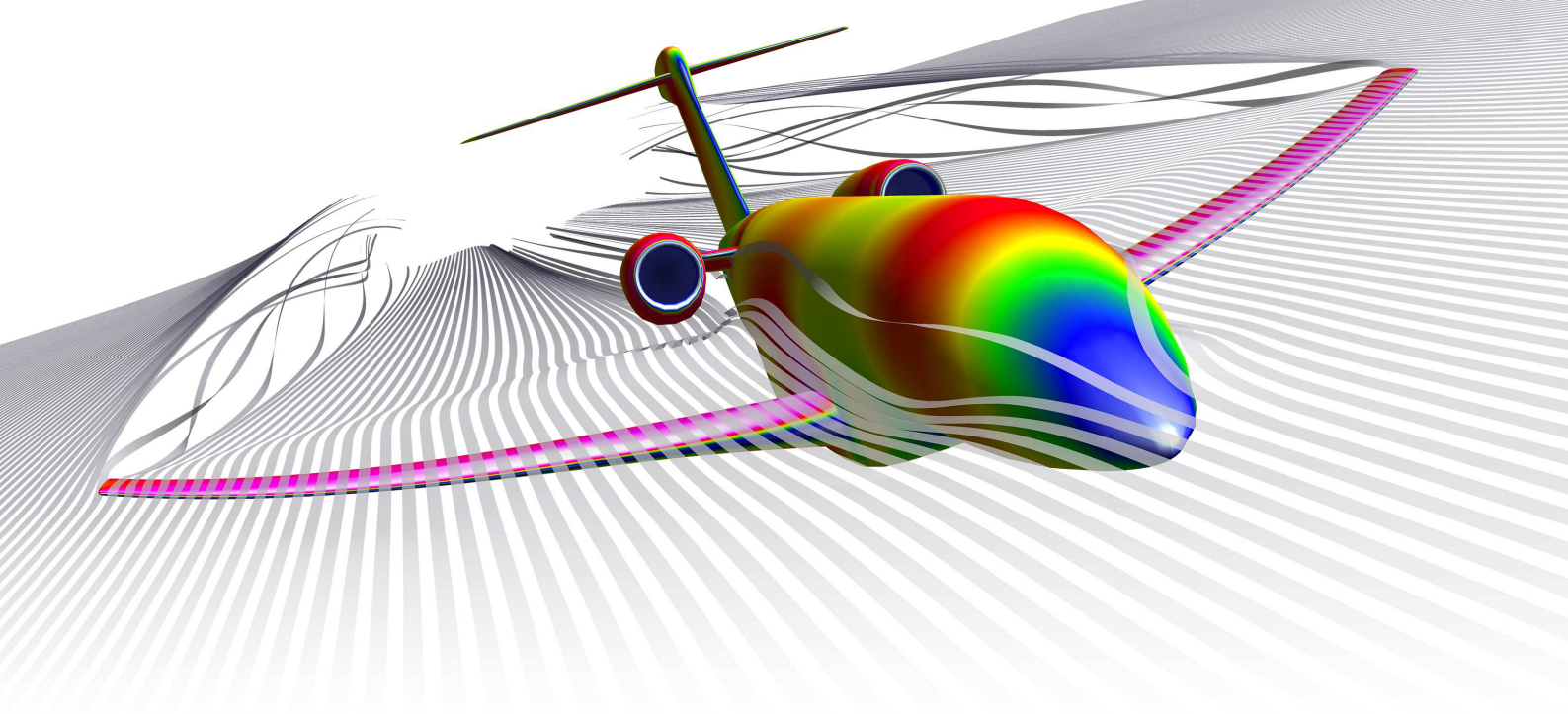

Setup and Validation of High Fidelity Aeroelastic Analysis Methods Based on RBF Mesh Morphing

Ph.D. thesis

Ubaldo Cella

Institution : University of Rome "Tor Vergata"
Program : Ph.D. in Industrial Engineering
Cycle : XXIX
Academic year : 2015/16
Supervisor : Prof. Marco Evangelos Biancolini
Coordinator : Prof. Roberto Montanari

Keywords: *Aeroelasticity, fluid-structure interaction, computational fluid dynamics, mesh morphing, radial basis functions,*

web: `www.designmethods.aero`
email: `ubaldo.cella@designmethods.aero`

Submitted January 2017 in partial fulfilment of the requirements for the degree of Doctor of Philosophy in Industrial Engineering at the University of Rome "Tor Vergata".

Typesetting system: LaTeX

"For every complex problem there is a simple solution, and it is the wrong one."

"Per ogni problema complesso esiste una soluzione semplice, ed è quella sbagliata."

George Bernard Shaw

Preface

The bases of the work here presented refer to a collaboration between the university of Rome "Tor Vergata" and the aircraft industry *Piaggio Aerospace* that began in 2009 and was aimed to the implementation of a CFD-CSM aeroelastic analysis procedure coupling the solvers in use in the company, *CFD++* for fluid dynamic and *Nastran* for structural analysis, by using the *RBF Morph* mesh morphing software as a link between the two environments. At that time *RBF Morph* was a novel solution, just appeared on the market, integrated as an add-on in the *ANSYS Fluent* solver. The task was then to verify its feasibility in implementing an FSI workflow outside the *ANSYS* environment and to test the efficiency of RBF mesh morphing as a coupling method for high fidelity aeroelastic analyses. It was one of the first steps in the development of the stand-alone tool that today is ready to be integrated with several solvers and that was, in recent years, the core technology of several European research programmes. Two EU aeronautics projects in particular (*RBF4AERO* and *RIBES*), constituted the developing framework of a technology platform aimed to extend the RBF mesh morphing application to problems ranging from shape optimization, ice accretion and FSI analyses involving commercial and open source tools. Within the *RIBES* project, furthermore, an experimental wing tunnel tests campaign for FSI numerical methods validation, aimed to cover aspects that are currently poorly covered by test cases available in literature, was setup and completed. The work here reported was developed, and funded, within this two projects.

Aim of this thesis is to demonstrate the capability of RBF mesh morphing to enhance the development of efficient high fidelity FSI analyses procedures by a 2-way and a modal superposition approach. The two methodologies are described detailing coupling procedures and workflows implementations. The quality of their solutions was assessed against two static experimental test cases: a complete aircraft model tested in transonic conditions (provided by *Piaggio Aerospace*) and the *RIBES* wind tunnel model consisting in a typical metal wing box equipped with a set of strain gauges able to provide the actual stress state of the wing under aerodynamic loads.

Ubaldo Cella

Messina, Italy
January 2017

Contents

List of Figures

List of Tables

Nomenclature

List of symbols

α	= angle of attack
$\bar{K}$	= modal stiffness
$\bar{M}$	= modal mass
β	= coefficient of the correction polynomial
ΔX	= modal displacements
δ	= direction cosine
ϵ	= normal strain
η	= coefficients vector of the fitted RBF
γ	= heat capacity ratio ≈ 1.4
μ	= dynamic viscosity
ν	= Poisson's ratio
Ω	= spectral matrix
ω_d	= damped circular frequency
ω_n	= natural circular frequency
ϕ	= principal stress direction
ρ	= fluid density
σ	= normal stress
τ_w	= wall shear stress
ε	= wing geometric twist
φ	= interpolating radial basis
ζ	= structural damping factor
C	= structural damping matrix
c	= mapping corrective coefficient
C_D	= drag coefficient

C_L = lift coefficient
C_P = pressure coefficient
d = mapping distance function
E = Young's modulus
F = force vector
f_n = natural frequency
G = vector of the scalar function to be interpolated
h = RBF correction polynomial
K = structural stiffness matrix
k = number of natural modes
M = structural mass matrix
m_T = total mass
N = number of interpolating points
P = constraint matrix used for RBF fit
p = modal participation factor
Q = nodal load
q = modal coordinate
R = universal gas constant = 287.05 $\left[\frac{J}{Kg \cdot K}\right]$
r = euclidean distance between two points
Re = Reynolds number
S = RBF based interpolating function
T = absolute temperature
t = time
U = interpolation matrix used for RBF fit
V = velocity
v = RBF displacement vector
W = smooth function for blending polynomial
w = mapping blending polynomial
X = modal shape
x = position vector in the Cartesian reference system
X_{CFD_0} = position of the CFD undeformed mesh nodes
X_{CFD} = position of the CFD mesh nodes
Y^+ = dimensionless wall distance

Acronyms and abbreviations

CAD	= Computer-Aided Design
CFD	= Computational Fluid Dynamics
CSM	= Computational Structural Mechanics
dc	= drag count ($C_D \cdot 10^4$)
DoF	= Degrees of Freedom
EAs	= Evolutionary Algorithms
EMPF	= Effective Mass Participation Factor
FCS	= Flight Control System
FEM	= Finite Element Method
FFD	= Free Form Deformation
FMM	= Fast Multi Pole Method
FSI	= Fluid-Structure Interaction
GUI	= Graphical User Interface
HPC	= High Performance Computing
LCM	= Local Correction Method
MAC	= Mean Aerodynamic Chord
MDO	= Multi-disciplinary design optimization
NURBS	= Non Uniform Rational Basis-Splines
POU	= Partition Of Unity
PSP	= Pressure-Sensitive Paint
RANS	= Reynolds Averaged Navier-Stokes
RBF	= Radial Basis Function
ROM	= Reduced Order Model

1

Introduction

Aeroelasticity is the subject that describes the interaction of aerodynamic, inertia and elastic forces for a flexible structure. A first schematic relation between the type of forces and the disciplines involved in the mechanism was proposed by Collar in 1946 with its well known *Triangle of Forces* [1]. In a more general view, aeroelastic phenomena are usually classified in two main categories: *static* and *dynamic*. Static aeroelasticity considers the non-oscillatory effects of aerodynamic forces (independent of time) acting on flexible structures. Dynamic aeroelasticity is concerned with the oscillatory effects of the aeroelastic interactions.

In aerospace engineering, the flexibility of structures plays a crucial role in several aspects of aircraft design processes [2]. In static conditions, the flexibility of the wing involves a direct coupling between structural deformations and aerodynamic forces. This mechanism causes a geometric shape modification of lifting surfaces under load with a consequent variation of lift distribution that leads to different static equilibriums for every steady flight condition. The capability to evaluate such interaction is important to avoid drag penalties in design conditions. The typical case of interest is the relationship between the so-called *"jig shape"* (the shape of the structure when supported in the jigs during manufacture) and *"flying shape"* (the shape that it will assume in the real in-flight conditions). For a theoretical rigid wing there would be no difference between the two shapes. For real structures the elastic deformation under aerodynamic loads causes the aircraft to exhibit performances that differ from what is expected assuming a rigid structure. If large wing bending occurs, for example, a high dihedral angle might be generated affecting also the aircraft lateral stability.

Static aero-structural interaction evaluation is also essential to account for potential influences on the effectiveness of control surfaces, aircraft trim behaviour and stability/control characteristics. It is, furthermore, crucial to account for two potentially dangerous phenomena: *divergence* and *control reversal*. The first occurs when the moments due to aerodynamic forces overcome the restoring moments due to structural stiffness, so resulting in risks of structural failure[1]. The latter affects the control system

[1]Typical examples are forward swept wings (with a traditional wing box structure) in which the

Figure 1.1: *In-flight shape of Boeing 787 Dreamliner wing under load (courtesy of ©Boeing).*

and occurs at speed conditions higher than a so called *reversal speed*. It is determined by the generation of a moment, induced by the action on the control surface, that is higher than the structural torsional response of the wing box. At reversal speed, the pitching moment of the wing is exactly cancelled out by the pitching moment generated by the action of the control surface [3]. At higher velocities the wing generates forces in the opposite direction respect to the direction expected by the action on the control surface causing a reversal operation of the command (e.g. to a pull up action on the command corresponds a diving response).

The link between aeroelasticity and loads is extended to the dynamic response of structures under steady and unsteady aerodynamic forces. The loads, resulting from flight manoeuvres, air gust or turbulence, interact with the aircraft vibration characteristics generating dynamic inertial and elastic forces. At some critical speeds, external air flow disturbances might trigger an unstable self-excited vibration in which a mode structure oscillation becomes negatively damped. Such phenomenon is called *flutter*. The unsteady nature of the aerodynamic forces and moments generated when the aircraft oscillates renders the prediction of the flutter mechanism a particular challenging task, especially in transonic regimes. The main area of interest of dynamic aeroelasticity is the study of such potentially catastrophic phenomena.

Another mechanism that is important to account for, particularly in highly flexible aircrafts subjected to large deformations, is the interaction between the aircraft vibration modes and the flight control system (FCS). This coupling represents a closed loop that affects both the aeroelastic and loads behaviour and can involve unfavourable interaction that might seriously degrade the control system efficiency [4]. The discipline that study such a mechanism is called *aeroservoelasticity*.

1.1 The Fluid Structure Interaction (FSI) problem

The history of aeronautics is dominated, from the early begin, by the phenomenon of aeroelasticity although it was still completely unknown to the pioneers of aviation. As often happens in many fields of engineering, the effort in deepening the investigation of an emerging phenomenon is motivated by the fear of potential damage or, in the worst case, as consequence of catastrophic events. The evolution of aviation is, un-

effect of bending under load produces an increase in the local angle of attack that further increments the aerodynamic loading.

fortunately, marked along its path by several disasters that, on the other hand, signed some of the major improvements in its technology. The moment at which engineers began to fair the effects of structures flexibility is probably associated to the in-flight wing box (dramatic) failure of the Fokker D.VIII during the First World War[2]. The importance of an interdisciplinary design approach in aircrafts design became then evident very soon. Aerodynamic design and aeroelasticity have been, however, historically treated separately in industry up to recent years. The aeroelastic verification was often demanded to the final stage of the design process or adopted to face problems appeared during flight testing. The problems were traditionally solved by stiffening the structure and/or by masses balancing.

Figure 1.2: *Fokker D.VIII (source Wikipedia).*

A milestone in the development of numerical tools to study aeroelastic problems is represented by the Theodorsen's flutter theory (1935) [6]. The experimental support to the validation of analytical methods progressed in parallel. The first wind tunnel constructed for exclusive use in flutter research became operational at NACA Langley Research Centre in 1945 [7].

The year 1965 is considered as the begin of the Computational Fluid Dynamics era [8]. The adoption of Vortex Lattice Method, during 1960s, made it possible to begin to model the aeroelastic behaviour of aircrafts in complete configuration [9]. Today several methods are available for every stage of aircrafts design process. In [10] a review of numerical techniques to face FSI problems and an extended reference list are provided and discussed. One of the classical approach involves the modal and the influence coefficient techniques, valid for attached flows and for aerodynamic loads in phase with the deformations [11]. Linear aerodynamic methods, as doublet-lattice [12] provide a robust approach for unsteady aerodynamics although simpler models, based on strip theory and indicial functions, are widely used at conceptual levels [13].

[2]The army technical bureau requested a modification to the original design imposing to reinforce the rear spar with proportional strength capacity to the front spar. This redistribution of stiffness caused a torsional divergence under flight loads [5].

The latter approaches are computationally inexpensive but neglect 3D flow physics (as wing-tip vortices and aerodynamic interference between wake and bodies). Where the linear assumption is not valid, as in transonic regimes or if large deformation occurs, corrections based on CFD or test results can be applied [14]. A set of examples, in which non-linear problems were solved implementing a FEM model of solid isotropic thin-walled structures within a RANS solver, are provided in [15].

The use of RANS solvers for steady and unsteady aeroelastic simulations have significantly increased in recent years and represents today the most accurate approach. In [16] a fully non-linear unsteady FSI procedure, that couples the *Y3D* deformable solid model finite-discrete element code with an adaptive finite element CFD solver based on the open-source *Fluidity* code, is proposed. Other examples of its application to multiphase fluid problems, involving free surface and floating bodies, are presented in [17]. The relatively expensive computational requirements of RANS methods constitutes, however, the main limitation to their adoption in more demanding applications (e.g. in modelling complex dynamic systems and/or in the integration within numerical optimization environments). In such cases Reduced Order Models (ROM) can be used in place of RANS solutions to lower the computational burden. ROMs use some limited results of high fidelity simulation models to provide a simpler mathematical representation of the physical phenomenon to be examined [18]. The aim is to be able to capture the most relevant behaviour of the system reducing its number of degrees of freedom (for this reason they are often also called "*low dimensional models*" [19]) thus providing a faster and computationally cheaper aeroelastic model.

In the present work we focus the attention on high fidelity methods and in particular on the crucial aspects related to the numerical coupling between fluid dynamic and structural solutions.

1.1.1 High fidelity approach for FSI

"*High fidelity*" simulations mimic the physics of phenomena with a greater accuracy with respect to "*low fidelity*" simulations. This higher accuracy has a cost. The confidence on such cost, on methods accuracy and on the balance between these two qualities, is important to proper select the opportune numerical tool with respect to the stage of the design process [20]. The possibility to adopt high fidelity analyses in earlier stages of aircrafts design provides the possibility to limit the uncertainness to be expected in the test phase and helps to reduce the time to market of the product [21].

The *state of the art* in FSI analysis numerical methods consists in approaching the problem coupling RANS codes with FEM solvers. The critical point relates to the strategy to be adopted in implementing the exchange of information between the two environments. In this work two static analysis methods, based on the use of CFD and FEM solvers, are proposed. The first couples the two solvers in the so called "*2-way*" procedure in which the aerodynamic solution, in terms of forces acting on wet surfaces, and the geometric displacement of the structure under load, are iteratively exchanged between the codes up to the convergence to an equilibrated static condition. The second method is based on the implementation of an intrinsically aeroelastic CFD configu-

ration in which the FEM solver is used to extract the vibrating modal shapes of the structure that are used to implement a parametric CFD domain.

2-way FSI analysis

The implementation of CFD-CSM (Computational Fluid Dynamic - Computational Structural Mechanics), or 2-way FSI procedures, might be quite complex and solver-dependent. The codes coupling requires several actions: solutions extraction, files format conversion, setup update, run management, solutions quality check, etc. If the analysis has to be included in an optimization loop, routines controlling the procedure in an automatic process have to be implemented. The main issues, however, are related to the efficient and accurate bidirectional coupling of the aerodynamic and the structural solution. Two technical aspects are particular awkward: the transfer of the CFD solution, in form of loads, to the FEM model and the adaptation of the CFD domain according to the displacement estimated by the FEM analysis.

CFD to FEM - Fluid dynamic and finite elements methods solve different regions generated with different discretization criteria that, in general, do not match on the common boundaries (the wet surfaces). The two solutions (structure displacements and aerodynamic loads) are then distributed on non-matching clouds of points belonging to common boundaries for which the mathematical definition of the surfaces is missing. An interpolation of solutions between the domains is then required. During the mapping process of the CFD aerodynamic forces (surface pressure and shear stresses) as loads into the FEM model, an error is, in general, introduced.

FEM to CFD - The computed structural displacement has to be used back in the CFD solver to close the 2-way loop. The adaptation of the fluid dynamic domain to the deformed shape (an action that has to be performed for every cycle of aerodynamic loads evaluation) is efficiently approached by mesh morphing techniques. Such process can degrade the quality of the computational grid and requires efficient algorithms.

Modal FSI analysis

The idea at the base of the adoption of the modal approach for FSI analysis is the simplifying assumption that the displacement of the geometry under the aerodynamic loads can be replicated by a combination of a limited number of structural natural modal shapes. The implementation of *"modal superposition"* FSI methods begins then with a preliminary structural modal analysis of the object under investigation. This action is performed only once and no further involvement of FEM solvers is required. The aim is to avoid the iteration between CFD and FEM analysis by the development of a fluid dynamic model that, with an opportune parametrization of the mesh, becomes intrinsically aeroelastic. The elasticity effect is taken into account directly within the CFD environment using a basis of structural modal shapes whose combination is used as target shape to deform the mesh. Applying the modal approach many of the complexities related to the CFD-CSM implementation, with the exception of the domain

adaptation problem whose awkwardness remains unchanged with respect to the 2-way FSI coupling, are then bypassed. Furthermore the possibility of retaining the geometric adaptation within the progress of the CFD computation, in conjunction with the possibility of controlling the mesh update frequency, supports the improvement of robustness and efficiency of the procedure. The latter aspect assumes significant relevance when dealing with the setup of automatic procedures.

Mesh Morphing Method

The problem of efficiently updating numerical domains acquires particular importance, beside FSI analyses, with the modern tendency of addressing engineering design problems by implementing multidisciplinary shape optimization (MDO) environments. Mesh morphing tools are, in fact, excellent candidates to perform shape parameterization [22].

Morphing is the ability to change one thing into another smoothly. *Mesh morphing* is, in a discretized numerical representation, the action of changing the shape of a meshed domain while preserving the topology.

Several techniques to approach this task, mainly based on the free-form deformation (FFD) [23] and the elastic models [24], are proposed in both research and commercial codes. Radial basis functions (RBFs) have become a well-established tool to interpolate scattered data [25] and are considered one of the most efficient mathematical framework to face the problem of mesh morphing. RBF morphing strategy is the one adopted for updating the fluid dynamic computational domain in both 2-way and modal FSI analysis procedures proposed in this work.

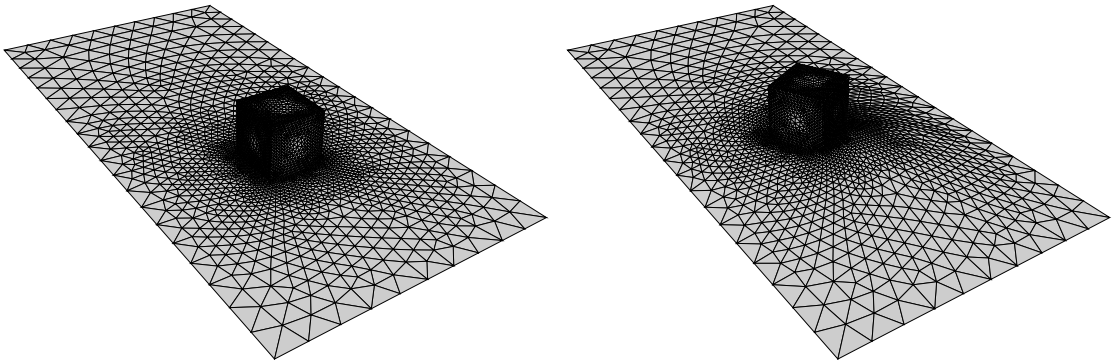

Figure 1.3: *Behaviour of mesh morphing.*

RBFs have been successfully applied in many research and academic activities. An example of the great potentialities of RBFs for mesh morphing is reported in [26] with an application on the parametrization and optimization of the shape of a wing. The ability to embed structural modes into a CFD model for transient coupled CFD analyses using RBFs has been proven by van Zuijlen et al. [27] on the AGARD 445.6 wing test case.

The first commercial mesh morphing tool based on radial basis functions was *RBF Morph*[3]. It was first developed as an on-demand module for a Formula 1 top team and then placed on the market as an add-on for the CFD solver *ANSYS Fluent* [28]. The code proved its efficiency in several aerospace [29] and non aerospace applications [30, 31]. A comprehensive description of the theory behind the tool and further examples of its application are given in [32]. *RBF Morph* is the tool used in the implementation of the CFD domain adaptation tasks performed in the FSI methodologies described in this work. The structural analyses were performed using *FEMAP/NX Nastran* while the fluid dynamic solutions were obtained by *ANSYS Fluent*.

1.2 Research contest of the work

The work here presented was developed (and funded) within the *RBF4AERO* and *RIBES* EU research projects, focused on aeronautical technologies, in which the university of Rome "Tor Vergata" was involved.

Figure 1.4: *Logos of the framework research projects.*

Object of *RBF4AERO*[4] was the development of a benchmark technology numerical platform for aircrafts design setting up methodologies based on RBF mesh morphing techniques [33]. The platform enables to solve relevant aircrafts design problems as FSI analysis [34], icing growth [35] and shape optimization combining adjoint and evolutionary based algorithms (EAs) [36, 37]. *RBF4AERO* was concluded November 2016.

The main topic of the *RIBES*[5] project was the reduction of the uncertainness in the CFD-CSM aeroelastic analysis numerical methodologies [38]. In addition, the project was addressed to the implementation of an RBF based workflow for shape structural optimization and to the experimental validation of FSI methodologies.

[3] `www.rbf-morph.com`

[4] *RBF4AERO* (`www.rbf4aero.eu`) was partially funded by the European Union 7th Framework Programme (FP7-AAT, 20072013) under Grant Agreement no. 605396.

[5] The *RIBES* project (`www.ribes-project.eu`) was led by the university of Rome "Tor Vergata" and was funded within the EU 7th FP programme by the aeronautics programme JTI-CS-GRA (Joint Technology Initiatives - Clean Sky - Green Regional Aircraft) under Grant Agreement no. 632556.

The topics of the *RIBES* project were:

1. the development of an accurate and efficient load mapping procedure to transfer solutions from fluid dynamic to structural solvers;
2. the implementation of a structural shape optimization tool;
3. the setup of an aeroelastic experimental campaign for FSI methodologies validation purposes.

A significant part of the budget was allocated on the setup of the wind tunnel experimental campaign. In this task an extensive sets of aeroelastic measurements, using an opportunely designed wing model with a typical metallic aeronautical wing box structure, was performed. The *RIBES* project was officially completed December 2016.

1.3 Validation of static aeroelastic analyses

The 2-way and the modal approaches to face the FSI problem previously introduced were implemented and validated against two proprietary aeronautical experimental test cases in static conditions. This document details the implemented methods, describes the adopted validation procedures and highlights the solutions of the assessments by a deep analysis of the experimental comparisons.

The test cases used for validation refer both to aircraft wings but have different characteristics. The first consists of a transonic wind tunnel model of an aircraft, in complete configuration, for which pressure and forces measurements are available in several conditions around the cruising Mach number. It refers to a program carried out by *Piaggio Aerospace* and was the base of a collaboration with the University of Rome "Tor Vergata" that began in 2009 and continued as a partnership within the *RBF4AERO* project. Its swept back wing configuration offers the possibility to asses the capability of the numerical methods to capture the coupling mechanism between aerodynamic performance and structural deformation. This assessment is than mainly addressed on the aerodynamic verification. The second test case refers to a half wing wind tunnel model, developed within the *RIBES* project by the University of Rome "Tor Vergata" in collaboration with the University of Naples "Federico II", that replicates a traditional metal wing box structure. No sweep angle is present, in this case, so no significant aerodynamic performance variation due to deformation is expected. The test case was expressly setup to provide a base of assessment for the elastic response of the structure. It is, in fact, instrumented with a set of strain gauges located in several points of the wing box structure.

Both comparisons are aimed to the absolute quantification of the accuracy of the 2-way method and to give the sensitivity on how the modal modelling represents a reasonable and practicable simplification in terms of estimation of geometric deformations.

2

Theoretical background

The aeroelastic methods here described approach the problem by coupling CFD and FEM solvers and by implementing a modal based FSI analysis within the fluid dynamic environment. In the CFD-CSM coupling, the module used to transfer the loads from the fluid dynamic solution to the finite element domain consists in a procedure implemented within the *RIBES* project. The modal approach is based on a preliminary structural modal analysis from which a number of natural modes are selected to be used in the creation of a parametric representation of the fluid dynamic domain. In both 2-way and modal methods, the CFD grid modification problem is solved adopting a mesh morphing tool based on Radial Basis Functions. A brief review of theoretical backgrounds on the Radial Basis Functions mathematical framework, a synthesis on structural modal analysis basics and a description of the RIBES load mapping procedure will be following provided.

2.1 Radial Basis Functions

Radial Basis Functions were born as interpolation methods for scattered data. They are very powerful tools able to interpolate, everywhere in the space, a function defined by discrete points [39, 40]. They are efficiently used to produce a mesh movement/morphing (for both surface shape changes and volume mesh smoothing) from a list of source points and their displacements[1].

The interpolating function S composed by RBFs, defining the motion of an arbitrary point inside or outside a domain (interpolation/extrapolation), is expressed as the linear combination of the radial contribution of each source point (if the point falls inside the domain of influence) by

$$S(x) = \sum_{i=1}^{N} \eta_i \varphi \left(\| x - x_i \| \right) + h(x)$$

[1] RBF can be used to fit scalar functions defined in a generic n-dimensional spaces providing a very effective interpolation tool for the evaluation, for instance, of Response Surfaces.

where

- φ is the selected interpolating radial basis;
- N is the total number of contributing source points (also called *centres*);
- $x_i = \{x_i, y_i, z_i\}$ is the vector of source points positions;
- $\eta_i = \{\eta_1, \ldots, \eta_N\}^T$ is a vector of unknown coefficients;
- h is a correction polynomial.

The correction polynomial h has order $m-1$, where m is the order of the radial basis φ. It is required to guarantee the uniqueness of the solution and the ability to execute rigid motions. The Euclidean distance between two points $r = \| x - x_i \|$ is defined in a generic n-dimensional space ($n = 2, 3$ for surface or volume mesh morphing applications). The radial contribution of each source point is specified without any special assumptions on their number or geometric position. This characteristic renders the formulation *"meshless"*.

A linear system (of order equal to the number of source points introduced) needs to be solved for the calculation of coefficients η_i. A radial basis fit exists if the coefficients and the weights of the polynomial h can be found such that the two following conditions are satisfied:

1. the value of $S(x_i)$ assumes the desired value at the point x_i.

$$S(x_i) = G(x_i), \qquad 1 \leq i \leq N$$

2. the system is completed if the orthogonality condition of the polynomial terms are verified for all polynomials p with a degree less or equal to that of polynomial h

$$\sum_{i=1}^{N} \eta_i p(x_i) = 0$$

The minimal degree of polynomial h depends on the choice of the RBF. A unique interpolant exists if the basis function is conditionally positive. If it is of order $m \leq 2$, the following linear polynomial can be used in a three-dimensional space:

$$h(x) = \beta_1 + \beta_2 x + \beta_3 y + \beta_4 z$$

A consequence of using a linear polynomial is that rigid body translations are exactly recovered.

The values for the coefficients η_i of RBF and the coefficients β of the linear polynomial can be obtained by solving the linear system (of order $N + 4$):

$$\begin{pmatrix} U & P \\ P^T & 0 \end{pmatrix} \begin{pmatrix} \eta \\ \beta \end{pmatrix} = \begin{pmatrix} G \\ 0 \end{pmatrix}$$

where

- $G = \{G_1, \ldots, G_N\}^T$ are the know values of the interpolating function at the source points;
- $\beta = \{\beta_1, \ldots, \beta_N\}^T$ are the coefficients of the polynomial h;
- U is the interpolation matrix (of dimension $N \times N$), defined calculating all the radial interactions between source points

$$U_{ij} = \varphi\left(\| x_i - x_j \|\right), \qquad 1 \leq i \leq N, \quad 1 \leq j \leq N$$

- P is a constraint matrix (of dimension $N \times 4$) that contains a column of ones and the x_i coordinates of source points in the others three columns[2]

$$P = \begin{pmatrix} 1 & x_1 & y_1 & z_1 \\ 1 & x_2 & y_2 & z_2 \\ \vdots & \vdots & \vdots & \vdots \\ 1 & x_N & y_N & z_N \end{pmatrix}$$

The process of deformation through the RBF expects to move each point individually according to the chosen interpolating function. The displacements along the three coordinates are governed by the following system:

$$\begin{cases} v_x = S_x(x) = \sum_{i=1}^{N} \eta_{x_i} \varphi\left(\| x - x_i \|\right) + \beta_{x_1} + \beta_{x_2} x + \beta_{x_3} y + \beta_{x_4} z \\ v_y = S_y(x) = \sum_{i=1}^{N} \eta_{y_i} \varphi\left(\| x - x_i \|\right) + \beta_{y_1} + \beta_{y_2} x + \beta_{y_3} y + \beta_{y_4} z \\ v_x = S_z(x) = \sum_{i=1}^{N} \eta_{z_i} \varphi\left(\| x - x_i \|\right) + \beta_{z_1} + \beta_{z_2} x + \beta_{z_3} y + \beta_{z_4} z \end{cases}$$

The behaviour of the function (and smoothness) between points depends on the kind of basis adopted. Several formulations of RBFs exist in literature. Typical RBFs, with global and compact support, are listed in Table 2.1.

The radial basis method has several advantages that make it very attractive for mesh smoothing and is considered one of the best mathematical tool to perform this task.

RBF mesh morphing is a meshless method - only grid points are moved regardless of which elements are connected (it is not necessary to store any information about the connectivity property of the mesh).

RBF system solution is suitable for parallel implementation - once the solution is known and shared in the memory of each cluster node, each partition has the ability to

[2]The control points should not be contained in the same plane otherwise the interpolation matrix would be singular.

smooth its nodes without taking care of what happens outside (high scalability) implicitly guaranteeing the continuity at interfaces.

RBF morphing action exactly prescribes known deformations - Surfaces are displaced exactly according to a known deformation. This effect is achieved by using all the mesh nodes as RBF centres with prescribed displacements, including the simple zero field to guarantee that a surface is left untouched by the morphing action.

Table 2.1: *Typical Radial Basis Functions.*

RBF with global support	$\varphi(r), r = \| r \|$
Spline type (R_n)	$r^n, n\ odd$
Thin plate spline (TPS_n)	$r^n \log(r), n\ even$
Multiquadric (MQ)	$\sqrt{1+r^2}$
Inverse multiquadric (IMQ)	$\frac{1}{\sqrt{1+r^2}}$
Inverse quadratic (IQ)	$\frac{1}{1+r^2}$
Gaussian (GS)	e^{-r^2}
RBF with compact support	$\varphi(r) = f(\xi), \xi \leq 1, \xi = \frac{r}{R_{sup}}$
Wendland (C^0)	$(1-\xi)^2$
Wendland (C^2)	$(1-\xi)^4(4\xi+1)$
Wendland (C^4)	$(1-\xi)^6(35\xi^2+18\xi+3)$
Wendland (C^6)	$(1-\xi)^8(32\xi^3+25\xi^2+8\xi+1)$

2.2 Structural modal analysis

Modal analysis is the study of the dynamic properties of structures under vibrational excitation [41]. Its goal is the determination of the undamped natural modes shapes and frequencies of a mechanic system during free vibration. It is applicable to both continuum and discrete systems (as FEM models) under the linear hypothesis. A continuum structure has an infinite number of modes while a discrete system has a number of modes equal to the number of degrees of freedom.

Mode shapes are the patterns the system assumes during vibration at specific natural frequencies.

Natural frequencies are the frequencies at which the structure would tend to naturally vibrate when subjected to a disturbance.

Modes are inherent properties of a mechanical system. They are determined by material properties and structural boundary conditions. Any variation of the structural properties (material, masses distribution, damping and stiffness) would alter both modal shapes and frequencies. The vibrational characteristics of a structure can then be controlled at design stage. In aeronautics, for instance, the definition of masses distribution and/or structure composite plies layout, linked to an opportune aerodynamic design[3], is adopted to delay instability phenomena as divergence or flutter onset.

The transient dynamic motion of a system with n degree of freedom is governed by the following second-order differential equations system:

$$[M]\{\ddot{x}\} + [C]\{\dot{x}\} + [K]\{x\} = \{F(t)\} \tag{2.1}$$

where $[M]$, $[C]$ and $[K]$ are respectively the mass, the damping (viscous) and the stiffness matrix. $\{\ddot{x}\}$, $\{\dot{x}\}$ and $\{x\}$ are respectively the nodal acceleration, velocity and displacement vector at a specific time t. $\{F(t)\}$ is the load vector of the time dependent forces that are applied to the system.

For modal analysis, a special case in which $\{F\} = 0$ (free vibration) and $[C] = 0$ (undamped condition), has to be solved. The equation 2.1 reduces then to the following free-vibration representation of the structural motion:

$$[M]\{\ddot{x}\} + [K]\{x\} = 0 \tag{2.2}$$

The response of this system, in function of time, is assumed to be harmonic and can be expressed in the form

$$\{x\} = \{X\}\sin(\omega_n t) \tag{2.3}$$

where $\{X\}$ is the eigenvector, or mode shape, and ω_n is the circular (or rotational) natural frequency (proportional to the natural frequency, $\omega_n = 2\pi f_n$).

Substituting the equation 2.3 in 2.2, after some passages is possible to obtain the eigenvalue problem

$$\left([K] - \omega_n^2[M]\right)\{X\} = \{0\}$$

[3] A typical example is the positioning of the engine nacelle. Its advanced position respect to the elastic axes of the wing box has a stabilizing effect. Under gust, for instance, having the centre of gravity of the engine forward of the wing induces a torsional moment which reduce the angle of incidence, and hence the wing load. A similar stabilizing effect, on static divergence, is generated by adopting a backward sweep angle [42].

which has a solution if the matrix $\left([K]-\omega_n^2[M]\right)$ is singular. This condition represents the form of the general eigenproblem where ω_n^2 is an eigenvalue.

If $[K]$ and $[M]$ are definite positive, the number of non-zero ω_{n_i} (with $i = 1 \dots k$) is equal to the number of DoF of the system. The vector $\{X_i\}$, corresponding to the circular frequency ω_{n_i}, is an eigenvector that corresponds to the i^{th} natural mode shape of the structure. Since the solution of the eigenvalue problem is a subspace of eigenvectors problem, the sign and the entity of each eigenvector may change depending on the algorithm adopted for the solution achievement.

The eigenvalue system can be solved numerically according to many methods. The most commonly adopted is the *Lanczos method* [43], which allows eigensolutions with eigenfrequencies to be extracted in ascending order.

An important result of the modal theory is the spectral decomposition. Eigenvectors (modes), corresponding to different circular frequencies, are orthogonal with respect to both structural stiffness and mass matrices. The following relationship is then valid:

$$\{X_j\}^T[M]\{X_i\} = \{X_j\}^T[K]\{X_i\} = \{0\}, \qquad i \neq j$$

that means that eigenvectors are linearly independent. This characteristic suggests to introduce a new reference system in which the equations can be uncoupled so that the contribution of each mode to the structure deformation is isolated.

Another important characteristic of natural modes is that the scaling or magnitude of the eigenvectors is arbitrary because they are an intrinsic characteristic of the structure. It means that they do not change in shape, when vibrating, but only in amplitude.

For solution purposes a convenient normalization, imposing for each mode $\{X_i\}$ a unit modal mass, is adopted

$$\{X_i\}^T[M]\{X_i\} = 1$$

and a definition of modal coordinates (or displacements) vector $\{q\}$ is introduced

$$\{q\} = [X]^{-1}\{x\} \tag{2.4}$$

$[X]$ is the modal matrix whose columns are the eigenvectors normalized with respect to mass and for which the following relation is assumed to be valid:

$$[X]^T[M][X] = [I] \tag{2.5}$$

For the stiffness matrix the following relationship is satisfied

$$[\Omega] = [X]^T[K][X] = \begin{pmatrix} \omega_{n_1}^2 & 0 & \cdots & 0 \\ 0 & \omega_{n_2}^2 & \cdots & 0 \\ \vdots & \vdots & \ddots & \vdots \\ 0 & 0 & \cdots & \omega_{n_k}^2 \end{pmatrix}$$

The matrix $[\Omega]$, known as *spectral matrix*, is populated with the eigenvalues along the diagonal and with zeros in the other positions.

Substituting the equation of the modal coordinates vector (eq. 2.4) in the general formulation of the equations system of motion (eq. 2.1), multiplying both terms by $[X]^T$ and including the relation 2.5, we obtain

$$[I]\{\ddot{q}\} + [X]^T[C][X]\{\dot{q}\} + [\Omega]\{q\} = [X]^T\{F(t)\} \tag{2.6}$$

To uncouple the equations system 2.6, the matrix $[X]$ is required to be such to make the matrix $[C]$ diagonal. This assumption can be satisfied if $[C]$ can be expressed as a linear combination of the structural mass and stiffness matrices.

$$[C] = (a[M] + b[K])$$

Each equation of the system 2.6 can then be posed in the uncoupled form

$$M_{ii}\ddot{q}_i + C_{ii}\dot{q}_i + K_{ii}q_i = F_i(t)$$

that, for convenience, is usually expressed as

$$\ddot{q}_i + 2\zeta_i\omega_{n_i}\dot{q}_i + \omega_{n_i}^2 q_i = \frac{F_i(t)}{M_{ii}} \tag{2.7}$$

where ω_{n_i} and ζ_i are respectively the rotational frequency and the damping factor

$$\omega_{n_i} = \sqrt{\frac{K_{ii}}{M_{ii}}}, \qquad \zeta_i = \frac{C_{ii}}{2M_{ii}\omega_{n_i}}$$

Modal participation factors

Consider a multi DoF system excited by the translational motion of the constraints and chose the relative displacements between the various masses and the supporting points to describe its motion. The equation of motion can be written in terms of modal coordinates as [44]

$$[M][X]\{\ddot{q}\} + [K][X]\{q\} = -[M]\delta_x\ddot{x}_A - [M]\delta_y\ddot{y}_A - [M]\delta_z\ddot{z}_A + \{f(t)\} \tag{2.8}$$

where x_A, y_A and z_A are the components of the displacement of the rigid frame and the terms δ_x, δ_y and δ_z are simply the direction cosines of the displacement.

If the modal matrix $[X]$ is not obtained by normalizing the mode vectors $\{X_i\}$ with the modal mass, the expressions of modal mass $[\bar{M}]$ and modal stiffness $[\bar{K}]$ matrix are

$$[\bar{M}] = [X]^T[M][X] \tag{2.9}$$

$$[\bar{K}] = [X]^T[K][X] \tag{2.10}$$

Multiplying all terms of equation 2.8 by matrix $[X]^T$ and considering equations 2.9 and 2.10, we can write

$$[\bar{M}]\{\ddot{q}\} + [\bar{K}]\{q\} = -p_x\ddot{x}_A - p_y\ddot{y}_A - p_z\ddot{z}_A + [X]^T\{F(t)\}$$

where

$$p_\xi = [X]^T[M]\delta_\xi, \qquad \xi = x, y, z$$

The terms p_ξ are called *modal participation factors*. The higher their value in a certain direction, the more that mode is excited by a motion of the supports in that direction.

When studying the response to an excitation due to the motion of the supporting points, it is usually sufficient to consider the few modes characterized by a high value of the corresponding modal participation factor.

Modal participation factors give a measure of how much of the mass of the system participates in the ith mode when the system is excited by a motion of the supporting frame in the relevant direction. It can be demonstrated, in fact, that the total mass of the system can be expressed as

$$m_T = p_\xi^T[\bar{M}]^{-1}p_\xi \tag{2.11}$$

The modal mass matrix is diagonal, and thus the equation 2.11 can be written in the form

$$m_T = \sum_{i=1}^{k}\left(\frac{p_{\xi_i}}{\{\bar{M}\}_i}\right)$$

Often ratios $\frac{p_{\xi_i}}{\{\bar{M}\}_i}$, also known as *effective mass participation factors*, are expressed as percentages of mass m_T and are used instead of the modal participation factors to provide a measure of the energy contained within each resonant mode. They represent the amount of system mass participating in a particular mode.

2.2.1 Modal superposition for static FSI analysis

In static aeroelastic problems approached by modal superposition, a simplified formulation of the modal theory can be adopted.

An aeroelastic phenomenon is considered *static* if the velocity of deformation of the system is higher than the velocity with which the loads are applied.

If the modal coordinates are not time depending, the equation 2.7 can be simplified in:

$$\omega_{n_i}^2 q_i = \frac{F_i}{M_{ii}} \tag{2.12}$$

Combining the equation 2.4 and 2.12

$$\{x\} = \sum_{i=1}^{k} \{X_i\} q_i = \sum_{i=1}^{k} \{X_i\} \frac{F_i}{M_{ii}\omega_{n_i}^2} \tag{2.13}$$

The modal forces F_i are, in FSI phenomena, associated to the aerodynamic resultants which, in a numerical analysis, correspond to the CFD loads related to pressure and shear stresses[4].

The equation 2.13 states that the deformation of the whole system is expressed as a combination of the modes weighted by the modal coordinates which are expressed as

$$q_i = \frac{F_i}{M_{ii}\omega_{n_i}^2}$$

The complete solution of the eigenvalue problem, can be approximated by retaining only a smaller set of lower modes with a substantial reduction in the number of degrees of freedom. This assumption is valid because mechanical systems are characteristically low-pass which means that the lowest frequency modes have the highest energy levels and are then physically prominent. This operation is called modes truncation. The minimum number of modes to retain depends on the system to be solved.

2.2.2 Formulation for unsteady FSI modal analysis

In case the phenomenon under investigation cannot be considered static, no simplification on the equation 2.7 can be adopted. Its unsteady formulation can be written as follows [41]:

$$\begin{aligned} q(t) = e^{-\zeta\omega_n t}\left[q_0 \cos(\omega_d t) + \frac{\dot{q}_0 + \zeta\omega_n q_0}{\omega_d}\sin(\omega_d t)\right] + \\ + e^{-\zeta\omega_n t}\left\{\frac{1}{m\omega_d}\int_0^t e^{\frac{-b(t-\tau)}{2m}} f(\tau)\sin[\omega_d(t-\tau)]\,d\tau\right\} \end{aligned} \tag{2.14}$$

where q_0 and $\dot{q}_0$ are respectively the modal coordinates and the modal velocities at the initial instant of computation (boundary conditions at $t = 0$). ω_d are the damped circular frequencies of the system expressed as

$$\omega_d = \omega_n\sqrt{1-\zeta^2} \tag{2.15}$$

The integral formulation within the curly brackets in the equation 2.14 is known as *Duhamel integral* and states that the reaction of a linear system subjected to a force $f(t)$ can be expressed by summing all the differential responses developed during the loading history (i.e. equal to the sum of the reactions of the system to the single impulses constituting the total force time evolution). This formulation can not be applied

[4] In some cases, as in high supersonic flows, it might be important to account also for thermal effects.

for a generic numerical analysis. However, given the initial conditions q_0 and $\dot{q}_0$, if the acting force is constant within every timestep, the equation 2.14 assumes the following form

$$q(t) = e^{-\zeta\omega_n t}\left[q_0\cos(\omega_d t) + \frac{\dot{q}_0 + \zeta\omega_n q_0}{\omega_d}\sin(\omega_d t)\right] + \\ + e^{-\zeta\omega_n t}\left\{\frac{F}{\omega_d}\left[\frac{4\omega_d}{\zeta^2\omega_n^2 + 4\omega_d^2} - e^{-\zeta\omega_n t}\frac{2\zeta\omega_n\sin(\omega_d t) + 4\omega_d\cos(\omega_d t)}{\zeta^2\omega_n^2 + 4\omega_d^2}\right]\right\} \quad (2.16)$$

The formulation of equation 2.16 can be adopted to update the modal coordinates in a time marching algorithm. Considering the equations 2.4 and 2.16, the nodal displacement vector can thus be expressed in function of time as

$$\{x(t)\} = \sum_{i=1}^{k}\{X_i\}q_i(t)$$

Similarly to the steady case, the whole deformation of the structure in unsteady state conditions, can be determined by linearly combining a certain number of modes using their time dependent modal coordinates as weights.

2.3 Solution mapping between non-matching domains

Vectors mapping is the process required when quantities need to be transferred between different non-matching discretized domains. In coupled fluid-structure analysis, the loads mapping consists in transferring the forces extracted from the cells faces adjacent to the wall of the CFD mesh (integrating scalar and vector fields) to the correspondent points of the structural domain in a form of forces vectors (figure 2.1).

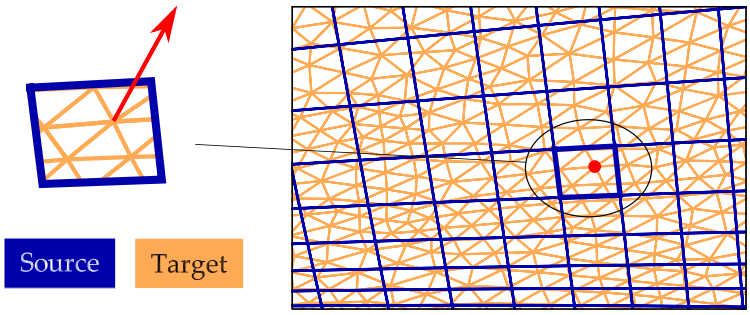

Figure 2.1: *Example of a mapping problem through non-matching meshes.*

The requirements for mapping methods are of being:

accurate - no loss of load magnitude or direction has to occur during the transfer process;

flexible - must be able to handle dissimilar meshes including the cases *fine-to-coarse* and

coarse-to-fine;

performant - must be capable to manage very large models in reasonable times.

With the view of the high fidelity requirements of CFD and FEM models, which involve the use of large meshes, the last point acquires particular importance.

2.3.1 Review of mapping schemes

A good review about load transfer schemes can be found in [45] and [46]. In both papers a great focus about load conservation and error estimation is given. Practical examples of aeronautical applications are presented in [47].

Among load transfer methods, it is worth to mention:

- **Point-wise interpolation/extrapolation** - the loads are interpolated at sources and become available as a point function. It is then used to extrapolate the load value at target point. The method is flexible because several strategies can be selected to interpolate the sources. The main drawback is that the equilibrium is not guaranteed.

- **Point to element projection schemes** - it relates to a direct connection between closest source elements and target points. The value at target is obtained using shape functions of the connected source element. The main complexity is related to neighbour searching (which can be optimised using space partitioning methods as octal tree decomposition). Local and global equilibrium are not guaranteed because the connection between sources and targets relies on local quantities and not to surface averaged ones.

- **Area weighted averaging** - the value of a target element is defined as the weighted average of the values of the source elements in contact. The weights are the areas of the intersections between the source and target elements. Conservation is guaranteed. The method can be classified as a special case of common refinement schemes that are proven to be conservative both globally and locally producing more accurate results if compared to point to element approach.

- **Mortar elements methods** - it is based on the introduction of an artificial thin shell structure that covers the domains interface as a vehicle for transferring the solution between the meshes [48]. The mortar interface usually is defined starting from the CFD mesh refining it splitting the cells at FEM nodes locations. The obtained shell mesh has nodes both at CFD and FEM nodal positions. FEM forces are obtained as constraints reactions from the solution of a static structural problem in which the shell nodes, corresponding to the FEM locations, are constrained while the ones corresponding to CFD locations are loaded with the CFD vectors.

2.3.2 The *RIBES* load mapping implementation

Interface reconstruction methods can benefit of the high quality achievable using the implicit surface definition based on RBF interpolation [49]. This approach is usually adopted to reconstruct a geometry that comes from a laser scan in reverse engineering applications. The mapping method implemented within the *RIBES* project exploits this feature.

The *RIBES* vectors mapping procedure consists in decomposing the original datasets in small RBF problems (for moderate amounts of data a single RBF transfer could be considered). The field, defined as a set of values at centroids or nodes of the source mesh, is interpolated using RBF. In case of force vectors field, the three components are interpolated by three independent RBF solutions. The *Partition Of Unity* (POU) method [50] is used to organize the source and target point sets into overlapping subdomains in which the interpolation problem is locally solved.

Given a smooth manifold M with an open cover U_i, a **Partition Of Unity** subject to the cover U_i is a collection of smooth, non-negative functions ψ_i, such that the support of ψ_i is contained in U_i and $\sum_i \psi_i = 1$ everywhere [51].

The force field is exchanged between the source subdomain and its target counterpart. In order to recover the continuity of the field and to guarantee the smoothness of the global solution, the resulting set of local solutions are combined together by a blending function. The blending polynomial is obtained from a set of smooth functions W_i by a normalization procedure

$$w_i(x) = \frac{W_i(x)}{\sum_j W_j(x)}$$

where the condition $\sum_i W_i(x) = 1$ has to be satisfied.

The weighting functions W_i can be defined as the composition of a distance function d_i and a decay function V_i. The distance function has to satisfy the condition $d_i(x) = 1$ at the boundaries of a subdomain. The decay function is defined from the distance function. Its degree can be arbitrarily defined. Examples of decay functions with growing degree are

$$\begin{aligned} DF(d) &= 1 - d \\ DF(d) &= 2d^3 - 3d^2 + 1 \\ DF(d) &= -6d^5 + 15d^4 - 10d^3 + 1 \end{aligned}$$

The shape of a subdomain can be arbitrarily chosen. For a spherical one, the distance function assumes the simple form

$$d(x) = \frac{r(x)}{R}$$

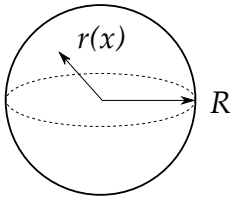

Spherical subdomains can correctly subdivide space only if they deeply overlap each other, otherwise some points could be left outside the subsets.

For a box (parallelepiped) shaped subdomain it assumes the form

$$d(x) = 1 - \prod_{r \in (x,y,z)} \frac{4(x_r - S_r)(T_r - x_r)}{(T_r - S_r)^2}$$

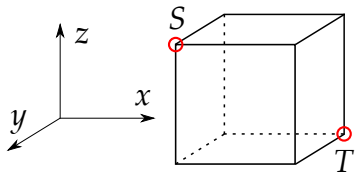

where S and T are the opposite points on the diagonal of the volume. Boxes best fit in Cartesian space. Their overlap depth can be arbitrarily decided. A zero overlap can be also set but in this case a loss of smoothness will occur.

The forces on the target mesh nodes are obtained by multiplying the interpolated forces density field by the area (or volume for space fields) of the corresponding target cells. The error in the equilibrium between source and target field is related to this point and depends on the differences between the two discretizations. Forces and moments equilibrium is smoothly recovered introducing three corrective coefficients (one for each component along X, Y and Z) that locally force the equivalence between the resultants of the source and target subdomains (not necessarily equivalent to the subdomains used in the interpolation). The coefficients continuity and their smooth transition between subdomains are obtained by overlapping the volumes and by the adoption of blending functions with a POU decomposition approach similar to the one adopted to organize the source and target points.

Assuming two overlapped subdomains, indicated as i and j, the corrected resultants are obtained as

$$\begin{cases} R_x = \sum F_{x,i} c_{x,i} w_i(x) + \sum F_{x,j} c_{x,j} w_j(x) \\ R_y = \sum F_{y,i} c_{y,i} w_i(x) + \sum F_{y,j} c_{y,j} w_j(x) \\ R_z = \sum F_{z,i} c_{z,i} w_i(x) + \sum F_{z,j} c_{z,j} w_j(x) \end{cases}$$

The corrective coefficients set is constant within the same subdomain. It is then possible to write

$$\begin{cases} R_x = c_{x,i} \sum F_{x,i} w_i(x) + c_{x,j} \sum F_{x,j} w_j(x) \\ R_y = c_{y,i} \sum F_{y,i} w_i(x) + c_{y,j} \sum F_{y,j} w_j(x) \\ R_z = c_{z,i} \sum F_{z,i} w_i(x) + c_{z,j} \sum F_{z,j} w_j(x) \end{cases}$$

The above formulations are valid for the computation of the homologous source subdomain resultants if:

$$c_i = \begin{pmatrix} 1 \\ 1 \\ 1 \end{pmatrix}; \qquad c_j = \begin{pmatrix} 1 \\ 1 \\ 1 \end{pmatrix}$$

The corrective coefficients, for the selected subdomains, are then expressed as:

$$c_{x,i} = \frac{[\sum F_{x,i} w_i(x)]_{source}}{[\sum F_{x,i} w_i(x)]_{target}} \qquad c_{x,j} = \frac{\left[\sum F_{x,j} w_j(x)\right]_{source}}{\left[\sum F_{x,i} w_j(x)\right]_{target}}$$

$$c_{y,i} = \frac{\left[\sum F_{y,i} w_i(x)\right]_{source}}{\left[\sum F_{y,i} w_i(x)\right]_{target}} \qquad c_{y,j} = \frac{\left[\sum F_{y,j} w_j(x)\right]_{source}}{\left[\sum F_{y,i} w_j(x)\right]_{target}}$$

$$c_{z,i} = \frac{[\sum F_{z,i} w_i(x)]_{source}}{[\sum F_{z,i} w_i(x)]_{target}} \qquad c_{z,j} = \frac{\left[\sum F_{z,j} w_j(x)\right]_{source}}{\left[\sum F_{z,i} w_j(x)\right]_{target}}$$

The reported correction is continuous and provides the mathematical equilibrium of local forces.

Procedure validation

The developed mapping procedure was validated using the HiReNASD (High Reynolds Number Aero-Structural Dynamics) test case [52]. It consists in a half wing/fuselage wind tunnel model used in a workshop for aeroelastic numerical methods validation. Both CFD and FEM grids are available. The static pressure field was mapped from the CFD wing surface grid to the wing structural FEM mesh. Table 2.2 reports the errors introduced by the interpolation process without correction between the two non-conformal domains.

Table 2.2: *Non corrected interpolation errors between HiReNASD model grids.*

$\mathbf{F_{x_{err}}}$ %	$\mathbf{F_{y_{err}}}$ %	$\mathbf{F_{z_{err}}}$ %	$\mathbf{M_{x_{err}}}$ %	$\mathbf{M_{y_{err}}}$ %	$\mathbf{M_{z_{err}}}$ %
47.3	6.6	1.0	13.1	13.8	27.8

Table 2.3 reports the errors on moments obtained applying the correction procedure implemented within the *RIBES* project (errors on forces are zero for definition). The errors are below 0.3% along all directions.

Table 2.3: *Corrected interpolation errors between HiReNASD model grids.*

$\mathbf{M_{x_{err}}}$ %	$\mathbf{M_{y_{err}}}$ %	$\mathbf{M_{z_{err}}}$ %
0.01	-0.28	-0.06

3

Coupling structural and aerodynamic solutions

The availability of numerical tools able to model the physics of the several aspects involved in a design, and their interaction, significantly increases the designer capability to produce higher-performance products. This is particularly felt, in aeronautics, concerning methods for studying the Fluid-Structure Interaction mechanism. In the modern scenario, the high performance of fighter, the increasing size of transport aircraft and the increasing performance request of the market, together with the extensive adoption of composite light weight structures, have enlarged the flexibility effects on the aerodynamic characteristics of aircrafts.

Several FSI methods with several order of fidelity are available in literature. Designers have the possibility to select the most appropriate numerical tool for each stage of the design process although the rising availability of powerful HPC environment motivates the interest in anticipating the adoption of more accurate tools in earlier stages of design. For this reason the interest in high fidelity based analysis methods, and in the improvements of their efficiency and robustness by novel implementation techniques, have significantly raised in the last years.

The *state of the art* in high fidelity FSI numerical methods consists in coupling, within an iterative process, RANS and FEM solvers in a so called *2-way* procedure. Several complexities arise in the implementation of an efficient coupling between the aerodynamic and the structural solution. Among them, the reception of the structural deformation within the CFD environment is probably the most dominant. In the work here presented we focus the attention on this topic by the setup and validation of high fidelity static aeroelastic analysis procedures in which the problem of domain adaptation is faced adopting mesh morphing techniques.

Beside the 2-way, an FSI method based on the modal superposition approach is proposed. This strategy offers the possibility to introduce some simplification without potentially compromising significantly the accuracy. It, furthermore, offers the possibility to include, in a *monolithic* way, the analysis within a single numerical environment with a significant improvement in term of robustness and performances. The

major drawbacks in the adoption of the modal approach are identified in the limitation of its validity to linear problems and in the potential uncertainness in the selection of the number of modes to be adopted (which can be however tackled by implementing a modal base qualification procedure).

3.1 Domain adaptation by mesh morphing

The adoption of multidisciplinary numerical analysis tools has become, in the last decade, the standard choice to face most of design problems in the aerospace field. These methods involve, in general, a geometric variation during the workflow that requires a parametrization suitable for automatic updating procedures (as in shape optimization, FSI analysis, ice accretion). The strategy used in the implementation of such parametrization affects both the efficiency and the quality of the solution. Most of the methods commonly used can be simplified into *CAD based* and *mesh morphing based*. The first permits to exploit the features of modern parametric CAD systems providing the possibility to manage complex models, to have great control of the quality of the geometry and to benefit of a large flexibility in variables and constraints definition (very useful in numerical optimization methods). The drawback of CAD based methods is the necessity to regenerate the computational domain for every new geometry to be investigated introducing uncertainness in the procedure robustness and in the accuracy of mesh dependent analysis methods. The remeshing requirements, furthermore, limits the application to problems having moderate dimensions (in term of computational domain cells number) or to relatively simple geometries suitable to be modelled by structured grids.

The mesh morphing approach consists in implementing the geometric parametrization directly on the computational domain. The new geometric configurations is obtained imposing a displacement of a set of mesh regions (e.g. walls, boundaries or discrete points within the volume) using algorithms able to smoothly propagate the model displacement to the surrounding volume. The performances of the morphing action (in terms of quality of the morphed mesh and computational resources requirements) depend on the algorithm adopted to perform the smoothing of the grid.

Mesh morphing methods can be categorized in *mesh-based* and *mesh-less* [53].

Mesh-based methods use the element topology of the mesh being morphed to define a computational space to compute new node locations.

Mesh-less methods ignore the element topology, in favour of other algebraic relationships.

Among the several algorithms available in literature, Radial Basis Functions are recognized to be one of the best mathematical framework to face the mesh morphing problem. Several advantages are related to the RBF mesh morphing approach:

- there is no need to regenerate the grid;

- the robustness of the procedure is preserved;
- its *meshless* nature allow to support any kind of mesh typology;
- the smoothing process can be highly parallelizable;
- the morphing action can be integrated in any solver.

The latter feature offers the very valuable capability to update the computational domain "on the fly" during the progress of the computation.

Figure 3.1 reports a typical application of mesh morphing for aerodynamic shape optimization. In the example reported the fuselage of a glider was optimized by two shape modifiers that act in the leading and trailing edge region of the wing root in spanwise direction. The objective was to reduce a large separation that occurred in the wing/fuselage junction at high incidence [54] (the left half model of the figure is the baseline geometry while the right one is the optimized).

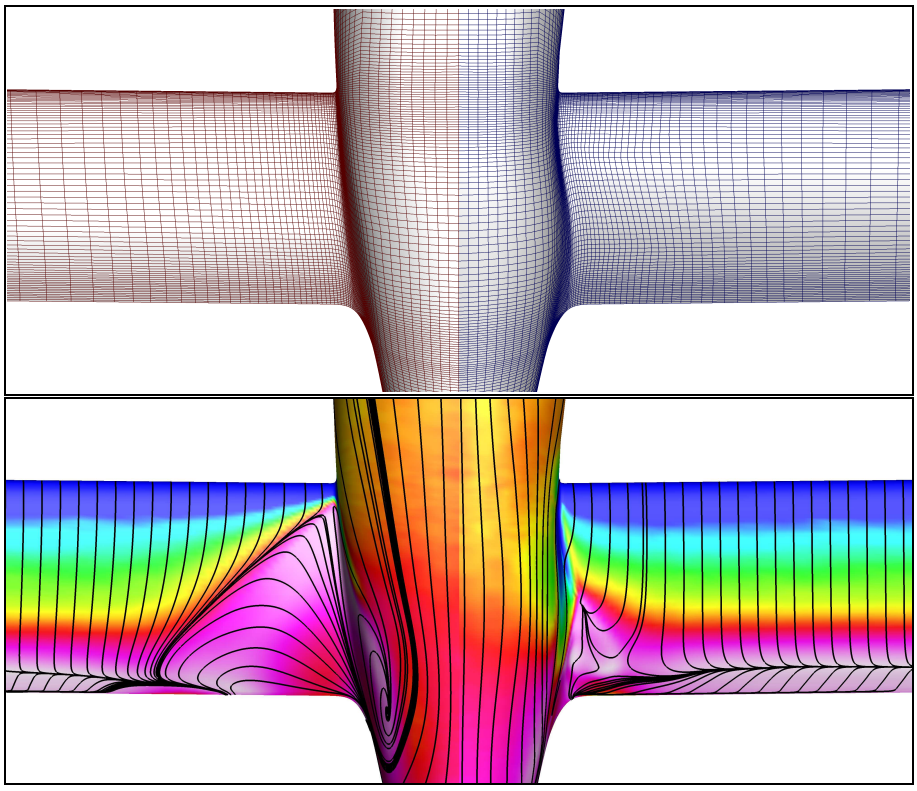

Figure 3.1: *Example of mesh morphing for aerodynamic shape optimization.*

The main disadvantages of RBF mesh morphing methods are the requirement of a "back to CAD" procedure, some limitation in the model displacement amplitude, due to the distortion occurring after extreme morphing, and the high computational cost related to the solution of the RBF system which, if large computational domains are involved, imposes the implementation on HPC environments.

3.1.1 The morpher tool *RBF Morph*

The first commercial mesh morphing software based on Radial Basis Functions was *RBF Morph*. Its development began in 2008 as a consultancy activity to a top Formula 1 team. The tool was born as an add-on of the *ANSYS Fluent* CFD code fully integrated in the solving process and was launched to the market in 2009 [55]. Its efficiency was successfully demonstrated on several industrial engineering problems that require geometric parameterizations (shape optimization, 6DoF analyses, ice accretion, static and dynamic FSI analyses) [56]. Today *RBF Morph* is also available as a standalone library to be coupled with any code. It was successfully embedded in the solving process of *OpenFOAM*, *CFD++*, *elsA*, *StarCCM+* and the FEM solvers *NASTRAN* and *ANSYS Mechanical* [57]. An implemented "*back2CAD*" feature provides the possibility to generate a CAD model of the morphed geometry.

RBF Morph allows to extract and control points from surfaces and edges, to put points on primitive shapes (boxes, spheres and cylinders) or to specify them directly by individual coordinates and displacements. Primitive shapes can be combined in a Boolean way allowing to limit the action of the morpher. The shape information deriving from an individual RBF setup are generated interactively using a GUI and subsequently used in batch commands that allow to combine many shape modifications in a non-linear fashion (non linearities occur when rotation axes are present in the RBF setup). The displacement of the prescribed set of source points, and of the combination of RBF solutions, can be amplified according to parameters that constitutes the parametric space of the model shape.

The definition and the execution of a morphing action is, with *RBF Morph*, completed by the following steps:

1. **setup** - the problems are manually defined and setup from the program GUI;
2. **fitting** - the RBF system is solved for each morphing action and solutions stored to be available for amplification;
3. **smoothing** - surfaces and volumes of the computational domain are morphed according to the stored RBF solution(s) and to arbitrary amplification factor(s).

The setup consists in the definition of the domain boundaries within which to limit the morphing action, in the selection of the source points with which to impose fixed and moving mesh regions and in prescribing the required movements to the points used to drive the shape deformation. In the fitting process the RBF system, derived from the problem setup, is solved and stored in a file to be ready to be amplified. This operation has to be performed only once for every RBF problem. Stored RBF solutions are very light (in terms of files dimension) compared to storing all the created morphed mesh. The smoothing action is performed firstly applying the prescribed displacement to the grid surfaces and then smoothly propagating the deformation to the surrounding domain volume. It can be performed combining several RBF solutions, each with its amplification factor, to constitute the parametric configuration of the computational domain. Figure 3.2 reports an example of an RBF setup. The red

points are distributed on the boundaries that are imposed as fixed. The green points belong to the mesh region to which the displacement is applied. The source points can both coincide to the grid points or can be generically located within the mesh volume.

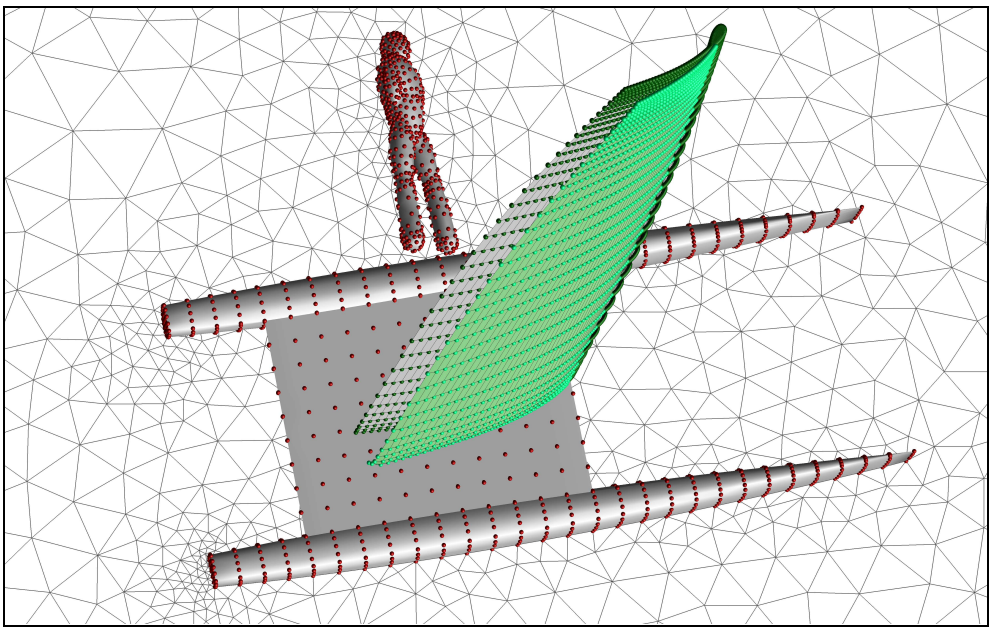

Figure 3.2: *Fixed (red) and moving (green) source points of an RBF setup.*

It is well recognized that RBFs have high computational costs. This aspect represented the main limitation in their application in the past. Such costs can be lowered by reducing the number of source points of the RBF problem. It was, in fact, demonstrated that the number of points required is independent of the mesh size (the problem is geometric) and that an 11000 points surface mesh can be represented by only 200 points [58]. Several strategies, to optimize the problem dimension, are possible. A straightforward method is, for example, to use a simple structured coarsening or unstructured agglomeration. More efficient approaches, aimed to minimize the surface interpolation error, are proposed in [59] in which a greedy method is used to select the surface points. Rendall and Allen proposed and compared three error functions used to guide the selection loop. *RBF Morph* is powered by a fast RBF solver that allows to scale up with complexity with a $N^{1.6}$ law. The fast implementation is based on a Local Correction Method (LCM) [60]. A greedy approach can be selected to firstly reduce the size of the points cloud. Omitted points can then be reintroduced with an advanced algorithm that allows to wisely decide the most important points to be kept. The number of refinement cycles can be controlled by the user. Usually two cycles are sufficient to achieve a substantial reduction of errors. The accuracy is then guaranteed by the LCM which introduces as many local RBF problem as the number of retained points. The combination of the global coarse RBF and the local ones (blended according to the *Partition of Unity* approach) allows to gain the desired tolerance at all the centres of the complete dataset. The Stand Alone version of RBF Morph features a Fast Multi Pole Method (FMM) that is adopted for the various RBF clouds that are part of the overall

LCM approach. The LCM distance needs to be tuned and usually exhibits an optimum value versus RBF fitting and evaluation time [61].

RBF Morph achieves good performance also by an efficient parallel implementation that, in HPC environments, allows to manage very large domains. Some examples that highlight the software performances are reported in table 3.1.

Table 3.1: *Examples of RBF Morph solver performance.*

Problem dimension	hardware	solution	elapsed time
14 mill. cells 60.000 source points	PC 4 cpu 2.67 GHz	fitting: smoothing:	53 sec. (serial) 3.5 min.
50 mill. cells 30.000 source points	HPC 140 cpu	fitting: smoothing:	25 sec. (serial) 1.5 min.
100 mill. cells 200.000 source points	HPC 256 cpu	fitting: smoothing:	25 min. 5 min.
Largest fitted cloud: 2 mill. points on 32 cpu in 3 hours *Largest morphed model (in our knowledge): 700.mill. cells on 768 cpu in 45 min*			

3.2 2-way CFD-CSM coupling

As already introduced, some of the main technical issues in CFD-CSM based FSI analyses setup, relate to the data exchange between fluid dynamics and finite element solvers.

- FEM and CFD outputs (structure displacements and loads, respectively) are discretized on non-matching clouds of points belonging to common boundaries for which the mathematical definition of the surfaces is missing. An interpolation, to close the iterative loop, is required. The surface pressure distribution, and friction vectors if required, have to be mapped as loads from the CFD solution into the FEM model. An error is, in general, introduced during this transfer and has to be contained adopting opportune correction criteria.
- Solvers coupling requires several actions: solutions extraction, files format conversion, setup update, run management and solutions quality check. If the analysis has to be included in an optimization loop, routines controlling the procedure in an automatic process have to be implemented in a complex environment that might require an expensive debugging session.
- The adaptation of the fluid dynamic domain to the shape of the deformed model estimated by the structural code (an action that has to be performed for every cycle of aerodynamic loads evaluation) is a process that can degrade the quality of

the computational grid. The mesh morphing action has to be propagated from the known displaced surfaces into the volume mesh and requires efficient and robust algorithms.

The workflow of a 2-way FSI analysis is synthesized in figure 3.3. The process begins with the CFD analysis of the rigid model at the desired condition. A mapping procedure is then applied to transfer the aerodynamic loads to a FEM model of the object under investigation. The structural analysis solution, in terms of wet surfaces displacement, is used as target for the mesh morphing tool in order to update the fluid dynamic domain according to the estimated deformed shape. The CFD computation is restarted on the new configuration and the cycle continues until the final deformed shape (for a steady condition) is reached.

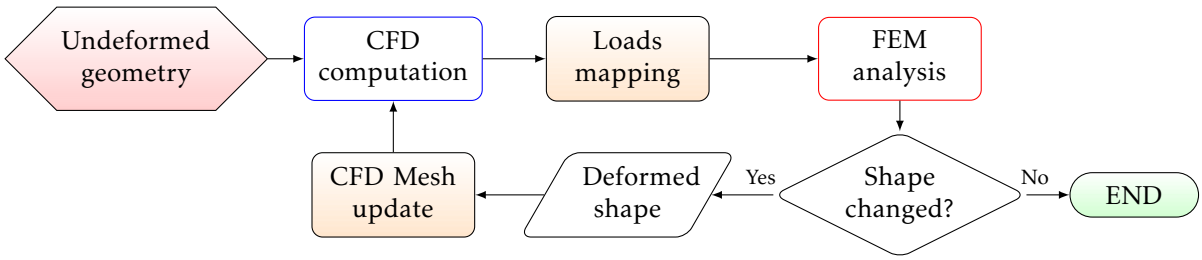

Figure 3.3: *Workflow of the 2-way FSI procedure.*

3.2.1 CFD mesh update

Several methods, able to prescribe different movements of the mesh regions, are implemented in *RBF Morph*. Among them, a very useful feature is the capability to import external geometries and displacement fields to be used as a target domain where to project the displaced nodes. The mesh morphing for 2-way FSI is performed exploiting the capability to import a FEM displacement solution field in *Nastran* format and to use it as a target for the smoothing process. In other words, the morpher uses a series of RBFs to produce a solution for the mesh movement using, as input source points, the imported FEM grid nodes and their displacements. The setup is made defining an arbitrary number of centres in the three dimensional space (to define the domain portion subjected to the morphing action), selecting the points belonging to the movable surface (FEM grids nodes) and prescribing them the computed movement (FEM points displacements). A displacement field that exactly interpolates the values prescribed at each source point is calculated in the fit stage and made available for nodes updating (smoothing) as a closed-form solution. The process can be executed by command lines and can be defined in a script file in order to automate the process. After fitting the RBF field for each direction (handled as separate scalar functions), a vector valued interpolation function that allows to calculate the displacement for any given point, is obtained. Such solution can be amplified using an arbitrary value. Using 0 as amplification factor no deformation will be applied. The target geometry is reproduced using 1 as amplification. Any intermediate value will produce a proportional intermediate

shape. Figure 3.4 reports, as example, the application on a morphing wing leading edge. The yellow mesh is the clean wing geometry. The black one corresponds to a deployed configuration obtained morphing the wing according to a displacement field computed using a non linear FEM analysis. The other overlapped grids are obtained amplifying the solution with the intermediate values of 0.25, 0.5 and 0.75.

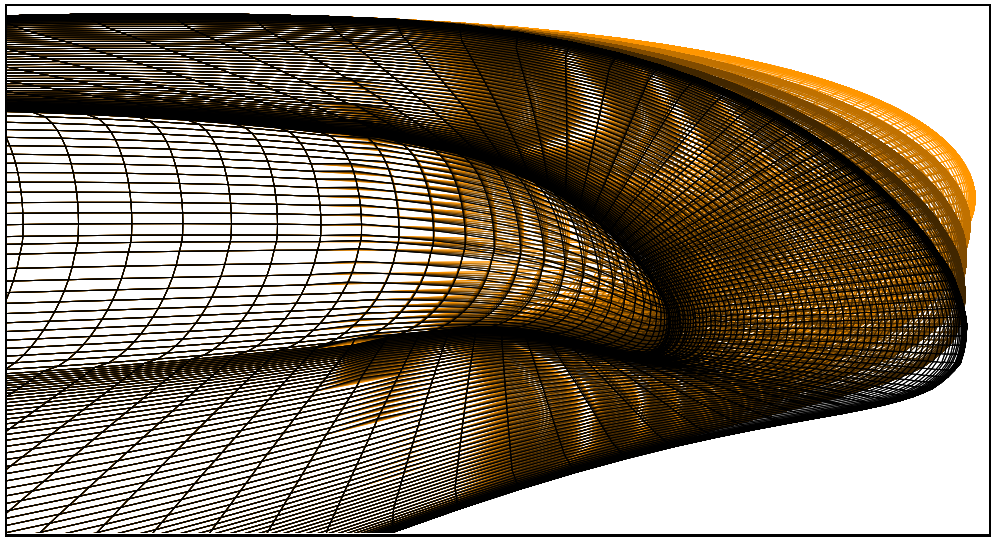

Figure 3.4: *Mesh morphing using a target non linear FEM result.*

3.3 Modal FSI Implementation

Modal FSI analysis consists in coupling structural and fluid dynamic solutions by representing the deformation of the structure as a superposition of a set of its natural modal shapes. It is a very well established method for dynamic analyses of complex FSI problems. The numerical implementation is based on a preliminary FEM modal analysis from which a number of natural modes is selected to be used in the creation of a parametric fluid dynamic domain. The grid is made parametric on modal coordinates and updated by mesh morphing during the progress of the fluid dynamic computation. Modal coordinates are used as weights for the morphing action of each modal shape and are obtained from the modal forces extracted by integrating the pressure and friction forces on the wall boundaries. The main advantage is the creation of simpler numerical environments respect to coupled CFD-CSM procedures. The iteration with external solvers is no further required and the complexities associated to the codes coupling (i.e. inputs/outputs format conversion, mapping interpolation, runs managements) bypassed. This numerical simplification represents a significant advantage in the vision, for instance, of implementing automatic procedures to be integrated in optimization environments. In the modal approach the "interface" between the fluid dynamic and the structural solution consists in just a single small vector representing the modal coordinates (modes are mesh independent and consistent for both fluid

and structural model). The major drawbacks is that the modal approach can be used for linear problems only which implies that structural non-linearities, due to material, large displacements or contacts, cannot be considered. The range of its application is then more restricted in comparison to the 2-way FSI methods but still wide enough to cover many of the typical fluid-structure interaction phenomena present in aerospace problems.

Some doubts about the generality of the modal approach, in the application for static FSI analysis, was highlighted during the first Aeroelastic Prediction Workshops[1] and concern the optimal choice of the number of modes to be adopted. Among the works presented during the workshop, Ritter [62] used 20 modes to perform its aeroelastic analysis. In a study presented at the IFASD 2013 Workshop [63], all the numerical tests were conducted using 30 modes. In general, when a new configuration has to be studied, and the opportune number of modes to be adopted cannot be estimated on the basis of previous experience, a modal base qualification procedure can provide useful indications in advance. The procedure consists in the extraction of a large enough modal base, in a preliminary CFD analysis of the rigid model (from which to extract loads and modal coordinates) and in the comparison of the modal amplified solution with the deformation computed by a static FEM analysis (using the same model adopted for the eigenvalues analysis) of the baseline geometry using the loads estimated by the rigid CFD model. The ability of the modal base to correctly replicate the FEM estimated displacement shape is then investigated by examining the vector field obtained subtracting the displacement of the modal approximation (using a candidate number of retained modes) from those coming from the static FEM analysis. The resulting vector field represents the modal truncation error. It can be used to decide how many modes to retain and to confirm if the guess base is large enough. This procedure was applied in the validation activity described in the next chapter where a deeper description of its setup is provided. The results of this activity were anticipated in [64].

The complete workflow of the modal FSI analysis is described in figure 3.5. Once available, the modal shapes are used to generate an RBF solution for each of the selected modes. The solutions are stored to constitute the database of the parametric mesh model (this action has to be performed only once for every structural configuration). The last step consists in implementing, within the CFD solver, the execution of the RBF based mesh update. The structural response can now be evaluated directly in the modal space. The analysis begins with the initialization of the dynamic mesh morpher with the stored RBF solutions and the modal forces calculation module to be available for recall during the computation.

The manual setup activities of a modal FSI implementation consists in the following steps:

- FEM model construction and computation setup of the undeformed configuration;
- structural modal analysis and extraction of natural frequencies and modal shapes;

[1] `https://c3.nasa.gov/dashlink/projects/47/`.

- generation and setup of the fluid dynamic numerical configuration;
- RBF setup and generation of the database of the morphing solutions based on the modal shapes;
- setup of the FSI computation within the CFD environment.

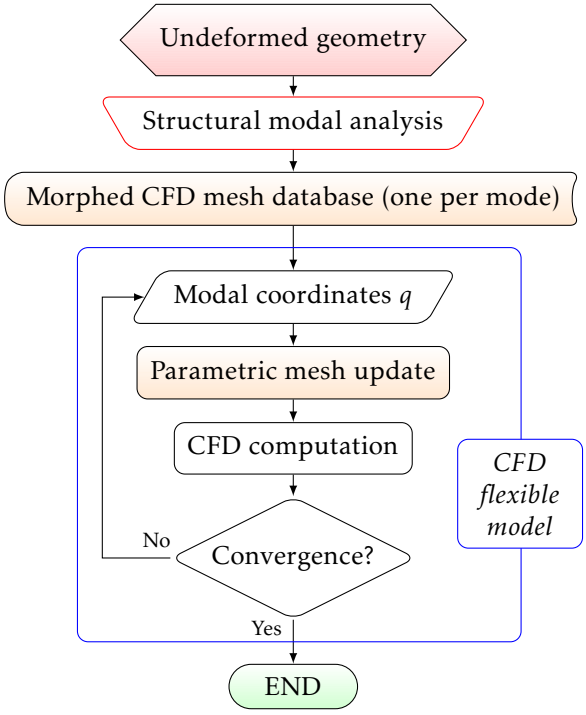

Figure 3.5: *Workflow of a modal FSI analysis.*

3.3.1 Parametric mesh formulation

The core of the modal implementation is the parametric mesh formulation, by modal coordinates computed during the computation, and its inclusion within the CFD environment. According to equation 2.13, the parametric formulation for the mesh becomes

$$X_{CFD} = X_{CFD_0} + \sum_{i=1}^{k} q_i \Delta X_i$$

where X_{CFD} are the positions of the grid nodes, X_{CFD_0} are the positions of the nodes of the undeformed baseline mesh, q_i are the (unknown) modal coordinates and ΔX_i are the modal displacements of the i^{th} mode (the modal shapes amplitude are normalized with respect to the mass and their absolute values are meaningless if not properly amplified using actual modal coordinates).

The modal forces associated to the aerodynamic resultants are calculated within the CFD solver by a loop performed over all wall domains under FSI investigation. The value of the i^{th} modal force is a scalar obtained from the sum of the dot product between the nodal loads and the nodal mode displacements of each node of the n_{surf} mesh surfaces.

$$F_i = \sum_{j=1}^{n_{surf}} \Delta X_{i_j}^T Q_j \tag{3.1}$$

Considering that a mass normalization criterion was defined for modes extraction, from equation 2.12 the modal coordinates are expressed as

$$q_i = \frac{F_i}{\omega_{n_i}^2} \tag{3.2}$$

The final expression of the parametric mesh formulation becomes

$$X_{CFD} = X_{CFD_0} + \sum_{i=1}^{k} \frac{F_i}{\omega_{n_i}^2} \Delta X_i \tag{3.3}$$

The mesh morphing model is embedded in the FSI procedure by a script which drives, every prescribed number of CFD iterations, the integration of the modal forces (eq. 3.1), the computation of the modal coordinates (eq. 3.2) and the update of the mesh combining the modal RBF solutions (eq. 3.3). The local nodal loads are obtained summing the inviscid forces components (which are vectors acting in a direction normal to the wall cells and obtained multiplying the computed pressure values by the cells area) and the viscous components (which are the friction vectors acting tangentially of the cells surface). In case of aeroelastic analysis of lifting bodies, as it will be later justified, the viscous components can be reasonably ignored.

It is worth to add that, even if not addressed here, the method can be used also for transient analysis. The FSI module implemented in *RBF Morph* uses the formulation described in section 2.2.2 to model unsteady phenomena. An example of its application for the transient aeroelastic response analysis of a wing after store separation is reported in [65].

4

Aeroelastic analysis of a transonic aircraft model

Aircrafts aerodynamic performance estimation by experimental wind tunnel measurements is a complex task that requires high qualified competences and sophisticated measurements procedures. The complexities increase with the Reynolds number and with the velocity of the test conditions both in terms of type of facility and in measurement techniques. In order to properly replicate, at model scale, the free flight conditions of the full scale aircraft, both Mach and Reynolds numbers have to be guaranteed at tests conditions. If both can not be ensured, an opportune compromise must be selected giving priority to the parameter that has the most dominant influence on the physical aspect that has to be studied (e.g. laminar flow, compressibility, stall...) and adopting opportune solutions to correct, or to reduce, the uncertainness induced by the missing similitude on the other parameter (e.g. forcing the development of turbulent flow by transition trips). When investigating transonic regimes, the requirements for the simulation of the two flow conditions becomes particularly conflicting. The high speeds involved force, in order to limit the tunnel mass flow rate, to reduce the model dimension (and consequently the Reynolds number).

The *Reynolds number* is a dimensionless quantity describing the ratio between inertial and viscous forces. It is based on a reference length x (the chord length in case of airfoils and wings) and is expressed as

$$Re = \frac{\rho V x}{\mu}$$

The *Mach number* is a dimensionless quantity representing the ratio between the flow velocity V and the speed of sound c. For an ideal gas it can be expressed as

$$Mach = \frac{V}{c_{ideal}} = \frac{V}{\sqrt{\gamma RT}}$$

Assuming the model dimension to be constrained, the only way to recover the Reynolds number is to act on the other parameters of its formulation. The most common strategy, adopted in high speed wind tunnels, is to pressurize a closed circuit thus increasing the density[1]. The loads on models, in this type of tests, can be very large and even if they are extremely stiff, wind tunnel models are not immune from deformation.

The 2-way CFD-CSM and the modal based FSI analysis methods described in the previous chapter were validated against one of this type of test case. It consists in a wind tunnel model of an aircraft in complete configuration tested in transonic conditions. The strong coupling between aerodynamics and structural deformation, due to the wing sweep angle, allow to assess the capability of the numerical tools to properly capture the interaction between deformation and aerodynamic performance.

4.1 The *Piaggio P1XX* business-class aircraft WT model

The geometry refers to a *Piaggio Aerospace* program, called *P1XX*, concerning the development of a medium size business jet class aircraft. A wind tunnel model of the complete aircraft (wing, fuselage, engine nacelle, vertical and horizontal tail) was built and tested in cruising conditions in the *ONERA S2MA* transonic facility.

Figure 4.1: *Piaggio P1XX transonic wind tunnel model (courtesy of ©Piaggio Aerospace).*

The model is steel-made and is mounted on a six-component balance by a sting connected to the fuselage (figure 4.1). It is equipped with eight external and four internal

[1] Another strategy is to cool down the flow in pressurized tunnels by using nitrogen in place of air acting then also on speed of sound and viscosity. Such wind tunnels are extremely expensive but allow to replicate the full flight Reynolds number of most aircrafts and to investigate the laminar flow behaviour (although it is still a very challenging task) at typical Reynolds numbers of modern liners in cruise [66].

static pressure taps used to calibrate the pressure measurement procedure. The flow-through nacelles have been dimensioned in order to maintain the real engine mass flow rate in cruising condition. The pressure distribution on the surface was measured using Pressure-Sensitive Paint (PSP)[2]. The principle of the PSP measurement technology is based on the response of a two-components photoluminescent paint excited with UV lights [67]. One of the two components of the paint is emitting a blue light, whereas the other one is emitting a red light. The response of the blue component depends on the local oxygen concentration in the air (i.e., the local static pressure) and on the intensity of the UV light excitation. The response of the red component only depends on the intensity of the excitation. A camera takes two consecutive pictures of the painted surface, the first one through a blue filter and the second one through a red filter. The ratio of these two pictures, referenced by the same ratio obtained wind off, is the image of the static pressure field. The external pressure taps, located on the wing, are used to calibrate the measurement procedure.

Mach number, angle of attack, and drag measurements were systematically corrected for upwash, wind-tunnel calibration, walls, sting line, and fuselage cavity pressure in order to obtain the aircraft data in free-flight conditions. The transition was tripped, applying carborundum grains at 5% of the local chord on both sides of the wings, tail, pylons, and nose. The turbulent transition was verified with acenaphtene visualizations. No measurements of the model deformation under load are available. Several complete polars were measured at several test conditions around the flight cruising Mach number. The data are properties of *Piaggio Aerospace* and are confidential. The absolute values of the coefficients were then omitted.

4.2 Numerical configurations

A first setup of a 2-way FSI analysis of the *P1XX* model, based on RBF mesh morphing, was made coupling the fluid dynamic *CFD++* solver with the structural *Nastran* code. That activity, published in 2012 [68], signed the beginning of a collaboration between *Piaggio Aerospace* and the university of Rome "Tor Vergata" that continued within EU research programmes. The work here presented is a deepening of that study, using *ANSYS Fluent* in place of *CFD++* and extending the FSI analysis to the modal superposition approach.

The setup of the procedures consisted in the preliminary preparation of the numerical configurations and in the coupling of the blocks summarized in figure 3.3 and 3.5. In the 2-way workflow, the load mapping between the CFD and the FEM domains was performed by the procedure implemented in the *ANSYS Fluent* solver in which the data are mapped using a zeroth-order interpolation [69]. The reason of this choice is simply because when this work was in progress, the *RIBES* mapping procedure was not yet available. This analysis gave, however, the opportunity to quantify the *ANSYS* procedure mapping error and to evaluate its influence on the FSI analysis of a wing.

[2]The paint application was found to have an impact on the forces measurements. The pressure measurements were then performed in a separate session and provided as a separated data set.

4.2.1 CFD analysis

Free-flight conditions were numerically simulated. The fluid dynamic computational domain generated is a multiblock structured hexahedral grid with farfield located at around 30 MAC (Mean Aerodynamic Chord) from the model. All aircraft surfaces were adiabatic viscous and the boundary layer was solved up to the wall. O-grid topologies were generated around the whole model. The cells were clustered on the walls in order to keep a dimensionless wall distance Y^+ between 0.5 and 1 in the analysis conditions.

The non-dimensional wall distance for a wall-bounded flow is defined as

$$Y^+ = \frac{u_* y}{\nu}$$

where u_* is the local friction velocity, y is the distance to the nearest wall and ν is the kinematic viscosity. The formulations of the friction velocity and the kinematic viscosity are

$$u_* = \sqrt{\frac{\tau_w}{\rho}}, \qquad \nu = \frac{\mu}{\rho}$$

where μ is the dynamic viscosity, ρ is the fluid density and τ_w is the wall shear stress expressed as

$$\tau_w = \mu \left(\frac{\partial u}{\partial x} \right)_{y=0}$$

The wall normal cells dimension growth rate is lower than 1.3. Around the airfoil there are 220 elements and 110 on the wing in spanwise direction. The total grid dimension is 14 million of volume elements (figure 4.2). No grid sensitivity analysis was performed. The selection of the grid topology, the choice of the domain extension, the wall cells clustering, and the total mesh dimensions derive from guidelines for this type of analyses and from extensive grid sensitivity assessment activities performed against the well known *DLR F6* experimental test case. It, furthermore, derives from experiences on several validation campaigns on other non-public experimental data.

Steady compressible RANS computations, using the density-based solver, an implicit time integration scheme, and second-order upwind spatial discretizations, were performed. The wind tunnel static pressure, temperature, and velocity were imposed at farfield. Back pressure was imposed at the domain outlet and adiabatic viscous wall boundary condition on the model surfaces. The flow field is assumed to be symmetric. The half domain was then modelled.

The flight condition at which the comparisons were performed was Mach 0.8 and Reynolds 4 millions and refer to the design cruising aircraft Mach number. The angle of incidence was 1.4 deg. This value was selected according to the PSP measurements available. The two-equation *realizable* $k - \epsilon$ turbulence model [70] was used together with a near-wall correction in the inner boundary layer region. Such approach should ensure proper accuracies in regions where potential velocities gradients would not guarantee Y^+ values lower that 1.

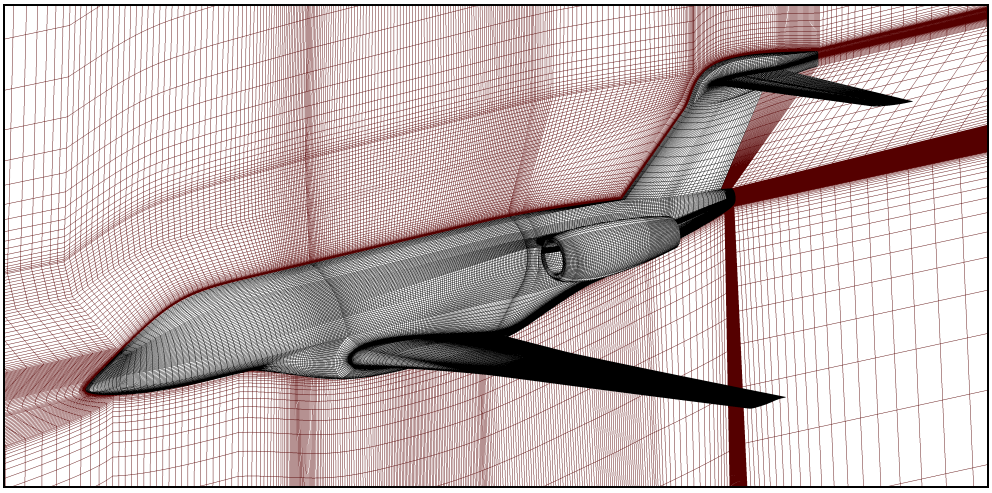

Figure 4.2: *P1XX - fluid dynamic domain of the aircraft.*

two-layer near-wall correction - The principle is to divide the domain into a viscosity-affected region and a fully turbulent region delimited by a turbulence Reynolds number in which the reference length is the minimum wall-normal distance of the cell centres [69]. In the region in which the computed Reynolds number is below 200, the one-equation model of Wolfshtein [71] is applied. The turbulent viscosity μ_t and dissipation rate ϵ are, here, corrected and smoothly blended with their high Reynolds number definitions from the outer region.

4.2.2 FEM model and modal analysis

Figure 4.3 details the wind tunnel model structure. The wing root extends into the belly fairing and is bolted to the central balance block. The wing root region, the bolts, and the balance structure are much stiffer than the external wing. The model deformation was then assumed to be limited to the exposed part of the wing. This simplification is probably not true if applied to the horizontal tail, but its influence should be of a lower order of importance compared to the measurements tolerance.

The structural FEM model was limited to the external wing region and was constrained at the wing/fuselage junction section. The wing is fully steel-made. The domain was then developed using solid hexahedral elements within the whole wing volume (figure 4.4). The total model dimension is 32100 nodes and it comprises 27666 solid elements and 7363 auxiliary shell elements (with negligible stiffness and mass) added on the skin to define the wetted interface. The mass of the wing structural model is 7.89 kg.

The modal analysis was performed evaluating up to 20 natural modes of the structure. Figure 4.5 plots the cumulative mass contribution of each mode by the progressive summation of their Effective Mass Participation Factors for the most relevant type and direction, namely the vertical translation and rotational factor along Y axis. The evaluation of EMPFs is used, in complex systems characterized by several randomly

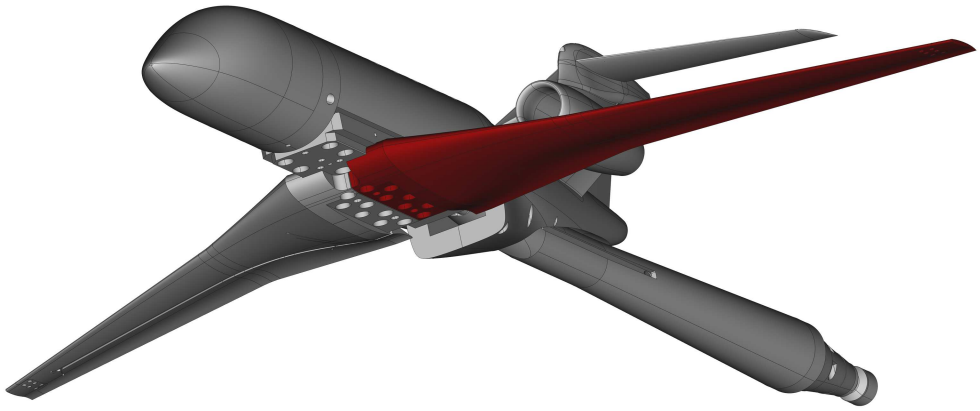

Figure 4.3: *P1XX - detail of the wind tunnel model assembly.*

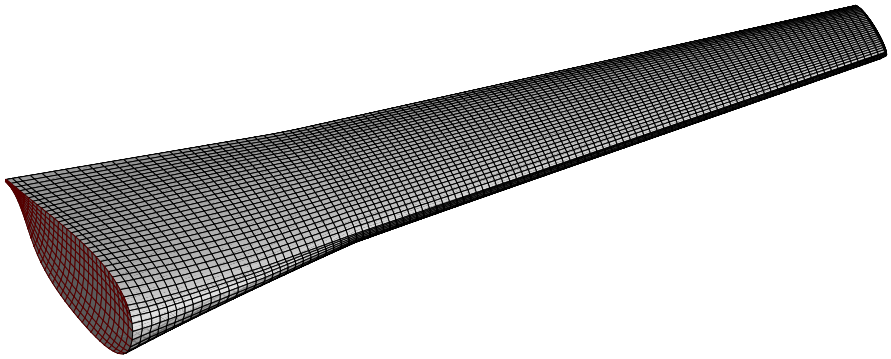

Figure 4.4: *P1XX - FEM mesh of the wind tunnel model wing.*

contributing modes, to evaluate how many modes to select to reach a certain percentage of the total system mass. Best practices suggest to involve a number of modes so that the summation of their effective participation factors reaches a threshold value of around 80% of the total mass. Such a target is, in general, not necessary for FSI analysis. This assumption will be, however, confirmed by the results of the modal analysis following reported. It was, in fact, decided to extract only six modes to be used to populate the modal base. With this number, the percentage of total mass contributing to the vertical translation and rotation along Y direction is respectively 52% and 18%.

The frequencies and shapes type of the six modes extracted are reported in table 4.1. The last two columns refer to a solution quality check on the FEM model made converting all the elements from linear to parabolic (increasing the size to 123820 nodes) and using the finer model as reference. The convergence error (last column) with respect to the reference is less than 1%.

4.2.3 Mesh morphing setup

The morphing action has been limited to a mesh region surrounding the wing surface and contained within a cylinder. The RBF problem is defined by selecting a number

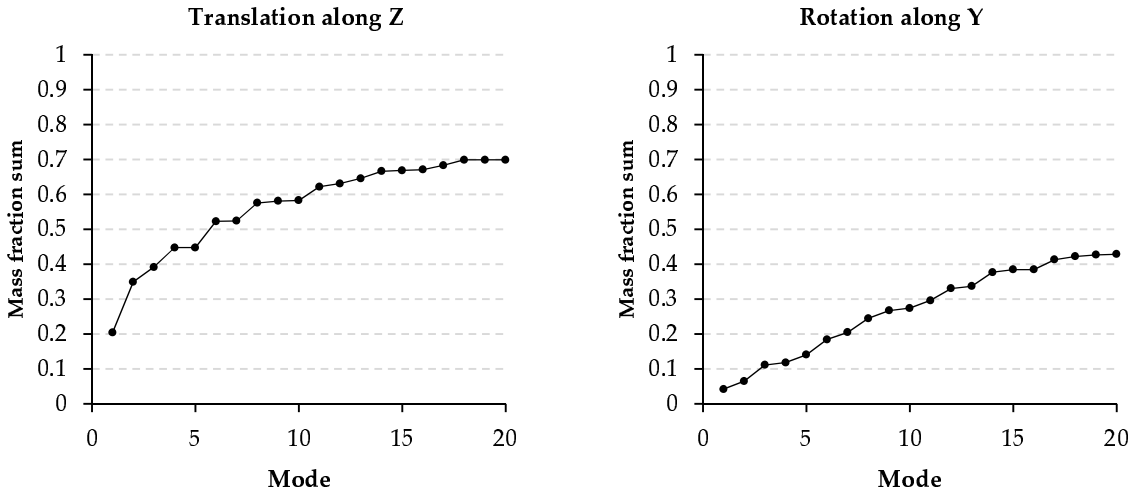

Figure 4.5: *P1XX - Sum of modal mass fraction of first 20 modes.*

Table 4.1: *P1XX - computed structural modes of the model wing.*

Mode	Shape	Frequency (linear el.) *Hz*	Frequency (parabolic el.) *Hz*	Error *%*
1	Bending 1	72.89	72.74	0.21
2	Bending 2	251.14	249.93	0.48
3	Bending 3	541.07	537.11	0.74
4	Bending 4	592.96	590.37	0.44
5	Torsion	684.23	683.50	0.11
6	Bending 5	1004.59	995.37	0.93

of source points on the boundaries and by imposing them the required displacement. Figure 4.6 details the RBF configuration. The source points are divided within three sets. The first set contains the limits of the fixed domain defined by a uniformly distributed number of points (red points in figure 4.6) on the limiting boundary cylinder. The second set contains all the points of the aircraft surface, with the exception of the wing, to which a zero displacement is imposed. The last set contains the nodes on the wing (green points in figure 4.6) to which the RBF solution, obtained using the FEM output, is prescribed. The points on the wing correspond to the nodes of the wing FEM mesh.

A two-step approach was adopted to prescribe the deformation. In the first step, the FEM nodes positions, and the corresponding computed displacement field, are used to generate a small RBF problem limited to the wing surface. The task is performed by an automatic tool that allows to extract the required information from the

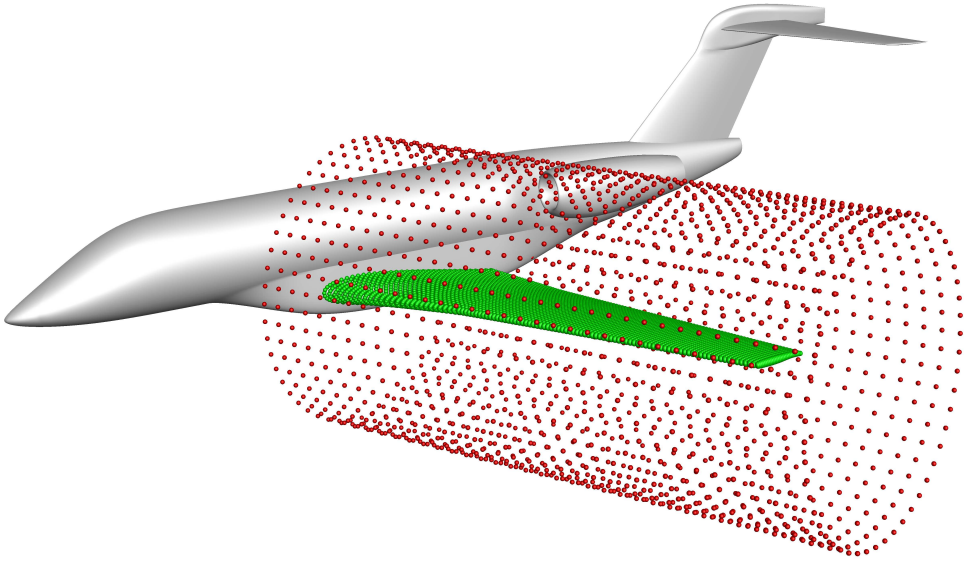

Figure 4.6: *P1XX - domain defining the RBF fitting problem.*

`.bdf` and the `.pch` files [3]. The mesh smoothing process, that accounts for the defined limiting boundary and the fixed position prescribed to the other aircraft walls, is performed within the second step in which the RBF problem is setup taking as input the RBF solution of the first step. This procedure is a trick that provides a smother solution and better quality of the morphed mesh. For both steps, the linear RBF $\varphi(r) = r$ with global support was adopted.

If the centres density is fine enough, the linear RBF is a choice that guarantees a reasonable fast solution and a smoothing process with the minimum mesh distortion. A higher order RBF (as the cubic one) can be useful to gently control surfaces using few centres.

The RBF problem, in this test case, is based on about 60000 source points. The smoothing process of the complete CFD mesh took 209 seconds on a PC equipped with a *Quadcore Intel* i5 2.67 GHz and with 8 GB of memory. A check of the morphing action was performed each time by verifying the skewness of the cells. No appreciable quality degradation was observed in the range of geometric deformations involved in the performed analyses.

4.3 2-way FSI analysis

The 2-way FSI solution was obtained applying the workflow sketched in figure 3.3. The CFD domain is adapted according to the RBF mesh morphing setup described in the previous section. The cycle starts from the CFD solution obtained on the undeformed geometry and progresses restarting each run from the previous computation. The plots

[3] the `.bdf` and the `.pch` files are respectively the standard input and output of the *Nastran* solver that contain the FEM problem and its solution.

in figure 4.7 report the typical coefficients convergence histories of a restarted computation. The first 10000 iterations refer to the solution obtained on the rigid model from scratch. The following curves, after the jump, describe the typical behaviour obtained on elastic models restarting the run from the converged rigid solution (in the plots the first cycle of the 2-way analysis is reported). When starting from scratch, a complete convergence was reached after 4000 iterations. When restarting the computation of a deformed geometry from the rigid solution, 1000 iterations were sufficient.

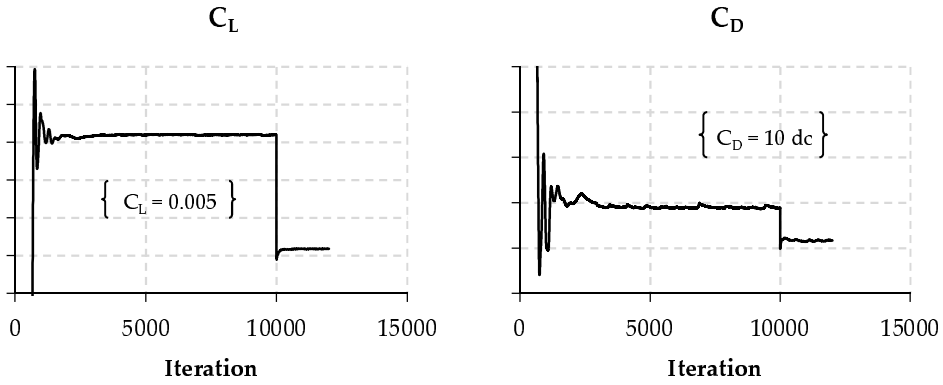

Figure 4.7: *P1XX - typical restart convergence histories.*

The cycle of the workflow was repeated until no more variation in loads and deformation was detected. Since the FEM field (total displacement) refers to the rigid configuration, at each cycle the CFD mesh was restored to the undeformed configuration before restarting the fluid dynamic computation. In this analysis, three iterations between the two solvers were sufficient to obtain a converged static solution (figure 4.8).

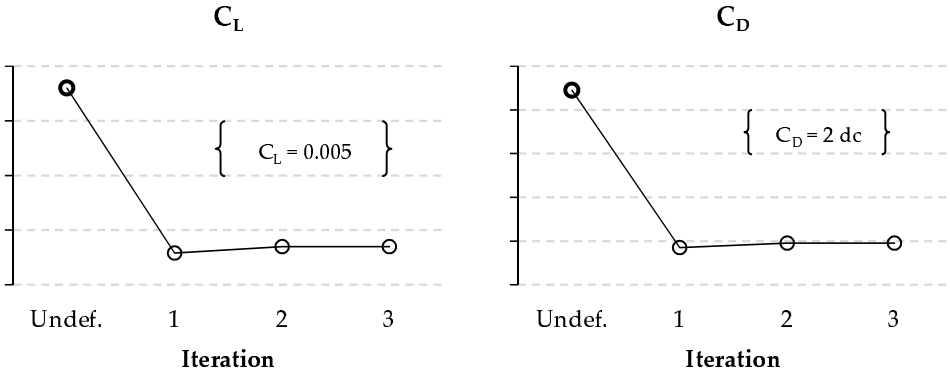

Figure 4.8: *P1XX - lift and drag coefficients convergence histories in the 2-way FSI cycle.*

The CFD loads were mapped on the FEM mesh using the interpolating procedure

implemented in *ANSYS Fluent*. The output is directly written in the FEM solver format. An error due to the different surface discretization adopted in the CFD and FEM domains is expected. Figure 4.9 evidences the difference between the two meshes in the root leading edge region. Only pressure loads were extracted to be applied to the FEM model. The contribution of viscous forces to the deformation of the wing were neglected. This assumption is in general valid for lifting surfaces because it is reasonable to neglect the viscous lift in comparison to the pressure component and because the aeroelastic influence of viscous drag is negligible. The wing drag module is, in fact, in the order of 20 times lower than lift and acts in a direction in which the wing moment of inertia is very high.

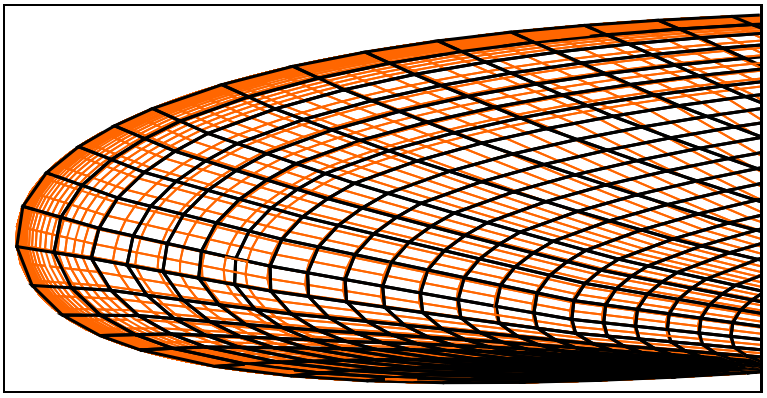

Figure 4.9: *P1XX - detail of FEM (blue) and CFD (yellow) surface wing meshes overlap.*

In order to evaluate the error introduced by the mapping procedure, the Z component of the integral value of the mapped loads on the wing surface has been calculated both on the CFD solver, before the extrapolation, and on the FEM code after having imported the loads file. This comparison has been performed for all cycles and is reported in figure 4.10 and table 4.2. A systematic overestimation, in the order of 2.5%, on the load applied to the FEM model was observed. A significant higher error on the X force components was present but, as stated previously, its impact was considered irrelevant. The quantification provided, however, the sense of how significant its influence might be, in general, for non lifting surfaces.

Figure 4.11 compares the 2-way FSI solutions with the solutions obtained on the undeformed geometry and with the experimental polars. The computed lift coefficient reduction, caused by the deformation of the wing, is lower than 0.015. The lift value, at constant incidence, of the elastic solution moves closer to the experimental lift curve but it is still overestimated of about 0.2 degree compared to the measurements. It is difficult to evaluate if the incongruence on incidence is due to a limit in the correction criteria adopted for the extrapolation of the experimental measurements or to uncertainness to be ascribed to the CFD configuration. Considering that the correction of the wind tunnel angle of incidence is a very challenging task due to the differences between the tunnel and the free flight configuration (wall blockage effect and presence of the string line), the entity of the difference observed can, however, be considered relatively modest. The drag difference, compared to the experimental

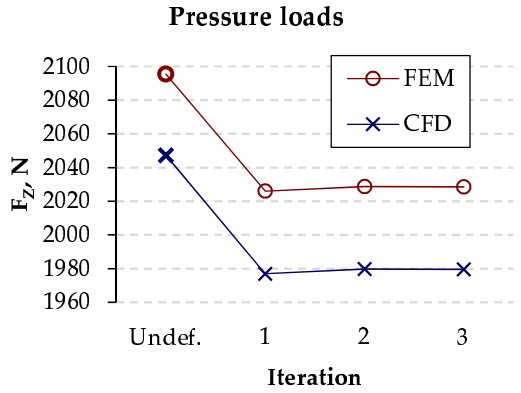

Table 4.2: *P1XX - errors on load mapping.*

Iteration	F_Z FEM	F_Z CFD	Error
	N	*N*	*%*
Undef.	2095.5	2047.3	2.353
1	2026.0	1976.9	2.485
2	2028.7	1979.7	2.478
3	2028.6	1979.5	2.476

Figure 4.10: *P1XX - F_Z from FEM and CFD.*

polar, conversely, remains almost unchanged (in the order of 4-5 drag counts), which means that the wing deformation is modest enough to poorly impact the induced drag. The observed differences are, however, in the order of the declared measurement error tolerances of the balances.

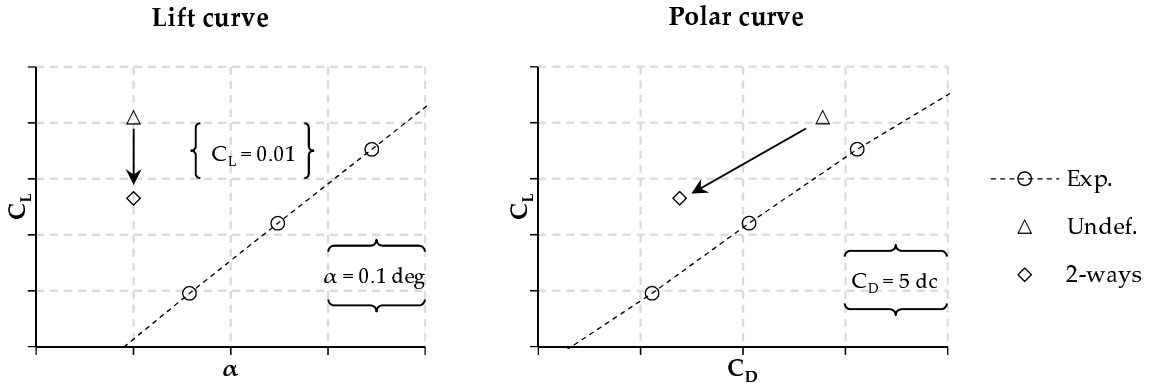

Figure 4.11: *P1XX - coefficients comparison with experiments.*

The wind tunnel model is extremely stiff. A displacement of the wing under aerodynamic loads, in the order of 5 millimetres, was anyway observed at the wing tip (the model span is 0.6 m). The contour plot reported in figure A.1 in appendix evidences the displacement of the whole wing computed by the 2-way procedure after three iterations. A qualitative view of the wing deformation under load (with an amplified scale) is given in 4.12.

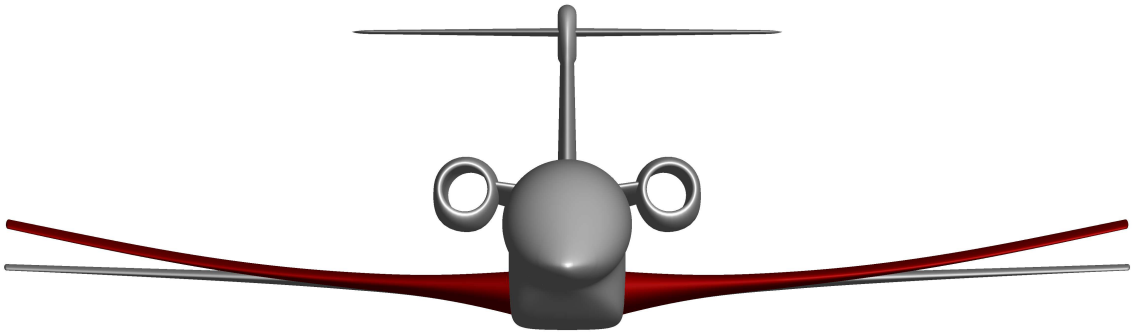

Figure 4.12: *P1XX - wing deformation amplified 10 times.*

4.4 Modal FSI analysis

Up to six structural vibrating modes were extracted from the FEM modal analysis and used for the implementation of the modal FSI procedure. For each mode, an RBF solution was computed and stored in a database in order to generate a parametric mesh in modal coordinates. Six modal analyses, with six parametric mesh formulations, implemented adopting a rising number of superimposed modal shapes, were performed. This approach, in addition to the modal base qualification, provided the sensitivity on how is the influence of the modal base dimension on the final solutions. Figure 4.13 displays the shapes of the first six wing vibrating modes whose natural frequencies are reported in table 4.1.

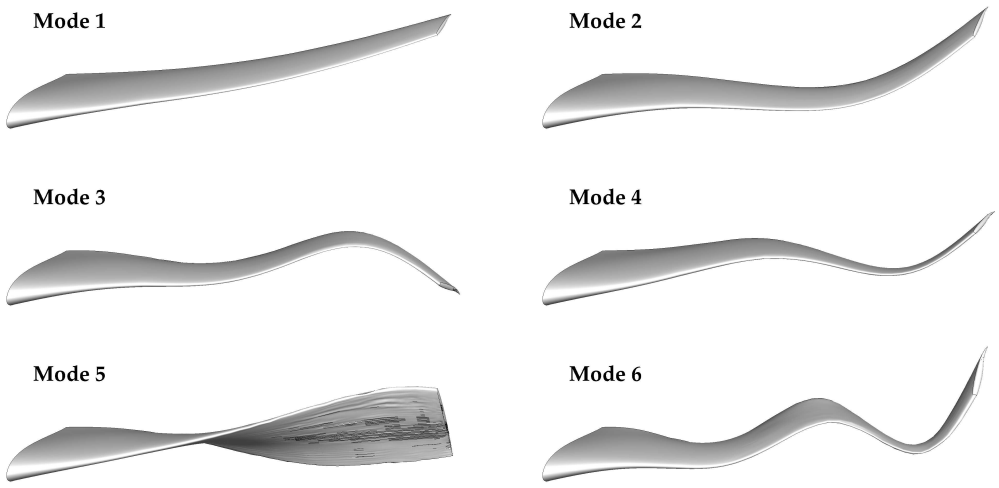

Figure 4.13: *P1XX - first six vibrating modal shapes of the wing.*

According to the workflow described in figure 3.5, the dynamic mesh morpher with the stored RBF solutions and the modal forces calculation module are initialized to be available for recall during the CFD computation. The mesh is updated, according to the modal coordinates computed during the progress of the run, every 20 iterations.

4.4.1 Modal base qualification

The adequacy of the modal base was verified using the first six modes. The modal base qualification helps to evaluate in advance how many modes are needed to reproduce a static deflection in coherence with the deformation that would be evaluated by the FEM analysis of the structure under the same aerodynamic loads. The check can be conducted on both CFD and FEM grids since the modes are independent from the mesh. It consists in the generation of the static deflection combining a certain number of modes and in its comparison with the FEM solution on the rigid model. Modal coordinates are evaluated by the CFD analysis of the rigid model. The qualification is useful in situations where the complete 2-way results are not available. It is included here for the sake of completeness even if both the full 2-way and the modal analysis, using up to six modes, are available.

The procedure to inspect the quality of the approximation, when only few modes are retained, consists in subtracting the approximated shape, obtained by modal superposition, from the elastic shape obtained by the FEM analysis. The modulus of the vectors obtained represents the approximation error. The resulting field can be inspected using standard post processing methods (i.e., plotting the deformed shape). The behaviour of the errors computed with the *P1XX* selected modal base, plotted onto the FEM mesh, is shown in figure 4.14. In order to emphasize the error distribution along the geometry, the error vectors were amplified by a factor 2000 in all plots with the exception of the plot reporting the error using only the first mode (left top figure) which was amplified by a factor 200. The first mode shape is, in fact, by far the most dominant mode and matches the bending deformation of the wing.

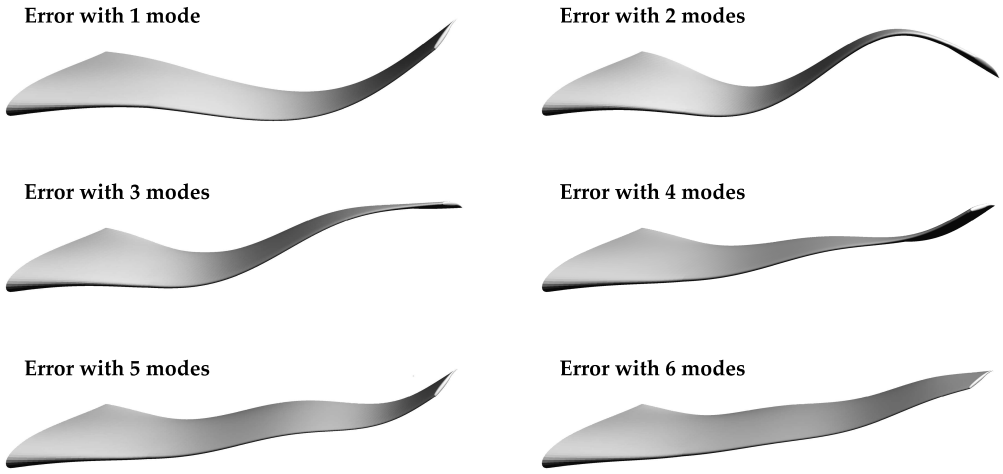

Figure 4.14: *P1XX - modal truncation error retaining from one to six modes.*

The shape of the errors can be compared with the structural natural modal shapes of figure 4.13. It can be seen that they look similar to the shape of the next mode dropped. For example, the error using the first mode only, looks to be shaped like

the second mode. Similarly, the first and second modes produce an error shape very similar to the third mode. When the third and fourth modes are added, the shape looks to be a combination of the fourth and fifth modes (it is worth to observe that their frequencies are quite close). By adding the fifth mode, the shape of the sixth mode can be clearly recognized.

The table 4.3 quantifies the results of the modal base qualification. The columns report respectively the number of modes involved, the modal coordinates computed by the rigid CFD model and the maximum displacement error evaluated using both CFD (third column) and FEM (last column) meshes. Taking as reference the displacement of 5 millimetres computed at the wing tip by the 2-way procedure, we can assume that the adoption of only the first mode would produce an error on deformation in the order of 7%. Adopting the first two modes the error would reduce to 0.7%. Such an error is approximatively maintained when adding more modes.

Table 4.3: *P1XX - modal base qualification using the first six modes.*

Modes retained	**Modal coordinates** q	**Maximum error on CFD mesh** *mm*	**Maximum error on FEM mesh** *mm*
1	0.00319593	0.362	0.361
2	-0.00017681	0.035	0.035
3	-0.00001032	0.034	0.032
4	0.00001273	0.044	0.043
5	-0.00000491	0.047	0.042
6	-0.00000502	0.035	0.030

It can be preliminarily assumed that two modes might be enough to setup a reasonable accurate modal analysis. We will have the confirmation of the correctness of this assumption comparing the solutions obtained by the six modal analyses in which the parametric mesh formulation was implemented adopting a rising number of superposed modal shapes.

4.5 Comparison between 2-way and modal solutions

Three points on the wing trailing edge were taken as references to monitor the geometry displacement. The pressure distribution was compared at four spanwise sections. The location of the three points and the four sections are displayed in figure 4.15.

Table 4.4 and figure 4.16 report the modal coordinates resulting from the computation adopting the superposition of the first six structural modes of the wing. It is evident how the first mode is by far dominant in comparison to the others.

The obtained modal solutions were compared to the 2-way FSI solution and to the experimental data. The comparison with the experimental drag polar is reported in

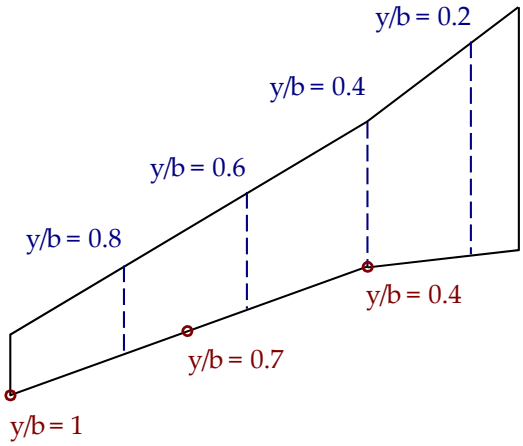

Figure 4.15: *P1XX - location of monitored points and sections on the wing.*

Table 4.4: *P1XX - values of modal coordinates.*

Mode	Modal coordinate q
1	0.00303478
2	-0.00017124
3	-0.00001094
4	0.00001200
5	-0.00000697
6	-0.00000495

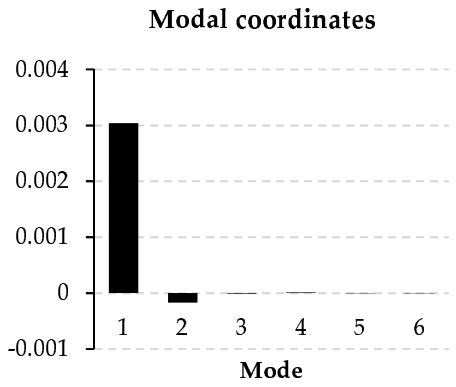

Figure 4.16: *P1XX - 6 modes modal coordinates.*

figure 4.17. The differences between the elastic solutions and the solution obtained with the rigid model (undeformed geometry) are listed in table 4.5. All the aeroelastic numerical configurations gave, from an engineering point of view, almost the same solution. The maximum difference in lift coefficient between the several elastic models is lower than 0.0006 whereas the range of drag coefficients variation is limited within 0.2 drag counts.

Figure 4.18 and table 4.6 report the computed displacement of the three monitored points on the wing trailing edge for all numerical configurations. The maximum displacement is close to 5 mm which, referred to the model dimension, is slightly lower than 1% of the wing semispan. Because of the larger chords and thickness in the inner region, the displacement of the point at the kink section ($y/b = 0.4$) is, as expected, very low. It can be assumed that the points displacement reach the ultimate values by adopting only the first two natural modes. Furthermore, the values reached are in very good agreement with the displacements estimated by the 2-way FSI analysis.

Swept wings have a strong coupling between aerodynamics and structural defor-

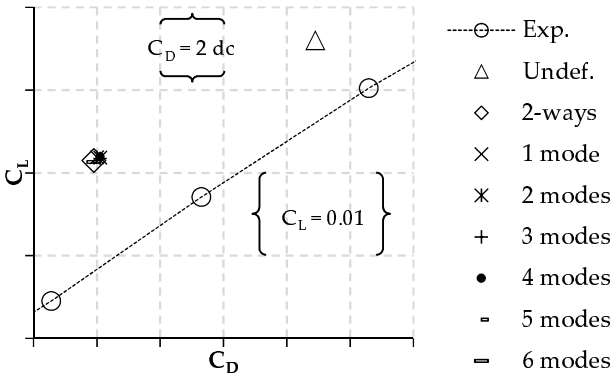

Figure 4.17: *P1XX - modal and 2-way solutions.*

Table 4.5: *P1XX - variation respect undeformed.*

Case	ΔC_L	ΔC_D *dc*
2-way	*-0.0145*	*-7.0*
1 mode	-0.0142	-6.8
2 modes	-0.0141	-6.9
3 modes	-0.0143	-6.8
4 modes	-0.0141	-6.8
5 modes	-0.0147	-7.0
6 modes	-0.0147	-7.0

mation. This coupling grows with the value of the sweep angle. More in detail, the coupling is between the wing box bending, which acts along its elastic axis, and the aerodynamic twist, which is referred to the streamwise wing section. In sweptback wings, the coupling consists in a twist increase as a consequence of the wing bending under positive lift (pitching down rotation at tip respect to the root). The wing deformation, therefore, has a direct unloading effect on the outer region of the wing[4]. Figure 4.19 empathizes this mechanism by amplifying the wing deformation. It is clear how the wing tip of the bent wing has a lower aerodynamic incidence respect to the undeformed geometry.

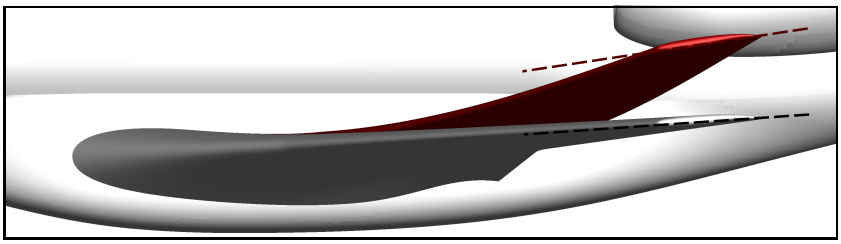

Figure 4.19: *Aerodynamics and structural deformation coupling mechanism.*

If the angles of attack of spanwise sections of a wing are not equal, the wing is said to have *twist*. If the angle of attack at the tip is less than that at the root the wing is said to have *wash-out* or *negative twist* [72].

In order to evaluate the capability to correctly capture this phenomenon, the variation of the wing tip section angle of incidence was monitored and compared to the

[4]For the same inner workings, forward-swept wings, with a conventional structure arrangement, have a decreased divergence speed compared to back-swept wings [3] because to a bending increase follows a wing tip load raise which further contributes to the structural bending.

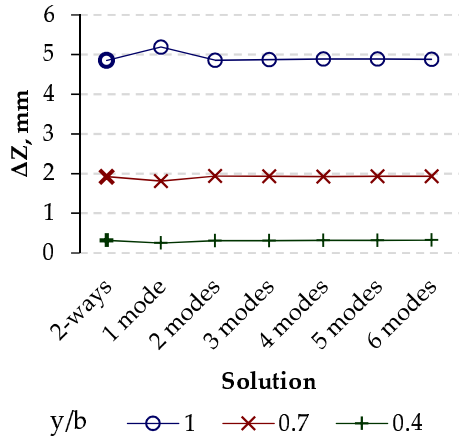

Figure 4.18: *P1XX - monitored points displacements.*

Table 4.6: *P1XX - values of displacements of monitored points.*

y/b =	0.4	0.7	1
	ΔZ	ΔZ	ΔZ
Case	*mm*	*mm*	*mm*
2-way	*0.320*	*1.923*	*4.852*
1 mode	0.251	1.811	5.188
2 modes	0.307	1.938	4.853
3 modes	0.312	1.933	4.871
4 modes	0.315	1.927	4.890
5 modes	0.318	1.935	4.891
6 modes	0.321	1.933	4.879

2-way solution. Figure 4.20 and table 4.7 report the result of this comparison. The absolute geometric twist increment under load is, in general, lower than half a degree. Also analysing the twist variation it can be stated that the solution does not change significantly when adopting a number of modes greater than two. Furthermore the modal solution replicated accurately the 2-way deformation.

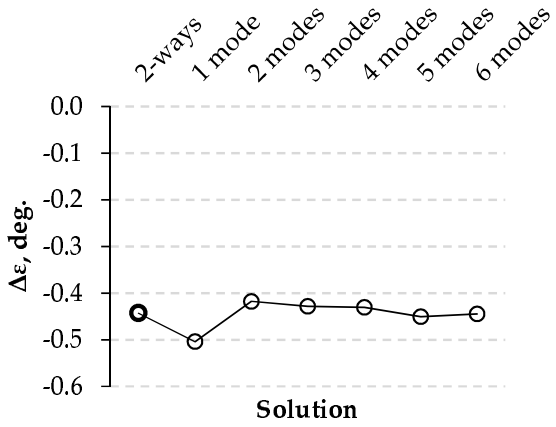

Table 4.7: *P1XX - values of wing geometric twist variation.*

Case	Δε (y/b = 1)
	deg.
2-way	*-0.443*
1 mode	-0.504
2 modes	-0.418
3 modes	-0.428
4 modes	-0.430
5 modes	-0.450
6 modes	-0.445

Figure 4.20: *P1XX - wing geometric twist variation.*

The plot of figure A.2 in appendix highlights the geometric differences between the solution of the 2-way analysis and the modal solution obtained by accounting for the first six modes. The contour values are the modules of the vectors obtained subtracting the displacement estimated by the 2-way procedure from the deformation obtained with the modal analysis. The maximum difference is lower than 0.03 mm.

Both 2-way and modal FSI methods are based on the linear assumption (the first because of the setup of the FEM analysis and the second for definition). If we consider that the load mapping procedure applied in the 2-way computation introduced an overestimation in the order of 2.5% on the integral force acting on the wing FEM model, it might be reasonable to expect the method to overestimate the deformation by a similar percentage (in the order of 0.12 mm). The geometric differences between the modal and the 2-way solutions are, conversely, practically insignificant (in the order of 0.5% of the maximum displacement). The conclusion is, therefore, that the influence of the error introduced by the interpolating mapping procedure is negligible, for the analysis of lifting surfaces, or that the modal approach suffer of an uncertainness of the same order of the error introduced by the load mapping process (i.e. the modal approach overestimates the deformation by 2.5%).

No information is available on the deformation of the wind tunnel model during the experimental tests. No direct displacement validation of the numerical solutions is then possible. The aero/structural coupling induced by the presence of the sweep angle, together with the transonic regime of the flow field, provides, however, an indirect indication of the accuracy of the elastic models. The recompression structures on the wing surface, that develop in transonic conditions, are in fact extremely sensitive to any geometric variation. If properly captured, the estimated aerodynamic twist induced by the wing deformation should find a confirmation when comparing the numerical with the experimental pressure distribution. The contour plots in figure A.3 in appendix provides a global view of the pressure distribution on the wing estimated by the two flexible numerical models. In the same figure, the experimental measurements are reported with the same scale suggesting a good agreement with the computations. A deeper evaluation is possible analysing the solutions at the four monitored wing sections indicated in figure 4.15. Such comparison is detailed in the four plots of figure A.4 in appendix where also the solution obtained on the rigid model is reported. Very good agreement is in general obtained in all sections in most parts of the flexible upper wing surface. Some differences are observed in terms of higher waviness in the most external sections indicating that the effect of the wing deformation is, as expected, aerodynamically significant only in the outer region. Even if differences from experiments are still present, the pressure distributions computed by the flexible models better match, compared to the solutions obtained on the rigid model, the experimental values, particularly in term of shock strengths and position. This agreement is a confirmation, as stated before, that the aeroelastic mechanism is properly captured by both 2-way and modal FSI numerical models.

Small disagreements are evaluated in the pressure recovery at the wing trailing edge where the numerical solutions do not match the experimental values. In the pressure decreasing region, in the lower side, the pressure values are slightly uniformly overestimated. This difference is, however, negligible at a inner sections but it becomes little stronger in the recovery region where a higher load is computed. The direct consequence of this disagreement is an overestimation of the lift coefficient, as clearly evidenced when comparing the experimental lift polar with the numerical solutions (figure 4.11).

5

Aeroelastic analysis of the *RIBES* wing model

RIBES is the acronym of "*Radial basis functions at fluid Interface Boundaries to Envelope flow results for advanced Structural analysis*". It is the name of a European research project led by the University of Rome "Tor Vergata" and funded within the 7th framework aeronautics programme JTI-CS-GRA (Joint Technology Initiatives - Clean Sky - Green Regional Aircraft). The project started December 2014 and was officially completed December 2016. Focus of research was the improvement of the accuracy of CFD-CSM based aeroelastic analysis methods. It, furthermore, allocated a significant amount of the budget on the setup of an experimental wind tunnel test campaign aimed to the development of a database for the validation of FSI numerical tools.

The assessment activity detailed in the previous chapter proved the accuracy of the proposed CFD and FEM solvers coupling methodology and provided useful guideline about the applicability of the modal approach for static aeroelastic analysis of a strongly coupled aerodynamic/structural phenomenon. The wing structural model was, however, very simple and no sensitivity was provided about the quality of the solution that would be obtained facing the problem of a more realistic wing structural configuration. Although several experimental static and dynamic aeroelastic test cases are available (e.g. Agard 445.6, HiReNASD, EuRAM), the literature is relatively poor concerning wind tunnel tests with realistic aeronautical wing structures. The RIBES experimental campaign was setup with the express objective to cover this gap.

5.1 Experimental measurements campaign

The *RIBES* test case should accomplish the task of being significant for a realistic wing design problem and of being suitable to be experimentally verified in a low speed wind tunnel (in order to contain costs). The first requirement is explicitly accomplished developing a typical wing box structure referring to a traditional realistic wing topol-

ogy (spars, ribs and skin) and by an aerodynamic design aimed to replicate as much as possible, at wind tunnel flow conditions, a realistic reference target load distribution (specifically, the wind tunnel model should be aerodynamically designed to replicate as much as possible an elliptical spanwise load shape). The latter requirement is achieved by dimensioning the wing model so to be able to produce significant deformation with moderate loads. Unfortunately, the adoption of a metal structure and the scaling effects to dimensions compatible with a typical low speed wind tunnel test section, act in the opposite direction.

The requirements for the wing tunnel measurements and for the model were:

- ***for the tests***
  - static pressure measurements under steady flow conditions;
  - forces and moments measurements;
  - model deformation measurements;
  - stresses measurements on most significant structure locations;
- ***for the model***
  - scaled physical model of a metallic wing type of structure;
  - rectangular shape and small thickness;
  - installation of strain gauges and pressure pick-up points at its surface.

The model deformation was reconstructed applying photogrammetric techniques and using a laser scan. The principle of photogrammetry is to obtain a stereoscopic visualization by taking a couple of images simultaneously using two cameras installed with different angle respect to the model. The 3D reconstruction process consists in recognizing the position of a matrix of markers opportunely placed on the model surface and to estimate the model deformation by the visual 3D evaluation of the displacement of this discrete number of points with respect to their known static positions (figure 5.1).

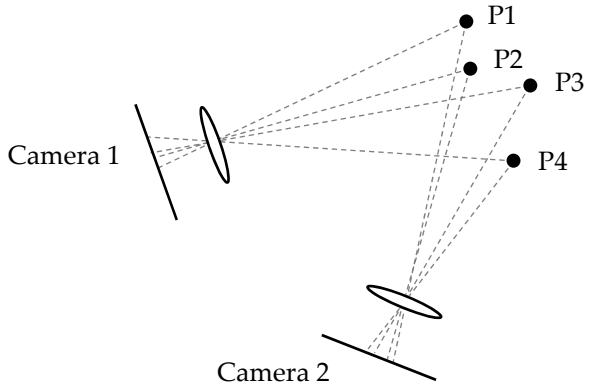

Figure 5.1: *Geometric principle of stereoscopic visualization.*

This technique is based on the principle that a set of points in space occupies different positions in two images taken from different locations. The 3D points coordinates, in an absolute frame, are derived from their 2D locations in the images according to the principle that every point is projected onto a particular point in a camera sensor plane and has to lie on a straight line.

5.1.1 Wind tunnel model design and manufacturing

The *RIBES* test article design had a long development process in which several iterations, with the model manufacturer and the topic manager of the project, leaded to reconsider the original wing configuration proposal. The first topology was thought with the vision to include an aero-structural coupling by adopting a sweep angle and to design a wing suitable for a reference realistic aircraft. A complete structural and load similitude at testing conditions of a scaled wing, however, would have required a relatively high speed which is not compatible with a typical not pressurized low speed wind tunnel with a sufficient large test section. Furthermore, a simple scaling of a "real wing" is not feasible for manufacturing reasons (the thickness of the skin would reduce to impracticable dimensions). A design, expressly customized for our purpose, had then to be planned. The aerodynamic design of the wing was made selecting an opportune geometric twist and designing a new airfoil specifically with the objective to reproduce as much as possible, at wind tunnel conditions, the pressure distribution the reference aircraft would exhibit in cruise. The complexities encountered related mainly in the attempt to maximize the wing deformation (in order to facilitate the displacement visualization) maintaining the wing box topology and constraining the sheet metal thickness to dimensions that allow a safe model assembly by rivets. Preliminary analyses of candidate dimensionings confirmed the difficulties in obtaining a tip displacement, under a maximum measurable loads (by wind tunnel balances) in the order of 100 kilograms of lift, higher that 1% of the wing span[1]. It was then decided to release the requirement of referring to a realistic aircraft (in order to orient the design only on the measurements requirements without constraints), to eliminate the sweep angle (in order to focus on the structural verification aspect of the FSI mechanism without interferences of other effects) and to comply the manufacturer suggestion to simplify the model geometry (in order to reduce costs and risks of manufacturing uncertainness). Even if a significant amount of the effort allocated on the *RIBES* project was dedicated to the model design, a deep detailing of its process is not considered strictly relevant to the main objective of this thesis and would require a long deviation that, due to lack of space, will be here avoided. Only the main steps of the test article design will be then following reported.

Among the configurations that were designed and verified aerodynamically and structurally, a straight wing 1.6 meters wide, with a root chord of 600 millimetres and 0.7 as taper ratio, was selected as final configuration (figure 5.2). In order to simplify its manufacturing, no twist was adopted. The skin is simply obtained by lofting a

[1] A more detailed description of the genesis of the original starting *RIBES* model candidate is reported in [38].

single curvature surface between the root and the tip airfoils geometries (the airfoil is maintained unchanged along all span).

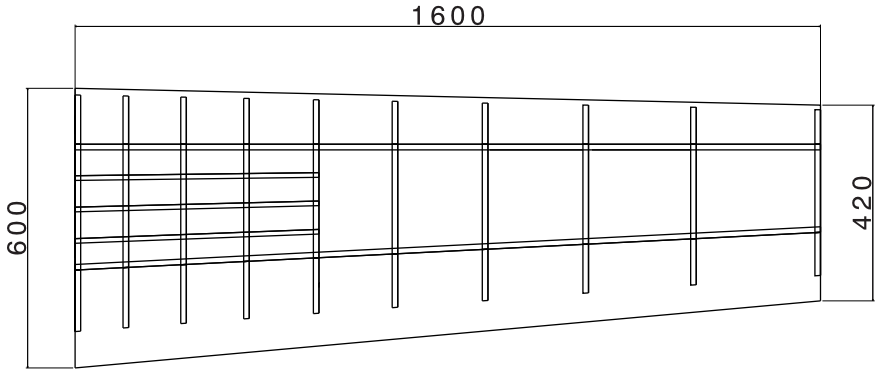

Figure 5.2: *RIBES - layout and planform dimensions.*

The airfoil was designed starting from the *Göttingen 398* scaling the original shape to a thickness $t/c = 11\%$ and redesigning the leading edge in order to improve the stall performance. Figure 5.3 reports the designed wing section.

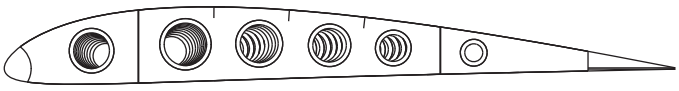

Figure 5.3: *RIBES - airfoil of the wing.*

Structural dimensioning

The wing box is a typical aeronautical structure with two C-shaped spars and ten ribs. The front spar is located at 20% of the chord and is maintained orthogonal to the symmetry plane. A moderate negative sweep angle (in the order of -0.3 deg.), referred to the line passing through the 25% of the chords, is then present. The rear spar is located at 65% of the chord. The reference surface is 0.816 m^2.

The external skin is divided in four parts: an upper, a lower a leading edge and a V-shaped trailing edge panel. They are joined to the structure by flush head CherryMAX rivets. The model is connected to the wind tunnel balance by a flange and a tubular rod (figure 5.4). The wing components were subjected to two treatment before assembly. The first was an Alodine treatment to prevent corrosion while the second consisted in a primer to prepare the wing structure to paint. Figure from A.6 to A.8 in appendix report a series of pictures of the model structure assembling and manufacturing process.

The model was dimensioned verifying the design at the target operative condition: flow speed equal to 40 m/s and around 60 kilograms of lift force. The CFD domain used in this phase reproduced the test section, including the inlet convergence element, of the selected wind tunnel facility (figure 5.5).

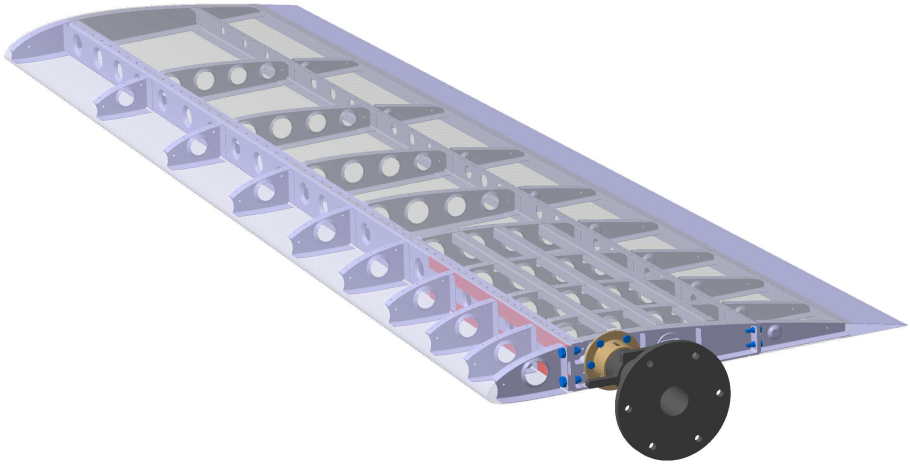

Figure 5.4: *RIBES - test article CAD model.*

The mesh was composed by 3.5 million of hexahedral elements. The boundary layer was solved up to the wall of the wing model while wall functions were applied to the tunnel walls. In figure 5.6 the obtained spanwise load distribution (left) and the shape of pressure distribution on the wing surface (right) is reported. The load is enough close to the target spanwise elliptical distribution. In this condition, 60 kilograms of lift is generated with a lift coefficient equal to 0.74.

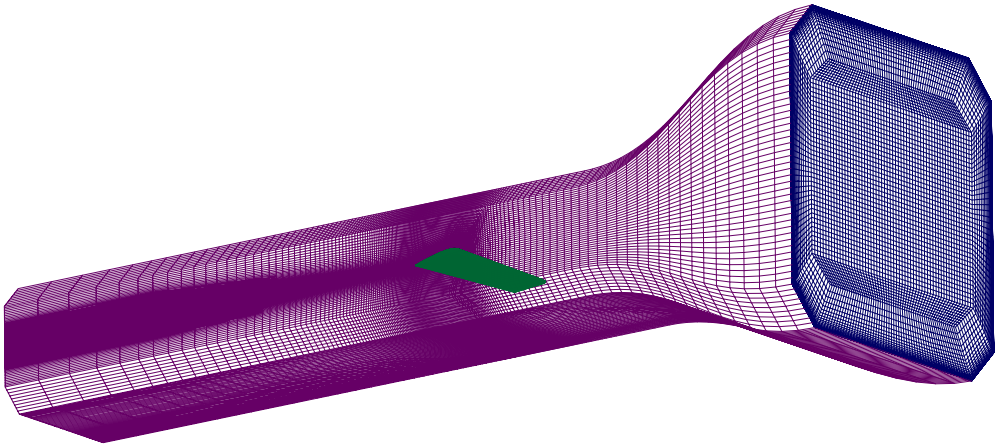

Figure 5.5: *RIBES - wind tunnel CFD domain.*

The FEM analysis was essential to dimension the thickness of the sheet metal components and to reinforce the regions of stresses concentration. It was, furthermore, adopted to check the plates buckling onset. This aspect was, in fact, the main driver in dimensioning the model. In order to maximize the wing deformation, the target thickness of spars and skin should be minimized. With this configuration most of the load is carried out by the skin. The buckling verification identified instability problems on the upper skin in the root region, as evidenced in figure 5.7, where plates are subjected

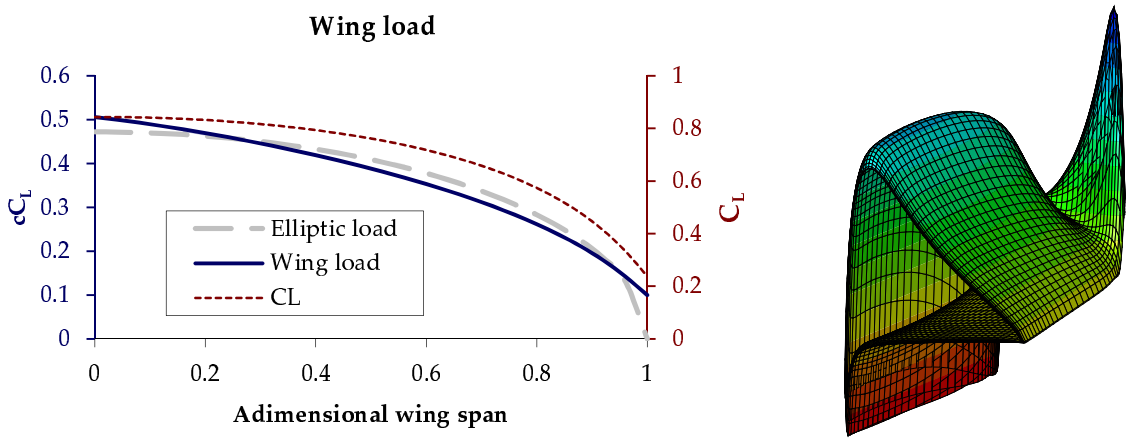

Figure 5.6: *RIBES - aerodynamic load on the wing surface.*

to maximum compression[2].

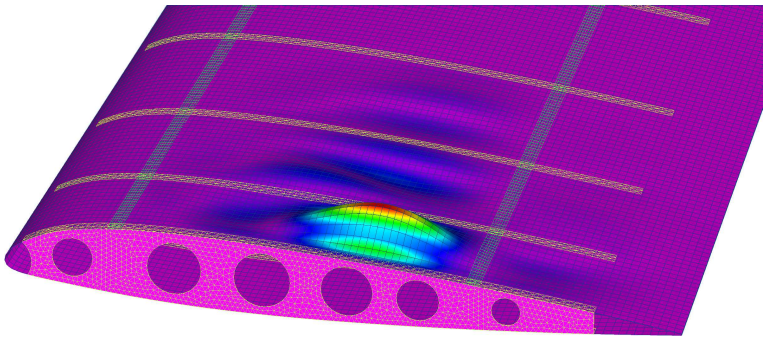

Figure 5.7: *RIBES - instabilities observed on the upper panel.*

Before acting on the thickness of the spars, a new structural solution was studied. In addition to a variable ribs distribution along the span, aimed to reduce the distance between the supported opposite edges of plates, two stringers were added to the skin in the upper panel and extended up to the fourth rib to further reduce the buckling multiplier. The new configuration demonstrated to improve the buckling behaviour maintaining unchanged the thickness of the elements. The eigenvector associated with the first positive buckling eigenvalue (which was in the order of 1.2) is shown in Figure 5.8 (left). The following study was focused on optimizing the stringers distribution (that became three in the final configuration) and plates properties.

It has to be noticed that the plates instability guided the design much more than the material stress limits. As evidenced in figure 5.8 (right) in fact, the maximum stress observed in design conditions is lower than 40 MPa which is very far from the limits of the material (the adopted material is the 2024-T3 aluminium alloy which has a yield strength higher that 270 MPa). From this point of view, the *RIBES* model dimension-

[2]The airfoil of the preliminary solution reported in figure 5.7 do not coincide with the final geometry which was designed in a following phase.

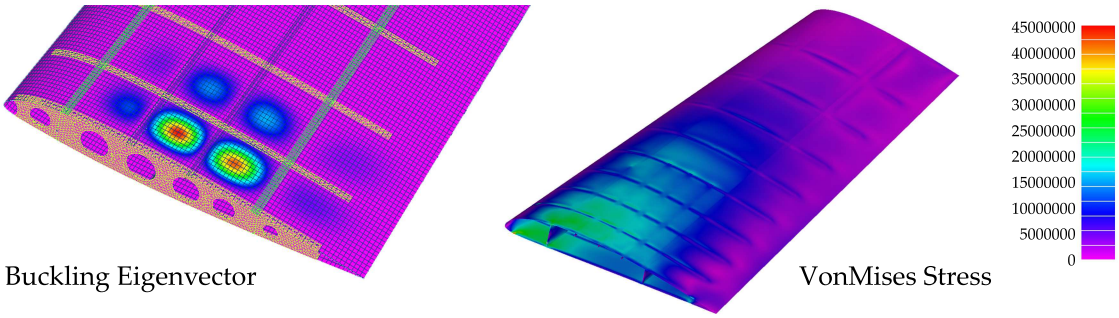

Figure 5.8: *RIBES - results of the FEM verification.*

ing followed an unusual philosophy. Aircraft wings design, in fact, is typically oriented on weight saving adopting the minimum *Factors of Safety*, on the primary structures, required by airworthiness authorities (in some case it is consider acceptable the structure to operate with plates in post-buckling conditions). The *RIBES* wing had as main target the maximization of the deformability of the structure which oriented its dimensioning toward the minimization of the plates thickness (both spars and skin) up to the minimum values acceptable for elements assembly.

The British Civil Airworthiness Authority reports the following definition [73]:

Factors of Safety (for static strength) - Design factors (*proof factor* and *ultimate factor*) to provide for the possibility of loads greater than those expected in normal conditions of operation, uncertainties in design and variations of structural strength, including variation of strength.

Loads are defined as [74]:

limit load is the maximum load that the aircraft is expected to experience in normal operation.

proof load is the product of the limit load and the *proof factor* (usually between 1.0 and 1.25).

ultimate load is the product of the limit load and the *ultimate factor* (usually equal to 1.5 unless otherwise specified).

Another important observation is that if the load is supported mainly by the skin, plates buckling would cause the whole load to be transferred suddenly to the spars which, if not properly dimensioned, might not be able to sustain the load. Thickening the spars, on the other hand, would increase the stiffness of the model further reducing the already moderate deformation (the maximum tip displacement computed never exceeded 10 millimetres even reducing the safety margins to one). Although aircraft industries usually assume a safety margin equal to one (or even lower) at limit loads when dimensioning plates for buckling, the final strategy adopted for the *RIBES* wing was to approach the design in a conservative way thickening the spars and assuming a safety factor between 1.2 and 1.3 on maximum load at buckling onset. With this

view, two plates 4 millimetres thick were added in the root region on the front spar where concentrations of stresses were observed (figure A.5 in appendix). Table A.1 in appendix lists the elements of the final wing configuration and their main properties.

Verification of the model geometry

The final assembled model was measured by a HEXAGON metrology electronic harm (figure A.9 in appendix) in order to verify the correctness of the external shape. Some differences from the nominal geometry were observed.

The assembly process was particularly complex. The forming of the leading edge skin panel, in particular, was difficult due to the relative high thickness of the sheet metal with respect to the low leading edge radius. The final assembled model evidenced the higher differences from the nominal geometry in this region. After some aerodynamic verifications, it was considered the disagreement not to affect the measurements considering the purpose of the test campaign. Figure 5.9 compares the nominal and the measured geometries, at the 75% of the span, together with the 2D pressure distribution at four degree of incidence. The check was also performed at high incidence in order to verify that the peak of the minimum C_P do not exceeds -8 in the range of measurements we are interested in. The evaluation of the high lift performance of the wing is not, in fact, object of interest of the planned tests.

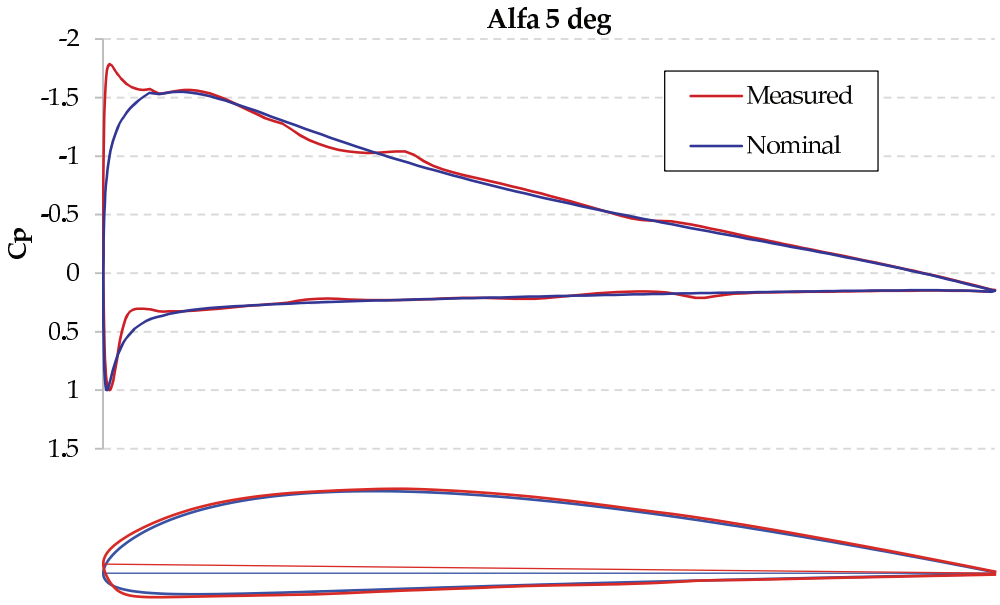

Figure 5.9: *RIBES - verification of the measured airfoil.*

As evidences in figure 5.9, the difference between the nominal and the measured geometry involved also a disagreement in the reference leading edge location (assumed as the point, on a reference section, located at the maximum distance from the trailing edge). The reference chord, on which the angle of incidence is refereed, was then

slightly rotated in order to restore a coherent reference system (the difference between the two references was around 0.6 degree).

Model instrumentation

The model was instrumented with 81 pressure taps along 6 sections. Table A.2 in appendix lists their location and their number per section. The pressure was measured around the whole airfoil at 37.5% and at 75% of the span respectively by 39 and 26 pressure taps. Four pressure taps are positioned on the other listed sections. This choice allow to provide two complete pressure measurements and an indication of the spanwise load distribution with a reasonable number of channels. Figures A.10 and A.11 in appendix show the pressure taps locations on the wing and detail the installation of the tubes on the skin plates.

In order to verify the stress state of the structure under load, twenty-five (16 uniaxial *Tokyo Sokki Kenkyujo FLA-3-23-5LT* plus 3 rosettes *Tokyo Sokki Kenkyujo FRA-3-23-5LT* with 3 signals) strain gauges have been installed on the wing model. The positions were selected according to the solutions of the preliminary FEM analyses. Figures A.12 and table A.3 in appendix show the positions and lists the characteristics of all sensors (rosettes are in bold font). The three channels rosettes measure the strain along three directions (y direction and ±45 degrees) allowing to define the complete state of strain including possible diagonal tension states. Figure 5.10 details the installation of rosettes and unidirectional sensors. The left figure refers to the rosette located on the lower skin panel, the right one shows the rosette in the middle of the front spar, close to the root rib, and the two unidirectional strain gauges on the spar stiffeners.

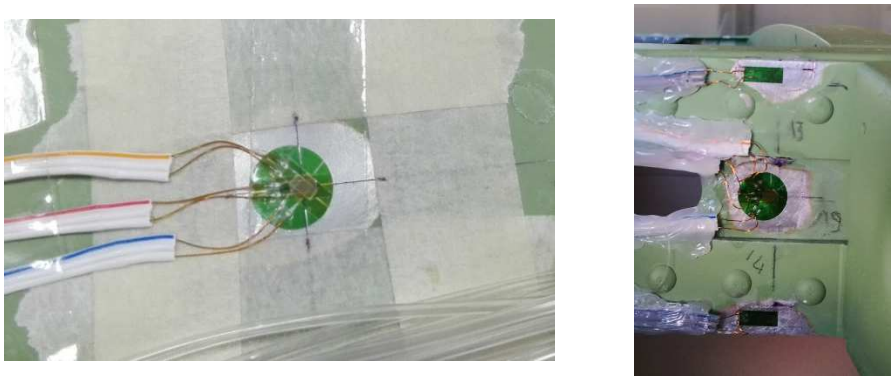

Figure 5.10: *RIBES - installation of strain gauges.*

The installation of strain gauges are operated, after cleaning and sanding the surfaces, by glue and catalyst. The nominal resistance of sensors is 120 Ω with a declared uncertainty by manufacturer of ±0.5%.

5.1.2 Test facility

The wind tunnel, in which the tests were performed, was the low speed facility of the university of Naples "Federico II" (figure 5.11). It is a closed circuit with a test section

2 meter wide. The airflow speed limit is 45 m/s. The balances measurement limits are 1000 N for the lift and 200 N for the drag. The turbulence level is in the order of 0.1%.

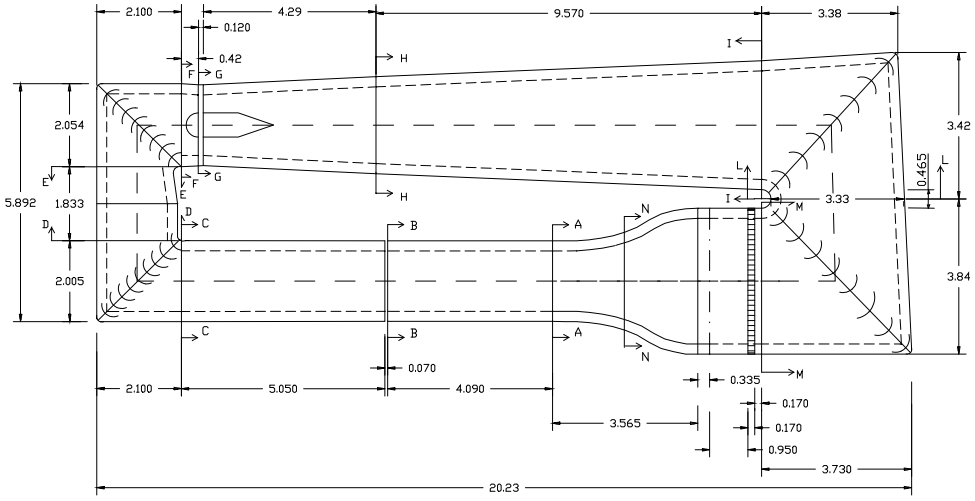

Figure 5.11: *RIBES - circuit of the wind tunnel test facility.*

The model is installed on the side wall of the test section as a cantilever (figure 5.12). The test matrix is planned to focus the attention around the design lift coefficient ($C_L = 0.7$). Transition trips were located before 5% of the chord on both side of the model in order to guarantee a fully turbulent boundary layer (figure A.13 in appendix shows the zig-zag tape used to set the transition during preliminary installation tests). Lift, drag, moment and pressure coefficients have been measured in all test matrix runs. Strain gauges measurements and deformation visualization were reported at the most significant polar points.

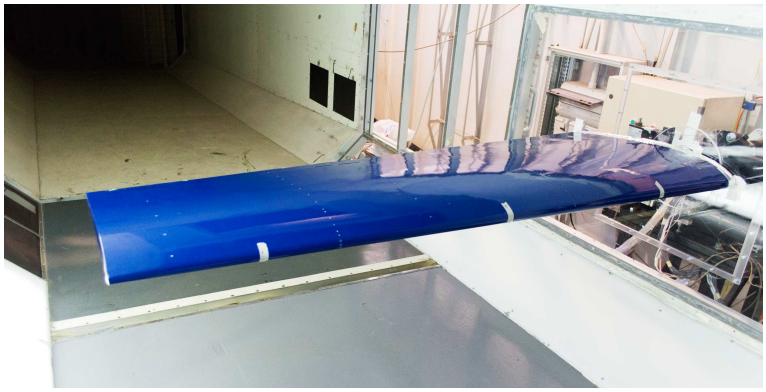

Figure 5.12: *RIBES - wind tunnel model installation.*

The flow speed of the tests ranged between 30 and 40 m/s to which correspond Mach numbers approximatively from 0.1 to 0.12. Referring to a model MAC of 515 mm, the Reynolds number ranges between 1 and 1.4 millions. Higher speed were not investigated due to the excessive loads generated on the model.

The displacement was measured detecting, by photogrammetry and laser scan, the position of a set of markers located on the wing surface. Figure A.14 shows the measurements of the wing tip displacement. In order to correct the measurements from the effect of deformation of the supporting system, the inclination of the balance was measured during the test (figure A.15 in appendix) and used to restore the wing measured displacement to the value it would assume if rigidly constrained. Further refinements of correction were adopted detecting the deformation of the support by applying an inclinometer at the root structure of the wing.

5.2 Setup of FSI numerical models

A 2-way and a modal analysis procedure, similar to those implemented and validated against the *P1XX* aircraft wind tunnel model, were here setup and validated against the *RIBES* wing measurements. In this case the attention was focused on the structural aspects of the test case. No coupling with aerodynamics is, in fact, expected since no sweep angle is present. Furthermore, even though the high camber of the airfoil causes to generate a significant moment coefficient, the high torsional stiffness of the model suggest not to expect appreciable wing tip variation of incidence under load.

The mapping procedure adopted to transfer loads from the CFD to the FEM domain, in the 2-way workflow, was the *RIBES* module described in section 2.3.2 which reduces to zero the errors on forces.

5.2.1 Measured model reconstruction

Eight sections of the manufactured model were measured from root to tip including the stations of the pressure taps lines. A CAD model was generated from the measured cloud of points. The procedure consisted in approximating the eight sets of measured points (one per section) by NURBS curves whose parameters (order, control points and knot vectors) were selected using an in-house developed optimization procedure in which the objective function was the minimization of the maximum distance between the curves and the input points. The search criterion adopted was the heuristic simplex based algorithm of Nelder-Mead [75]. The curves maximum deviation from the measured geometry was contained within half millimetres maintaining the continuity on the third geometric derivative and acceptable waviness on curvature (figure 5.13).

A sweep surface, interpolating the eight curves, was used to generate the wing skin. An acceptable spanwise quality of the surface was obtained but, since no measurements were performed along the span, the quantification of the deviation from the real model between sections was not possible. We are, anyway, confident that the sections similitude and their spanwise density are sufficient to ensure a reasonable accurate real model reproduction.

The internal structure topology was regenerated, in form of surfaces neglecting the elements thickness, starting from the CAD model of the nominal geometry and match-

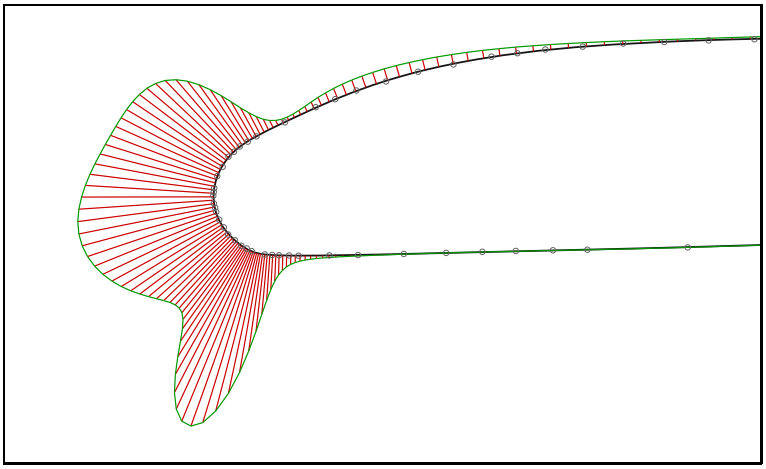

Figure 5.13: *RIBES - detail of a CAD reconstructed model section.*

ing the external loft surface generated to approximate the measured wing geometry. With this procedure, a coherence between CFD, FEM model and real geometry should be guaranteed. Figure 5.14 shows the generated 3D CAD model. The blue translucent surfaces are used in the CFD model while the red entities refer to the internal reconstructed structure.

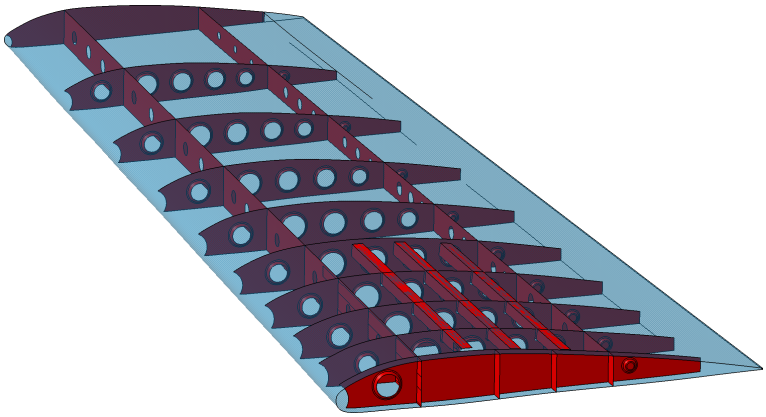

Figure 5.14: *RIBES - regenerated CAD model for numerical analyses.*

5.2.2 CFD analysis

The experimentally measured coefficients were corrected from the effects of wall blockage. The CFD numerical domain was then generated replicating the free-flight conditions. A multiblock H-C structured mesh topology, with hexahedral elements, was generated (figure 5.15). The pressure farfield boundary condition was set on surfaces located 50 MAC in front, on the top, on the bottom and on the side of the model. The pressure outlet surface is 60 MAC downstream the model. The grid is composed by 3.2 million of elements. The boundary layer was solved up to the wing surface. The

first layer of cells was set to ensure Y^+ lower that one. The layers growth rate from the wall is in the order 1.2. About 200 cells are distributed on the wing sections and 80 spanwise. Compressible RANS computations, using the pressure based solver, were performed adopting a coupled pressure-velocity scheme and second order spatial discretizations.

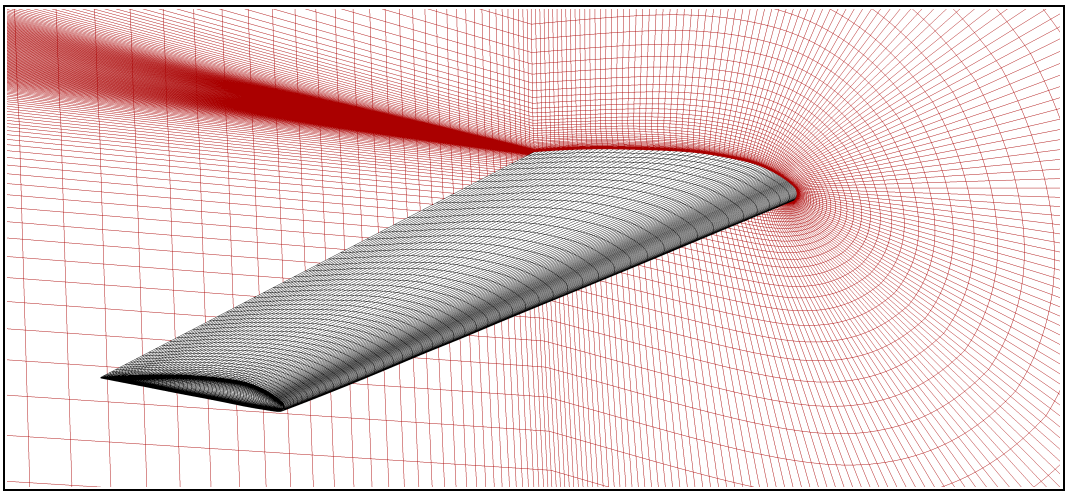

Figure 5.15: *RIBES - CFD computational domain.*

The wing polars of the rigid model were computed at $V = 40$ m/s. The convergence of the computations was very fast. Three hundred iterations were sufficient to obtain a converged solution at zero incidence (figure 5.16). The following points of the polar were computed restarting the runs from the previous solutions and increasing the angle of attack. In those cases 100 iterations were enough to converge.

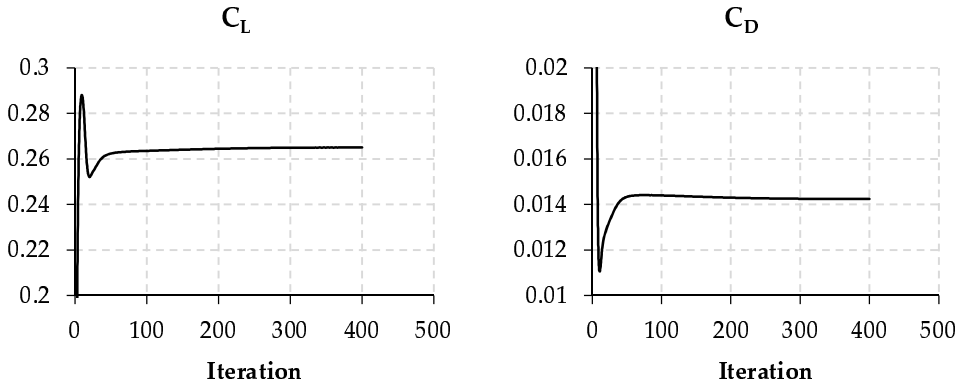

Figure 5.16: *RIBES - coefficients convergence histories at $\alpha = 0$ deg.*

5.2.3 FEM model and modal analysis

The FEM mesh was generated using *ANSYS Meshing*. It is composed of 97000 shell elements distributed on surfaces extracted from the faces of ribs and spars and on the reconstructed wing wet surface. The spar caps are joined to the skins linking the common nodes at the locations of the fasteners. The same procedure was adopted to join the stringers and the root rib to the skin. Figure A.18 in appendix reports the map of the modelled junction points. In the case of the front spar caps, the discrete junction involved the leading edge skin, the lower and upper panels (as on the real model). Figure 5.17 sketches the plates overlap in the upper cap area of the front spar. The other ribs caps were not modelled. Ribs and trailing edge skin are simply continuously constrained to the skin. This model is probably not correct but it was assumed this simplification not to affect significantly the solution.

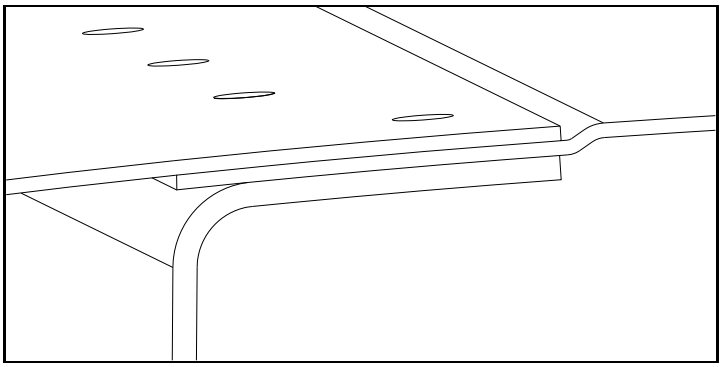

Figure 5.17: *RIBES - sketch of plates overlap in the front spar caps area.*

The properties associated to the elements correspond to the thickness of the several wing elements. The wing is constrained at the central web in the root rib location where the real model is connected to the balance by the tubular rod. Figure 5.18 shows the FEM model of the wing. The green area of the root rib highlights the cells where constraints are applied.

The *P1XX* wing model, described in the previous chapter, was a fully steel-made structure characterized by clearly identified global modal shapes. The *RIBES* wing structure is much more complex. It is then reasonable to expect more complex modal shapes and vibrating behaviour of the structure. A deeper modal analysis was then performed computing up to 50 modes. The aim was to classify mixed modes by inspecting the fraction of system mass participating in each eigen shape by the computation of their effective mass participation factor. This evaluation was performed for sake of completeness since, according to what evidenced by the results of the modal FSI analysis of the *P1XX*, it was showed not to be necessary to reach a large amount of participating mass fraction in FSI analyses. This criterion is then not used to determine the opportune dimension of the modal base. As already shown, in fact, the primary procedure to provide, in absence of a complete 2-way FSI result, the indications on the minimum number of modes to adopt in the modal FSI analysis implementation is the modal base qualification procedure described in section 4.4.1 (the modal qualifica-

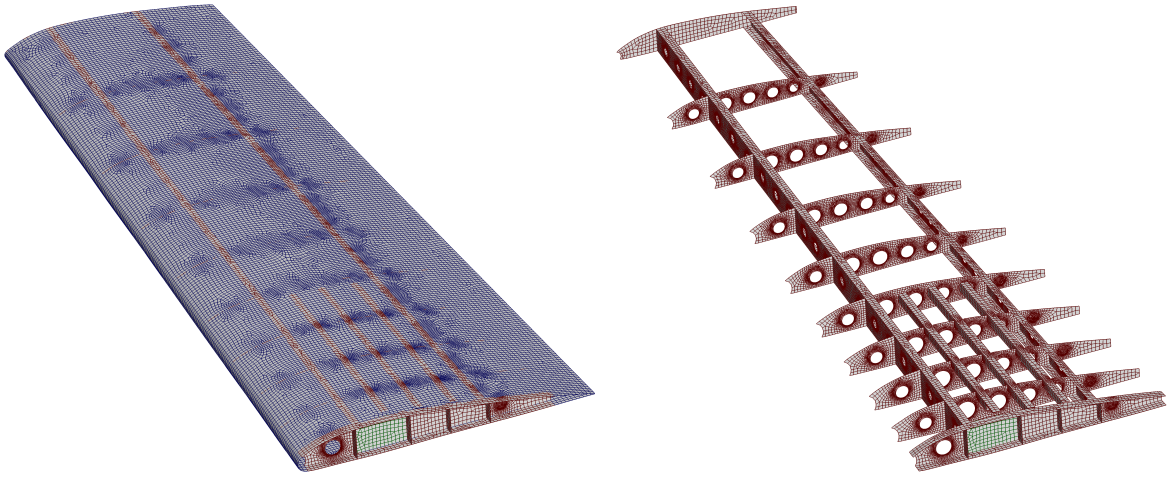

Figure 5.18: *RIBES - FEM model of the wing structure.*

tion was not repeated for the *RIBES* wing since it is provided by the direct comparison between the modal and the 2-way FSI solutions).

The translating and rotational modal mass contributions along X, Y and Z direction, taking as reference a point in the middle of the root web, are plotted in figure A.16 in appendix. The mass fraction of the first mode contributes, alone, of more than 50% of the total mass on wing translation in vertical direction. The second mode is almost the only contributor of rotation in forward direction. Beside individual modal and effective mass participation factors, it is more indicative to analyse the cumulative contribution of each mode by the progressive summation of the mass fraction of each mode. The sum of the fractions contributions are plotted in figure 5.19 for the vertical translation and rotational factor along spanwise direction. The first mode has clearly the highest contribution on translation. The highest contribution to rotation is provided by the third mode. As evidenced by the plot in figure A.16, in fact, its single contribution is close to 30% of the total mass. After the first, the major increments in rotation are provided by the third, the ninth and the fourteenth mode. Modes from 15 to 28 give modest contributions. The contribution of modes higher that 28 is negligible. Major steps on rotation contribution are evidenced by the modes number 1, 3, 4, 14, 16 and 26. No significant contributions are provided by the following modes.

It was decided to limit the number of mode to extract to eight. From the aerodynamic point of view, since no coupling with structural deformation is present, the number of modes to be selected is irrelevant (with the exception of the influence on torsional deformation which is, however, assumed to be extremely limited). Eight modes, which as evidenced by figure 5.19 allow to reach a total mass participating to bending and torsion respectively of 63% and 55% of the wing mass, were considered sufficient to qualify the comparison, in term of structure global deformation, with the displacement field computed by the 2-way FSI analysis. With the view of the modal approach to represent a "lighter" environment compared to a full 2-way coupling, in fact, the confirmation of the validity in adopting a potentially poorly populated modal base is

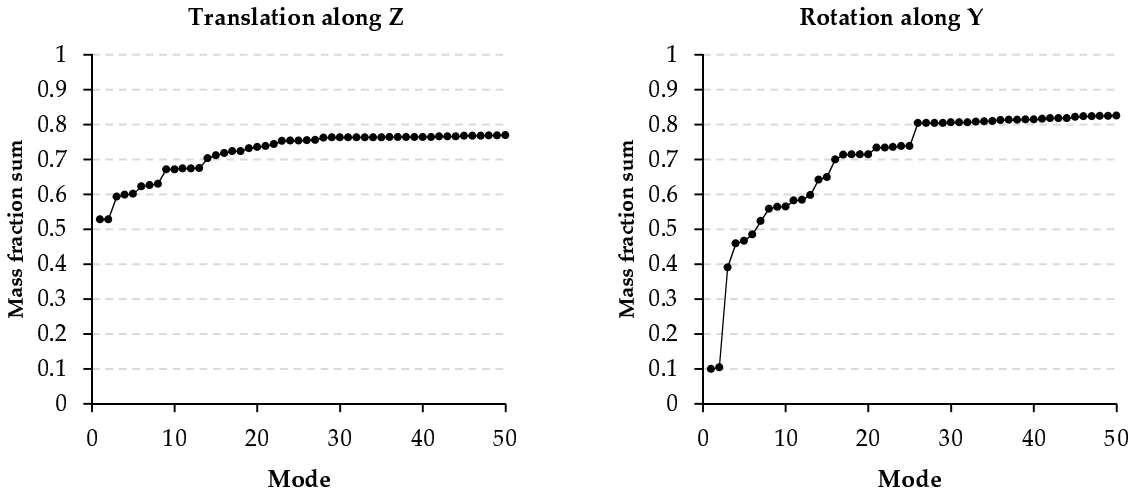

Figure 5.19: *RIBES - Sum of modal mass fraction of first 50 modes.*

an information that helps to explore the minimum limit of a modal setup.

Shapes and frequencies of the first eight modes extracted are reported in appendix in figure A.17. The first and the second are graphically confirmed to be purely global bending modes, respectively in vertical (Z) and horizontal direction (X). All the other modes present a combination of global and local effects. Modes 3 and 6 present, in addition to the local components, bending and torsional shapes. In modes 4, 5, 7 and 8 the global components are mainly torsional.

The total mass of the FEM model, computed by the software, is 4.59 kilograms. The mass of the geometric model, computed by a CAD system, is 4.39 Kg. This difference is due to the simplified modelling adopted in the region of the wing constraint. The root web, where the wing is connected to the balance by the tubular rod, has a complex shape with several irregular reinforcements. Since it is assumed this part to be particularly stiff, it was simply modelled as a surface 20 millimetres thick. This mass overestimation, however, belong to a surface on which constraints are applied to the mesh nodes. There is then no effect on solutions. An aspect that, conversely, would have an influence, if a dynamic analysis had to be performed, is the difference between the mass of the numerical model and the real mass of the tested wing. The weight of the real model is, in fact, around 5.8 kilograms. The difference is devoted to all elements that were not included in the FEM model (rivets, linchpins, tubes, wires, sensors, primer, paint, etc...) Such a difference might affect the correctness of the computed frequencies but do not affects the computation of a steady phenomenon. The tuning of experimental modes is a delicate task and, since it was not possible to face it within the activities of the *RIBES* project, it will tackled in the future with a specific experimental campaign.

5.2.4 Mesh morphing setup

A set of source points, equally spaced by 0.2 meters each other, was defined on a box shaped bounding volume in order to limit the space of the mesh morphing action. The moving points are located on the wing wet surface. Figure 5.20 shows the domain of the RBF setup. The limiting source points are marked in red while the moving centres, belonging to the wing, are in green.

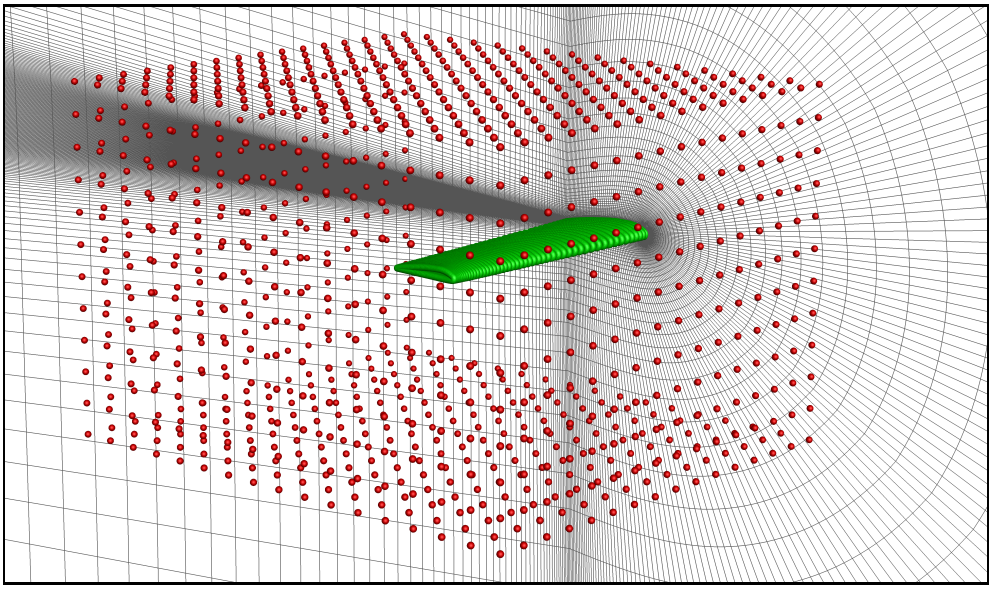

Figure 5.20: *RIBES - domain defining the RBF fitting problem.*

The setup of the RBF problem was the same for both 2-way and modal FSI implementation. It was performed by a two-step approach similar to the one adopted in the implementation of the *P1XX* domain morphing problem (described in section 4.2.3). The first step consisted in a small RBF problem, limited to the wing geometry, in which the displacement field was prescribed by the solution of the FEM analysis (in the 2-way FSI implementation) or by the selected normalized modal shape (in the setup of the RBF modal base) resulting from the structural modal analysis. The second step defines the limits of the morphing domain and prescribes the RBF solution of the first step to the wing.

The RBF problem was based on 30160 source points on the wing (which correspond to the number of surface grid nodes) and on 1164 points on the bounding domain. The RBF system was solved in 62 seconds on a workstation with 20 CPUs (2 processors *Intel Xeon* E5-2680 2.8 GHz with 10 cores each) and 128 GB of RAM. This action has to be performed only once, during the setup phase, for each RBF solution. The fitting action, amplifying one RBF solution, required 40 seconds. This is the action that has to be performed during the 2-way FSI computation. In the modal approach, the required time to morph the mesh raises with the number of modal shapes to be combined and amplified. The maximum effort, required by adopting a modal base with eight shapes, was 3 minutes and 31 seconds. This effort is not required during the progress of the

CFD computation since the modal solutions are initialized and stored in memory at the begin of the run. The domain update of the CFD aeroelastic model is then extremely fast (order of a few seconds and, in general, faster than one CFD iteration).

5.3 Solutions of elastic models

The rigid model was characterized at V = 40 m/s and at incidences ranging from -3.4 to 10.6 degrees. The comparison between the computed polars of the rigid model and the experimental data is reported in figure 5.21.

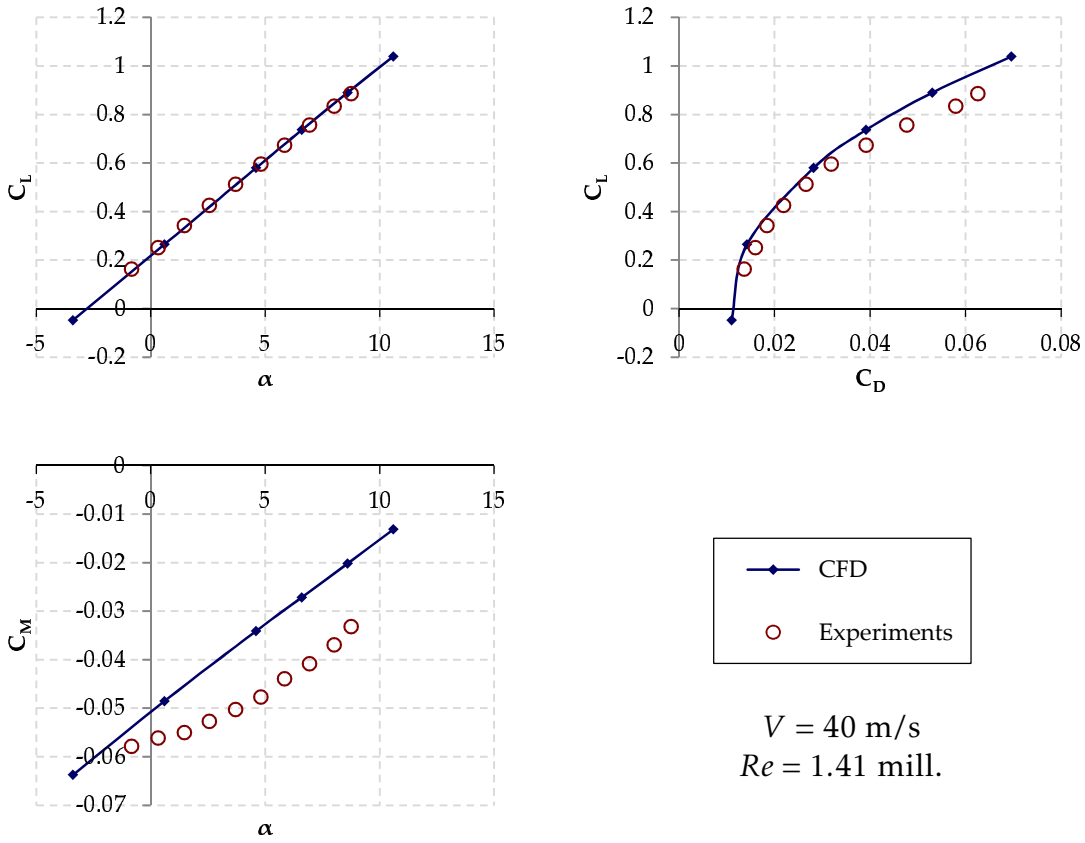

Figure 5.21: *RIBES - comparison between rigid CFD solutions and experiments.*

A very good agreement was obtained in the lift curves slopes and values. A relative constant underestimation of the drag, in the order of 13-15%, was observed along the polar curve. The reason might be devoted to the additional drag introduced by the transition trips which, in order to ensure transition at low Reynolds numbers, must have a relatively high thickness. The disagreement is more evident when comparing the moment coefficients.

The two plots in figure 5.22 report the comparison between the measured and the computed pressure coefficients at the stations 3 and 5 (see table A.2 in appendix). A

good agreement was observed at both stations along the whole airfoil with the exception of the value measured by one pressure tap located close to the leading edge in the section 3. The measurement hardware was inspected and verified but no malfunctioning was noticed. The reason of this disagreement is not clear. An hypothesis might be to devote it, again, to the disturbance caused by the proximity of the transition tape.

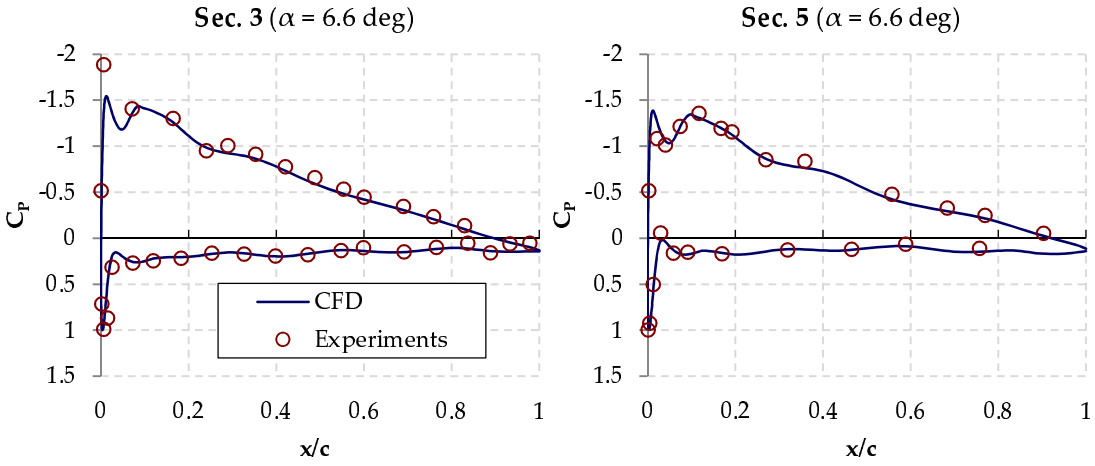

Figure 5.22: *RIBES - comparison between computed and measured C_P (C_L = 0.736).*

Figure 5.23 reports the comparison of the spanwise pressure coefficients at the constant streamwise stations x/c = 0.17 and 0.56.

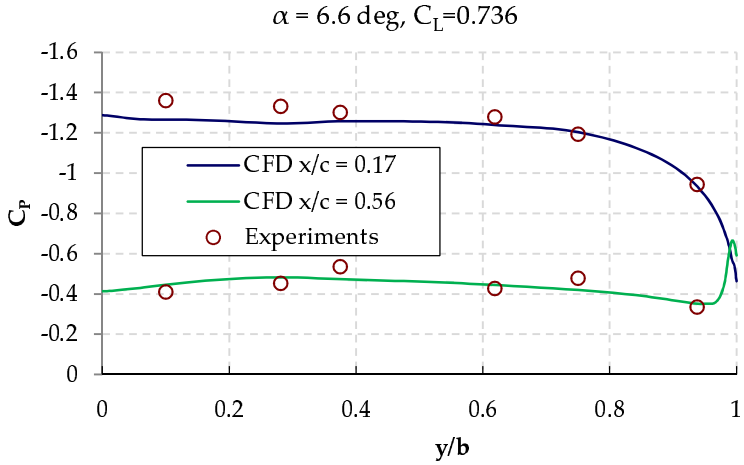

Figure 5.23: *RIBES - comparison of spanwise C_P at two stations.*

The aeroelastic verification was performed at a wing incidence (of the numerical model) of 6.6 degree to which corresponds the target design lift of 60 kilograms. The flexible models provided, as expected, aerodynamic solutions extremely similar to the solutions obtained with the rigid model confirming that the deformation has no influence on aerodynamics. The variation of coefficients of all solutions was practically insignificant (lower than 0.0006 for lift and lower than half drag count for drag). One

iteration of the 2-way cycle described by the workflow of figure 3.3 was enough to provide the final solution of the elastic model. Table 5.1 compares the aerodynamic coefficients computed at $V = 40$ m/s and at $\alpha = 6.6$ degrees by the several models.

Table 5.1: *RIBES - coefficients at $V = 40$ m/s and $\alpha = 6.6$ deg.*

Case	C_L	C_D	C_M
Undef.	0.73635	0.03917	-0.027158
2-way	0.73668	0.03917	-0.027968
1 mode	0.73656	0.03916	-0.0284
2 modes	0.73656	0.03916	-0.028347
3 modes	0.73686	0.03918	-0.028665
4 modes	0.73689	0.03918	-0.028658
5 modes	0.73684	0.03918	-0.028655
6 modes	0.73654	0.03915	-0.028408
7 modes	0.73649	0.03913	-0.028275
8 modes	0.73649	0.03914	-0.028289

Table 5.2 and figure 5.24 report the modal coordinates computed adopting a modal base with eight shapes. The first bending moment is by far the most dominant. The magnitude of all other modes do not exceed the order o 2% of the first mode.

Table 5.2: *RIBES - values of modal coordinates.*

Mode	Modal coordinate q
1	0.0075421296
2	0.000084563813
3	-0.000091689029
4	0.0000089290608
5	-0.000027857336
6	-0.0001328897
7	0.000098014211
8	-0.000014453632

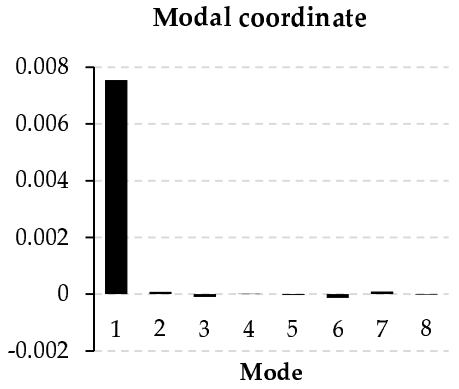

Figure 5.24: *RIBES - 8 modes modal coordinates.*

The qualification of the modal base is provided comparing the displacements estimated by the 2-way FSI analysis and by the modal FSI numerical configuration adopting a modal base constituted by eight modes. Such comparison is reported in figure A.20 in appendix where the modules of the vectors obtained from the difference of the two displacements are graphically evidenced by colour plot. The maximum difference

between the two solutions is lower than half millimetre in an area localized on a panel behind the rear spar between the ninth and the tip rib.

5.3.1 Structural response of the elastic models

The structural responses estimated by the two numerical models were compared with the experiments in term of stresses, in the locations of strain gauges, and displacements of a set of points identified by markers located along the wing front spar on the lower surface. The optical displacements measurements were corrected generating a reference system linked to the wing root obtained subtracting the deformation of the measurements chain (balances and supports). The procedure consisted is measuring the displacement and the inclination of the structure supporting the wing to the balance and in using these data to update the reference system. The model rotation at the root location was measurement by an inclinometer linked to the wing root rib in the junction with the balance tubular rod. Figure 5.25 compares the measured with the FSI models estimated displacement. Table 5.3 reports the numerical values and the spanwise locations of the markers positioned on the front spar lower cap.

Table 5.3: *RIBES - markers location and displacements values.*

	Exp.	2-way	Modal
y	Δz	Δz	Δz
mm	*mm*	*mm*	*mm*
324	0.41	0.72	0.63
462	0.72	1.26	1.13
600	1.22	1.89	1.74
755	1.7	2.71	2.54
909	2.31	3.59	3.43
1055	3.01	4.49	4.34
1204	3.74	5.42	5.32
1398	5.03	6.67	6.63
1593	6.3	7.94	7.94

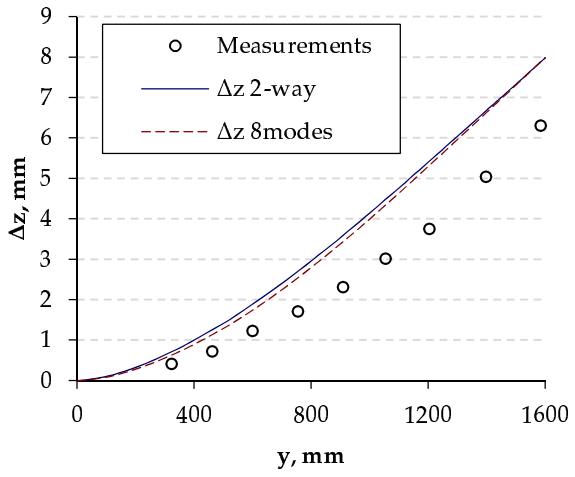

Figure 5.25: *RIBES - displacements comparison.*

The 2-way and the modal FSI methods estimated a very similar deformation. They, however, both overestimated the wing displacement under load. An hypothesis, to justify this disagreement, might be related to the panels junctions modelling. The simple assumption of connection by points do not account for friction and interference that are present along the junctions surfaces leading, probably, to model a structure more flexible than the real one.

Stress state verification

The set of installed strain gauges provided a map of the stress state of the structure. All the unidirectional sensors were aligned in spanwise direction. Unfortunately a failure occurred on strain gauges number 1 so it was not possible to acquire its measurement. Figures from A.21 to A.25 in appendix report the visualizations of the normal stresses, in the Y direction, resulting from the FEM analysis in the final cycle of the 2-way aeroelastic analysis procedure. The sensors location are marked by red circles.

Table 5.4: *RIBES - measured and computed σ_y at strain gauges location.*

ID	**position**	**measured σ_y** *MPa*	**FEM σ_y** *MPa*
1	front spar	n.a.	∼ -47
2	front spar	58.1	∼ 46
3	rear spar	-1.2	∼ -1
4	rear spar	0.2	∼ 2
5	front spar	-17.5	∼ -16
6	front spar	18.2	∼ 15
7	rear spar	-9.5	∼ -7
8	rear spar	11.5	∼ 9
9	front spar	-12.2	∼ -11
10	front spar	12.3	∼ 10
11	rear spar	-8	∼ -8
12	rear spar	7.5	∼ 6
13	front spar thickening	-15.6	∼ -38
14	front spar thickening	15	∼ 36
15	upper skin	-143.2	∼ -21
17	upper skin	-31.5	∼ -15

The values of stresses extracted from the FEM model are compared to the measurements in tables 5.4 (for the unidirectional strain gauges) and 5.5 (for the rosettes). In general, a reasonable matching between measured and computed stresses was observed. Significant disagreements are, however, present in locations close to the root region where higher stress gradients are present. In particular, the two strain gauges located on the front spar thickening (numbers 13 and 14) and the ones located on the upper skin (number 15 and 17) showed the largest differences. Concerning the two sensors on the front spar, the FEM model significantly overestimated the stress values. In the FEM configuration, no junction between reinforcements and spar is modelled. One of the hypotheses to justify such differences might be that the load is only partially transferred to the two elements due to microslips occurring between the riveted elements. The sensors on the upper skin, conversely, reported a stress state much higher

than computed. The combination of the two sets of information (strain gauges on the front spar and on the upper skin) would suggest that the distribution of the load between the front spar and the skin was not properly captured. Further investigations will be necessary to better understand the reason of such disagreement. Uncertainness might be also introduced by the junction between the two front spar thickening and the root rib. The elements are, in fact, linked by two linchpins (with a diameter of 7.92 mm) which were not modelled in the numerical configuration.

Principal stresses are computed according to the following equations:

$$\sigma_1 = \frac{E}{(1-\nu^2)}(\epsilon_1 + \nu\epsilon_2), \qquad \sigma_2 = \frac{E}{(1-\nu^2)}(\epsilon_2 + \nu\epsilon_1)$$

where the principal strains ϵ_1 and ϵ_2 are computed as

$$\epsilon_{1,2} = \frac{\epsilon_a + \epsilon_c}{2} \pm \frac{1}{\sqrt{2}}\sqrt{(\epsilon_a - \epsilon_b)^2 + (\epsilon_b - \epsilon_c)^2}$$

The equations above refer to a rosette with three strain gauges oriented at 0, 45 and 90 degrees. The principal angle is referred to the strain gauges b and is expressed by

$$\phi = \frac{1}{2}\arctan\left(\frac{\epsilon_a - 2\epsilon_b + \epsilon_c}{\epsilon_a - \epsilon_c}\right) + 45$$

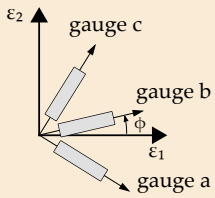

Table 5.5: *RIBES - principal stresses and directions (respect y) at rosettes location.*

	measured	**FEM**
	rosette 16 (lower skin)	
σ_1	58.14 MPa	~ 36 MPa
σ_2	3.95 MPa	~ 11 MPa
ϕ	65.25 deg	~ 77 deg
	rosette 18 (upper skin)	
σ_1	-4.58 MPa	~ -4 MPa
σ_2	-32.28 MPa	~ -20 MPa
ϕ	7.15 deg	~ -6 deg
	rosette 19 (front spar)	
σ_1	8.62 MPa	~ 11 MPa
σ_2	-11.16 MPa	~ -14 MPa
ϕ	45.33 deg	~ 43 deg

Conclusions

Methods for Fluid-Structure Interaction analyses based on high fidelity numerical solvers are considered the most accurate approach to simulate aeroelastic phenomena. The cutting-edge technology, nowadays, consists in coupling RANS codes with FEM solvers. Both technologies are very well consolidated analysis methods widely used in many fields of engineering and extensively adopted in several aspects of design. Engineers have a deep confidence in their accuracy and range of applicability. When coupled to face FSI problems in the so called *2-way* procedure, however, several issues affecting the efficiency of the workflow, might arise. The coupling consists in iterating between FEM analyses, in which the loads are derived from the aerodynamic solution, and CFD computations, in which the domain is adapted to the deformed geometry estimated by FEM models. The points relate to the strategy to be adopted in the implementation of the workflow that governs the CFD-CSM closed loop and in the methods used to enhance the information exchange between the two numerical environments. The loads transfer process from the fluid dynamic solution to the FEM domain requires an interpolation procedure that, in general, introduces errors that depend on the algorithm adopted and on the differences between the two discretizations in the common boundary regions. This error was showed to be eliminated (on forces resultants) adopting opportune corrective coefficients as in the mapping method developed within the EU *RIBES* research project. The trickiest aspects of FSI analyses remains the method through which to receipt, within the CFD environment, the information about the shape the model assumes under aerodynamic loads. A procedure able to adapt the computational domain to the solution of the FEM solver is required. Among the several strategies available in literature, the most promising to face this problem is recognized to be the mesh morphing approach using Radial Basis Functions.

In the work here presented, an RBF mesh morphing technology was used to implement high fidelity FSI analysis methods that were applied to the static aeroelastic analysis of aircraft wings. In addition to a traditional CFD-CSM coupling, a method based on the modal shapes superposition was implemented and validated. The assumption at the base of the modal approach consists in representing the model deformation by a combination of a limited number of natural modal shapes of the structure. The setup of the modal FSI analysis procedure is then based on a preliminary modal FEM computation aimed to the extraction of the structural natural modal shapes and frequencies of the object under investigation. A set of RBF solutions, one for each selected modal

shape, is then computed and stored to constitute the mesh morphing database used to generate the parametric mesh morphing criterion. The wing deformation is applied amplifying the RBF field according to the modal forces computed during the CFD iterations. The main advantage of the procedure is that an intrinsically CFD flexible model, fully working within the fluid dynamic solver environment, is generated. No further iterations with the structural solver are required, nor routines or codes coupling procedures need to be developed with a clear advantage in terms of workflow robustness. The main limitations consist in the restriction of validity to linear problems and in the selection of the minimum number of modal shapes, which is unknown a priori, to be adopted in the implementation of the parametric mesh formulation.

The modal approximation allows, compared to a 2-way method, to enhance the computational performance for several reasons:

- the morphing action, once the run is initialized, is practically inexpensive;
- the mesh update is performed continuously (every prescribed number of iteration) during the CFD computation;
- the whole FSI analysis is performed within the same numerical environment and no transfers of information between CFD and CSM solvers is required;
- no CFD restarting procedures or solutions interpolations are required (on this aspect the required effort is strongly solver-dependent).

The time-to-setup of modal analyses depends on the complexity of the problem but, in general, it requires less effort compared to the setup of a complete 2-way coupling especially when implementing automatic procedures suitable, for instance, to be integrated in MDO environments.

The two FSI methodologies here described were validated against two static test cases: the *Piaggio Aerospace P1XX* mid-size business jet, a complete aircraft model tested in a transonic wind tunnel, and an half wing model, manufactured within the *RIBES* EU project and replicating a typical wing box topology, tested in a low speed facility. The aim of the first assessment was to evaluate the numerical methods capability to capture the structural-aerodynamic coupling mechanism that derives from the sweep angle of the aircraft wing. The second validation was addressed to the structural aspects of the numerical modelling. In particular, the attention was focused on the evaluation of the methods capability to face aeroelastic problems that are more representative of realistic wing structures. For this reason, the model was instrumented with a set of strain gauges to provide a map of the stress state of the wing structure to be compared with the numerical simulations outputs.

The modal bases adopted in the modal FSI analyses implementation were composed of the first six modes of the aircraft wing and of the first eight modal shapes for the half wing structure. In order to gain a sensitivity on the influence of the modal bases composition, the analyses were performed incrementing sequentially the adopted number of modes and comparing all solutions (including the 2-way) with the

experimental measurements. In both modal analysis configurations, the first modes showed to be largely the most dominant over all the others. In fact, moderate impacts on the solutions were observed when adopting more than two modes. The first conclusion is that, for lifting bodies, few modes are sufficient to support a representation of the shape deformation under load suitable to provide an aeroelastic solution having an accuracy comparable to the solution provided by a complete 2-way FSI analysis. In both validation sessions, furthermore, the 2-way and the modal based FSI analyses provided, from an engineering point of view, almost the same solutions, confirming the modal approach to be a valid candidate to setup efficient and accurate static and dynamic FSI analyses.

When the validation activity against the *P1XX* measurements was performed, the load mapping procedure developed within the *RIBES* project was not yet available. The procedure adopted at that time to transfer the pressure from the CFD to the FEM domain in the 2-way FSI analysis introduced a systematic error on lift resultants in the order of 2.5%. When comparing the 2-way with the modal solution, it was then expected a difference of a similar order of magnitude. As previously introduced, conversely, the 2-way and the modal solutions were extremely similar. Since the 2-way and the modal analyses provided very similar solutions also in the FSI analysis of the *RIBES* wing, in which the mapping procedure adopted introduces corrective coefficients that eliminate the mapping errors on forces resultants, we are induced to assume that moderate errors on vectors mapping between meshes do not affect substantially the aeroelastic analyses of lifting surfaces.

Three cycles of the 2-way closed loop were required to obtain a converged static solution in the FSI analysis of the *P1XX* aircraft model, while only one was sufficient for the analysis of the *RIBES* wing structure. The latter, in fact, is a straight wing with no sweep angle and the effect of its deformation on aerodynamic is negligible. The solutions were compared in terms of coefficients and pressure distribution with the experimental measurements. The flexibility of the *P1XX* model during tests was not verified but the strong coupling between wing deformation and aerodynamic performance allow to search an indirect confirmation of the quality of the FSI analyses comparing the aerodynamic coefficients with experiments. The solutions of the flexible models, in fact, better match the measured lift polar, but a better confirmation is provided by evaluating the behaviour of the pressure distribution. Transonic speed conditions, in fact, involve the generation of supersonic regions that recover the subsonic conditions through recompressions whose structures are typically extremely sensitive to any geometric configuration variation. The flexible models provided a description of the shock structures more coherent with experiments in terms of strengths and positions, suggesting a correct estimation of the wing deformation.

The aerodynamic verification of the *RIBES* wing polars showed a good agreement with measurements and, as expected, no effect of elasticity was observed. A slight underestimation of drag, may be due to the effect of transition trips, was observed. The validation was focused then on the structural deformation and on the stress state verification. The numerical elastic models showed to be more flexible than how evidenced by the measurements. The maximum displacement computed is in the order

of 25% higher than measurements. Although the shape and the general behaviour of the elastic models seem coherent with measurements, such a difference is higher than expected. The reason of this disagreement is not clear and further investigations will be necessary. The research of a justification might be oriented to the opportune modelling of the connections between the wing components. In the FEM configuration, discontinue junctions, linking the points of the elements meshes corresponding to the rivets location, were modelled. The shell elements belonging to the skin, for instance, were constrained with the shells belonging to the spar caps by the common nodes that were opportunely generated matching the position of the real junction lines. This simplification does not involve the modelling of the friction that occurs between skin and spar caps (induced by the preload of the rivets) and neglects the interference of the plates. Neglecting those two effects might induce to underestimate the rigidity of the whole structure.

Concerning the stress state verification, a good agreement with measurements was observed in regions far from the wing root. Some disagreements, particularly large in some cases, became evident in the areas close to the junctions at the wing root where higher gradients are present. The differences consist of a significant underestimation of the stress present on the upper skin and an overestimation of the stress state on the reinforcements nailed to the front spar. In other words, the measurements suggest that the load transfer from the skin to the spar was not properly captured by the numerical model and was, in general, numerically overestimated. The suspect is that the actual contribution of the wing elements was not properly modelled due to aspects that are ignored in the FEM configuration. A hypothesis might be, for example, the presence of microslips effects between the front spar and its reinforcements that leaded to an erroneous estimation of the load shared between the skin and the spars.

It has to be highlighted that the developed numerical aeroelastic configurations showed to be very effective. The RBF morphing approach to the FSI problem, in particular, makes the procedures extremely efficient and robust. The disagreements evidenced in the *RIBES* model analysis strictly concern aspects related to FEM modelling techniques or measurements uncertainness, which are often present in any experimental correlation, and contribute to improve the knowledge that allows to refine our analysis capability. The *RIBES* test case was setup exactly for this purpose and from this point of view it demonstrated to represent a valuable source of information. On the other side, the setup of the FSI configurations allowed to appreciate the efficiency of the RBF based FSI analyses and to focus on aspects of numerical modelling that are oriented to the accuracy improvement of the analyses.

All measurements, geometries, numerical models and solutions of the numerical/experimental activities performed within the *RIBES* project will be soon available on line (at the project web site address `www.ribes-project.eu`) to the scientific community. A web portal is under development with the wish the *RIBES* test case to constitute an enhancement for information sharing between scientists and a framework for further discussions, research activities, proposals and collaborations.

Acknowledgements

Several people have contributed to the completion of this work but the *"big architect"* of the programmes, this research is part of, was Marco Biancolini. He developed the core technology at the base of all activities of *RIBES* and *RBF4AERO* projects. I had the pleasure to work with him on topics ranging from marine to automotive and aerospace engineering and I could appreciate his wide competence in several disciplines and his uncommon capability to manage any topic, also not related to his official academic competences, with great professionalism. He is an open-minded and passionate researcher to whom I wish to express my sincere gratitude for having involved me in the several activities we share a common passion for. Thanks to him and to his expertise I had also the opportunity to extend my interests on topics other than the ones strictly related to my professional background.

During the years of my doctorate I could appreciate the competence of the colleagues I had the opportunity to work with. I wish to thank Corrado Groth for having provided the key elements of the FSI workflows and for his support (24 hours a day) on every subject related to structural analysis. I wish to thank Andrea Chiappa and Francesco Giorgetti for having contributed to the development of the *RIBES* core software (in particular the load mapping procedure used in this work) and for their support in the completion of the technical documentation of the project. I am grateful to Gianvito Apuleo from *Piaggio Aerospace* for his support on practical aspects on aircraft structural wing design. A special thank is for Emiliano Costa from D'Appollonia (coordinator of the *RBF4AERO* project), for his constant presence, for his never missing support and for his friendship. His competence, his precision and his capability to guide with equity and with the proper authority such an international, wide and heterogeneous consortium are examples to follow and were the guarantee of the success of such a big and complex project. My gratitude to the people I have been working with during the last years is particularly felt also for having constituted a group of good friends. I wish to express my gratitude to Evangelos Karelas from Hellenic Aerospace Industry (topic manager of the *RIBES* project). He was a competent guide always available and his suggestions were precious in all technical activities of the project. I wish also to express my gratitude to professor Roberto Montanari (coordinator of the doctorate course) for having given me large flexibility in the organization of my activities and for his indulgence in the moments of difficulties.

Experimental measurements are "by nature" subjected to uncertainness and unknowns that render delays in schedules *the rule* and not *the exception*. This is partic-

ularly true when dealing with models manufacturing and wind tunnel tests. In my small personal (probably unlucky) statistics, furthermore, the delays always leaded to perform tests in proximity of summer or Christmas holidays. The *RIBES* test program was not an exception and had the additional drawback to coincide with the deadline of the final delivering of this thesis. I wish then to thank Fabrizio Nicolosi from the university of Naples and all the staff of his department for their efforts in providing the necessary measurements data in time to complete this work despite the Christmas holidays.

My last thanks are for my family. I wish to thank my three years old son, whose constant presence during the final drafting of this manuscript made its completion a real challenge, and my wife for her vain effort in trying to keep him far from my desk.

Appendix

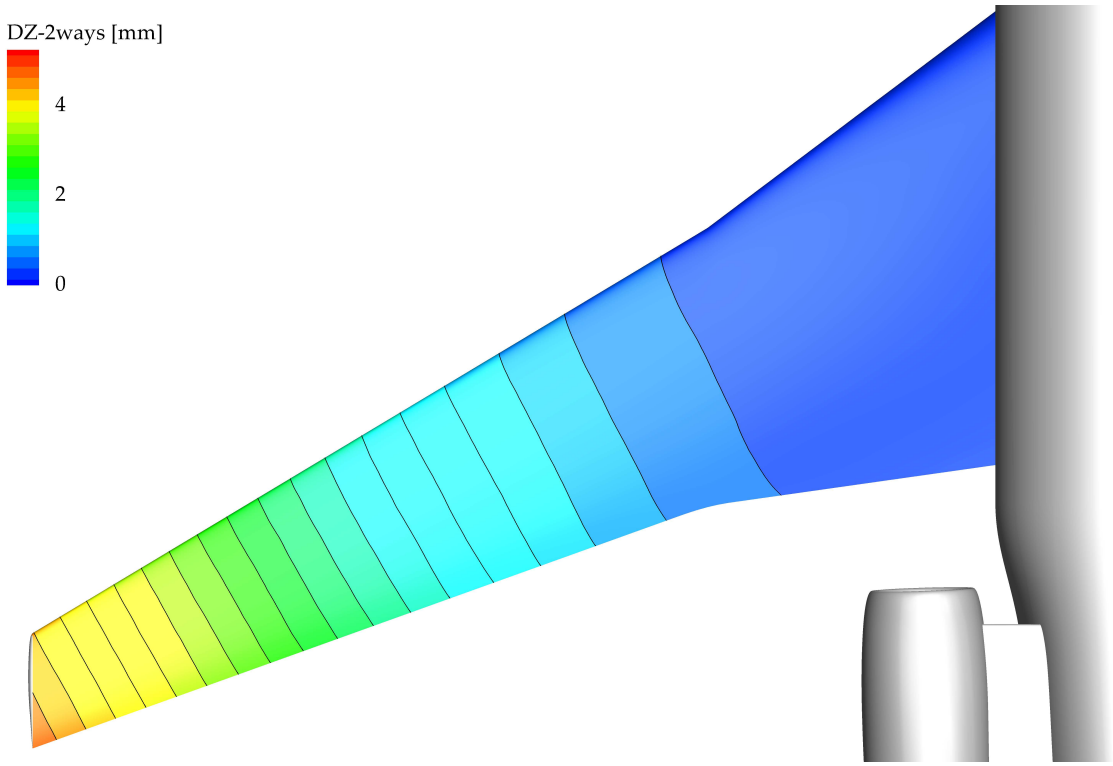

Figure A.1: *P1XX - displacement of the wing computed by 2-way analysis.*

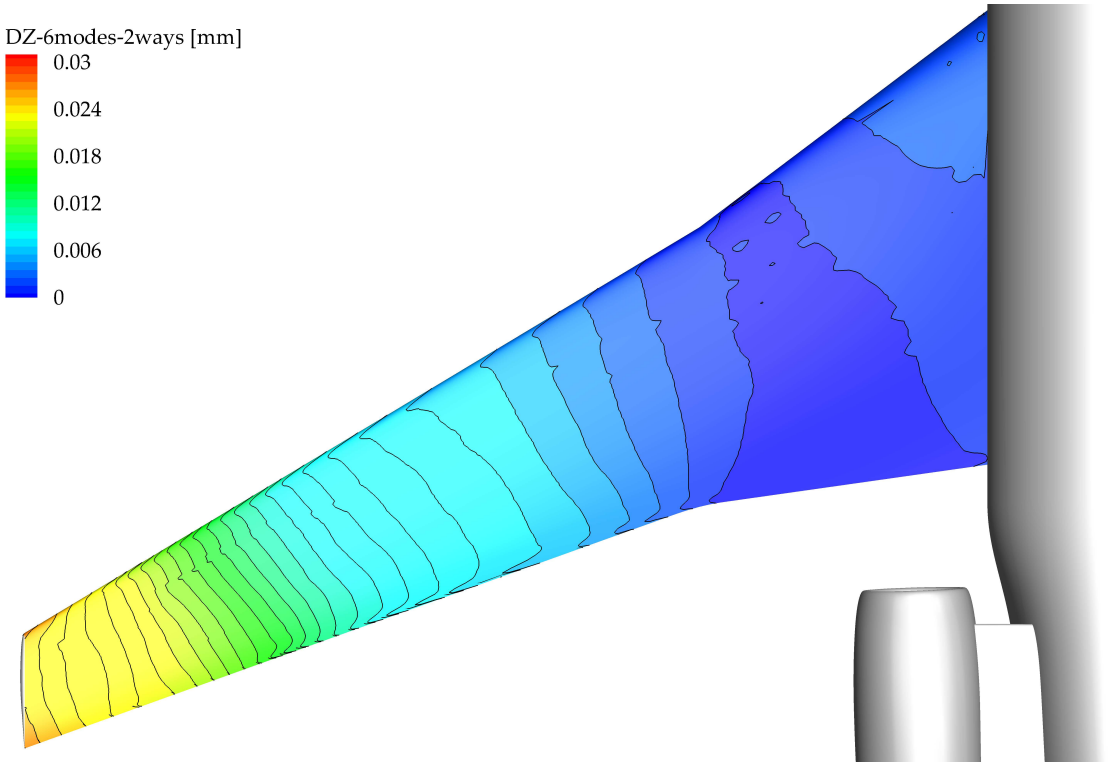

Figure A.2: *P1XX - geometric differences between elastic models solutions.*

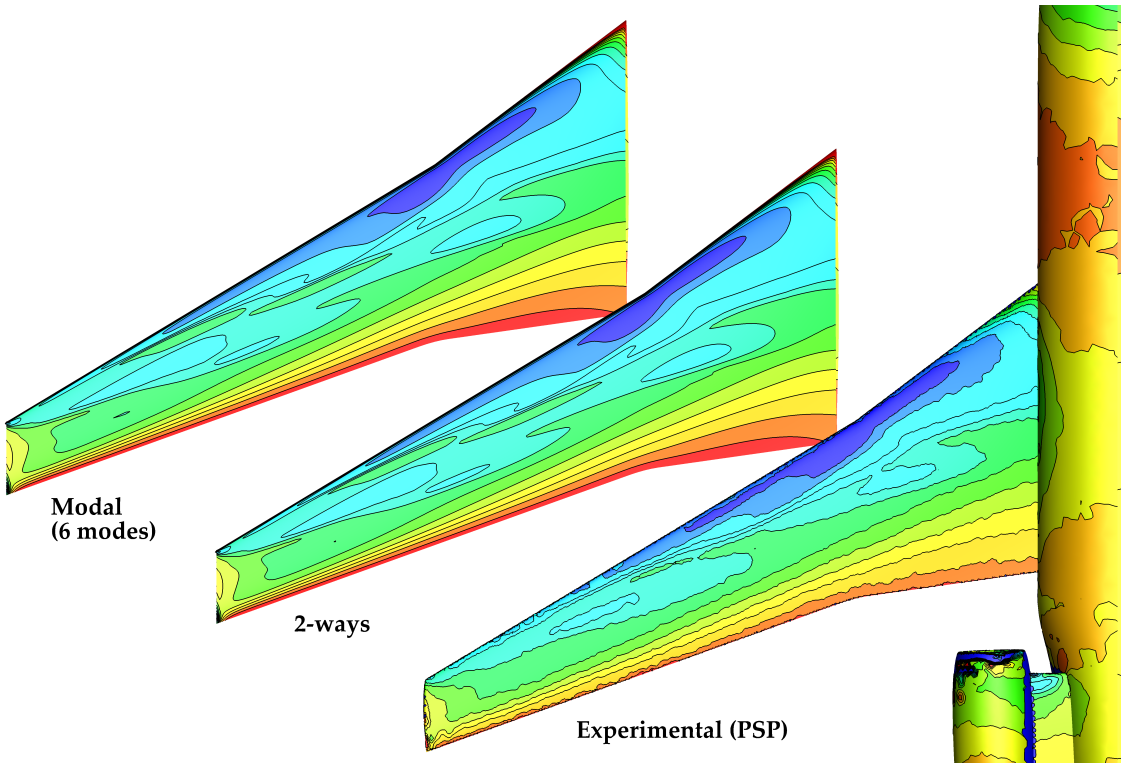

Figure A.3: *P1XX - pressure contour plots on the suction side of the wing.*

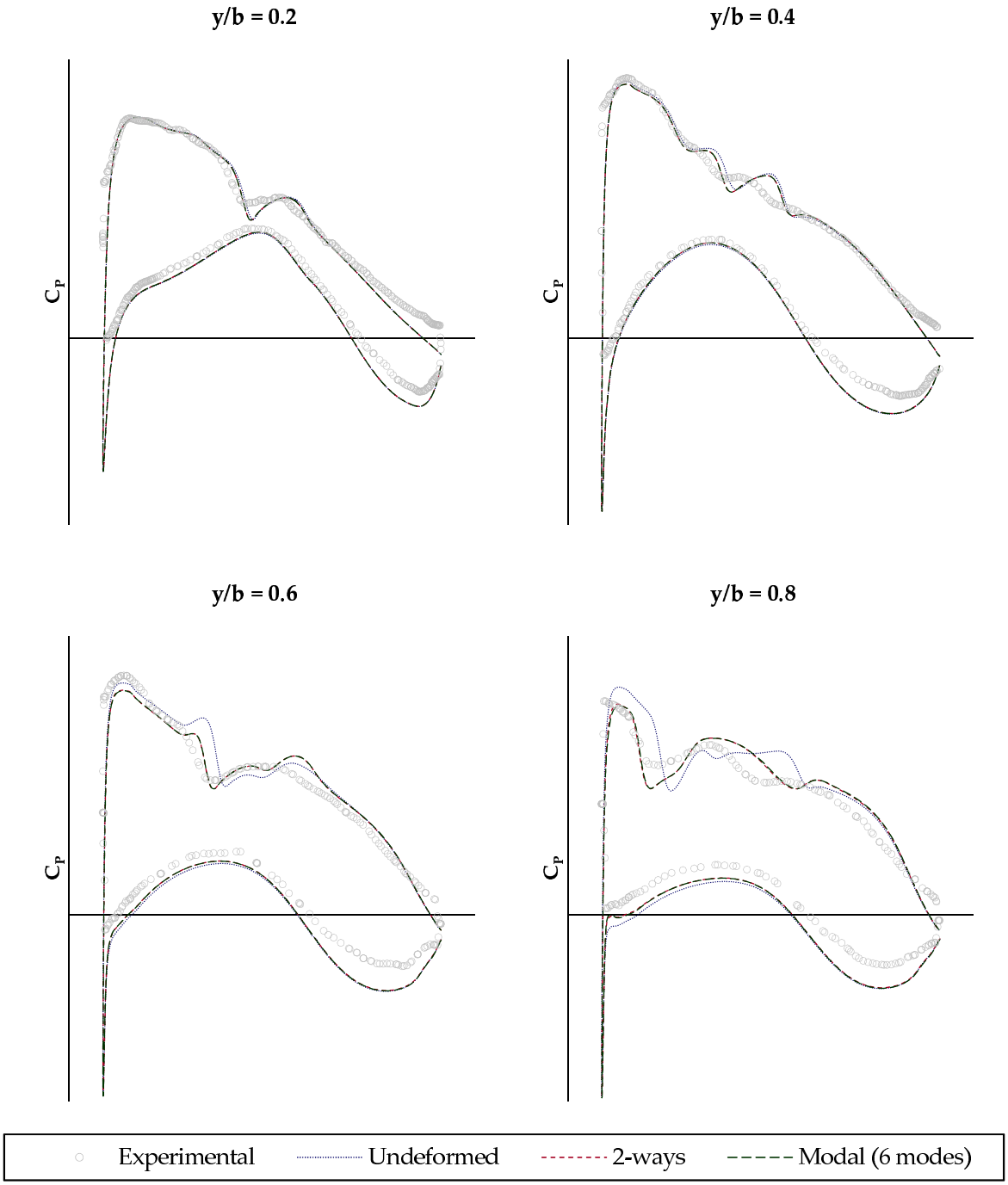

Figure A.4: *P1XX - C_P comparison at the four monitored wing stations.*

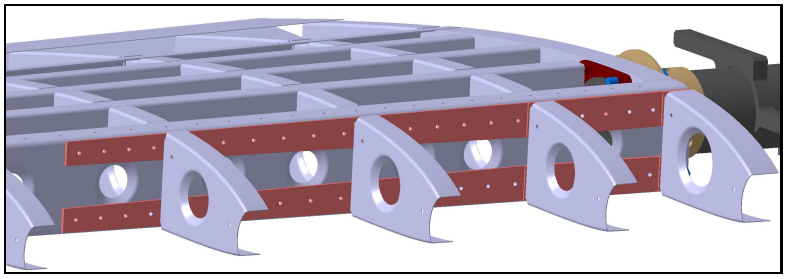

Figure A.5: *RIBES - front spar thickening.*

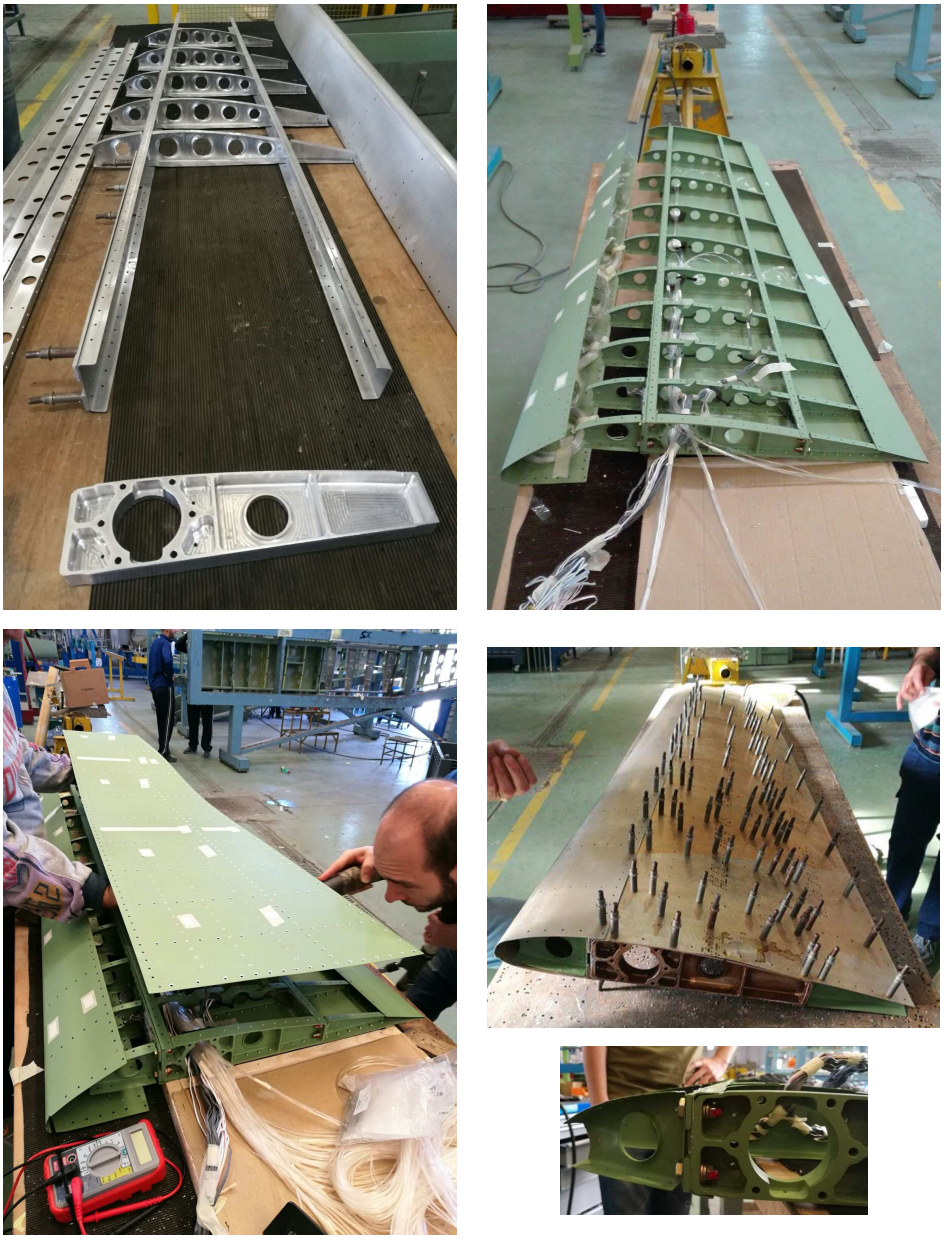

Figure A.6: *RIBES - assembly of the model.*

Figure A.7: *RIBES - assembly of upper panel.*

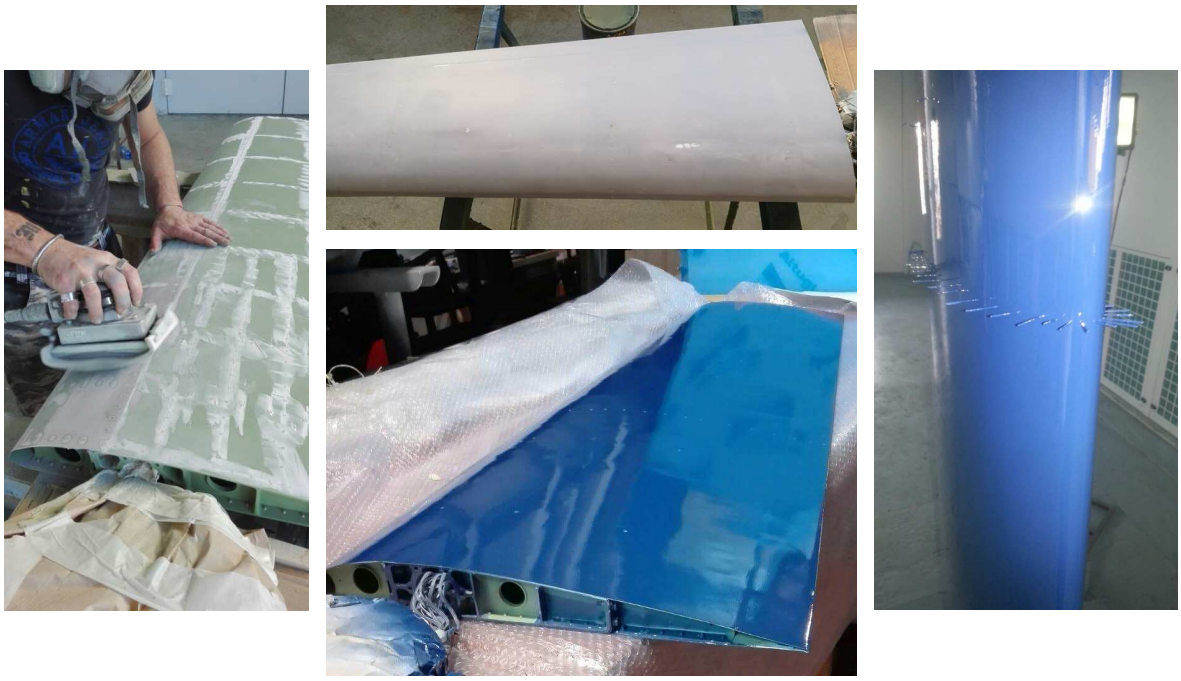

Figure A.8: *RIBES - final model surface finishing.*

Table A.1: *RIBES - list of model elements and dimensions.*

List of wing elements (material: Al 2024T3)		
Number of elements	**component**	**thickness**
		mm
1	front spar	1
1	rear spar	1
2	front spar thickening	4
8	wing box ribs	0.6
1	root wing box rib	6
9	leading edge ribs	0.6
9	trailing edge ribs	0.6
1	tip rib	0.6
3	stringers	0.6
1	skin leading edge	0.6
1	skin upper box	0.6
1	skin lower box	0.6
1	skin trailing edge	0.4
List of junctions elements		
Number of elements	**component**	**dimension**
		mm
800	CherryMAX rivets	
8	linchpins and nuts	4.8
2	linchpins and nuts	7.92

Figure A.9: *RIBES - reconstruction measurement instrument.*

Table A.2: *RIBES - Pressure taps locations and number.*

Section	y *mm*	y/b *%*	chord *mm*	pressure taps
1	160	10	582	4
2	450	28.1	549	4
3	600	37.5	533	39
4	990	61.9	488	4
5	1200	75	465	26
6	1500	93.8	431	4

Figure A.10: *RIBES - pressure tubes installation.*

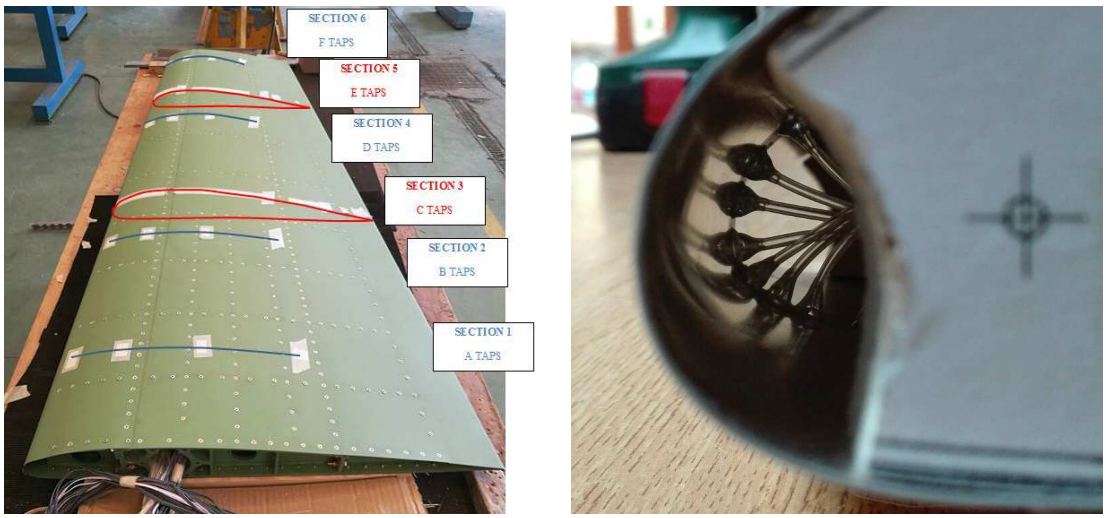

Figure A.11: *RIBES - pressure taps locations.*

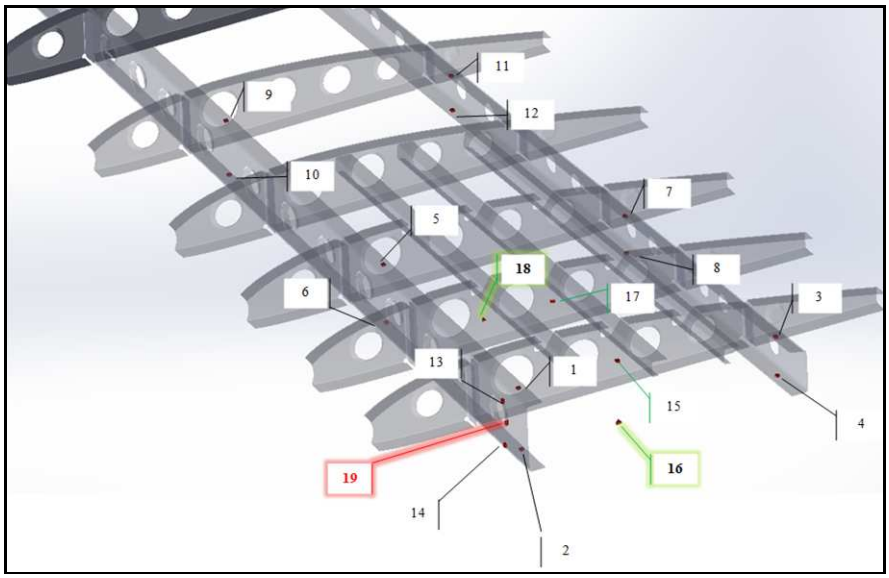

Figure A.12: *RIBES - map of strain gauges position.*

Table A.3: *RIBES - List of strain gauges.*

ID	position	type	y *mm*
1	front spar	unidirectional	35.5
2	front spar	unidirectional	35.5
3	rear spar	unidirectional	35.5
4	rear spar	unidirectional	35.5
5	front spar	unidirectional	310
6	front spar	unidirectional	310
7	rear spar	unidirectional	297
8	rear spar	unidirectional	297
9	front spar	unidirectional	600
10	front spar	unidirectional	600
11	rear spar	unidirectional	598
12	rear spar	unidirectional	598
13	front spar thickening	unidirectional	35.5
14	front spar thickening	unidirectional	35.5
15	upper skin	unidirectional	35.5
16	lower skin	**rosette** three signals	35.5
17	upper skin	unidirectional	169
18	upper skin	**rosette** three signals	169
19	front spar	**rosette** three signals	35.5

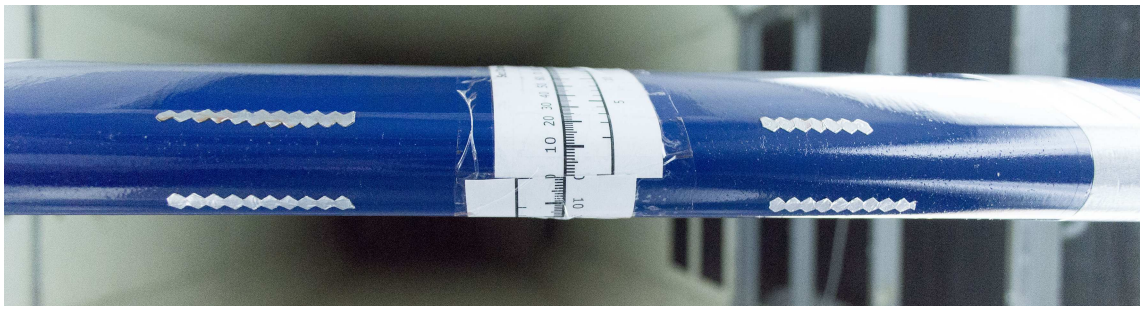

Figure A.13: *RIBES - installation of transition trips.*

Figure A.14: *RIBES - wing tip displacement measurement.*

Figure A.15: *RIBES - balance inclination measurement.*

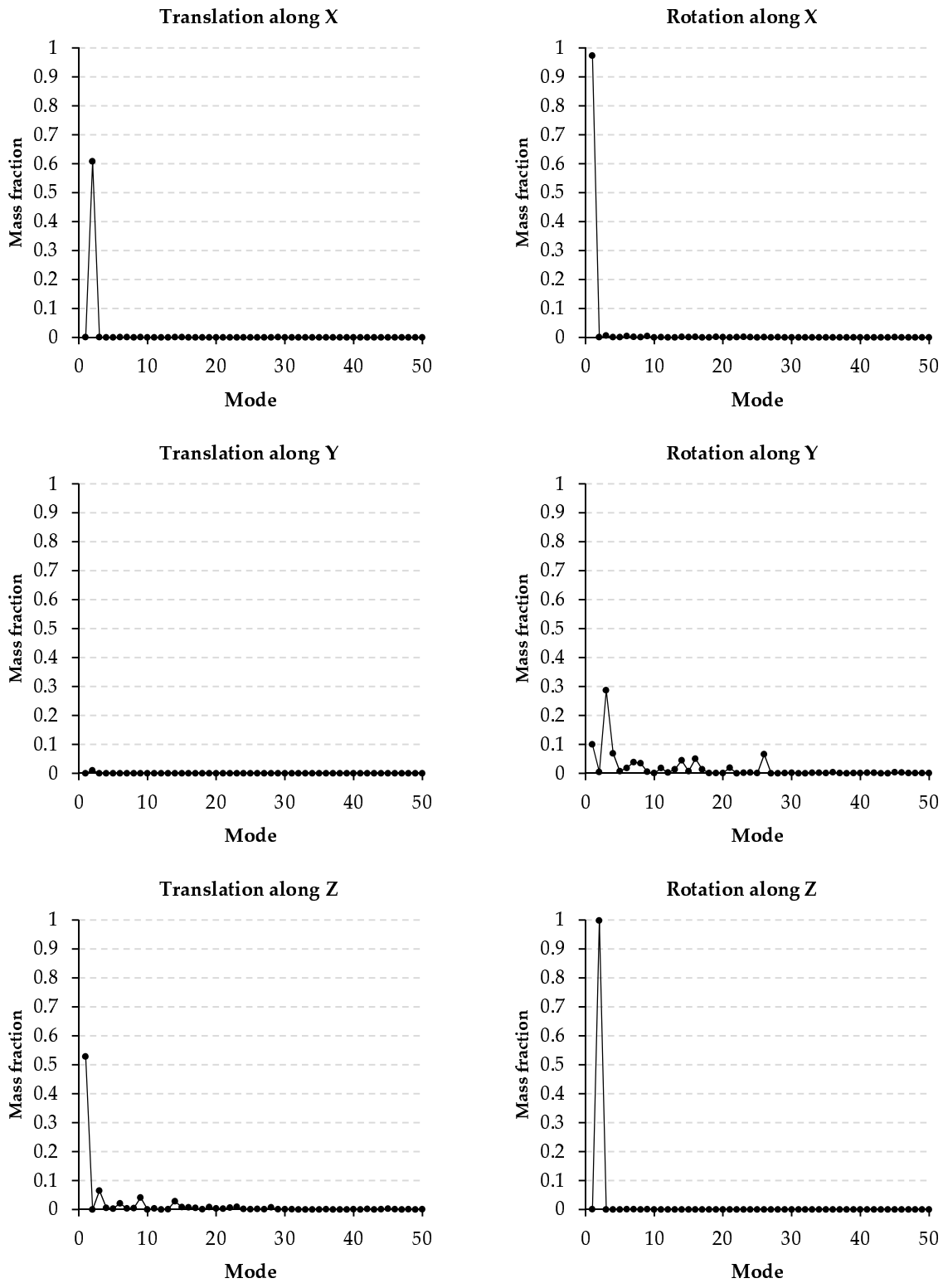

Figure A.16: *RIBES - modal mass fraction of first 50 modes.*

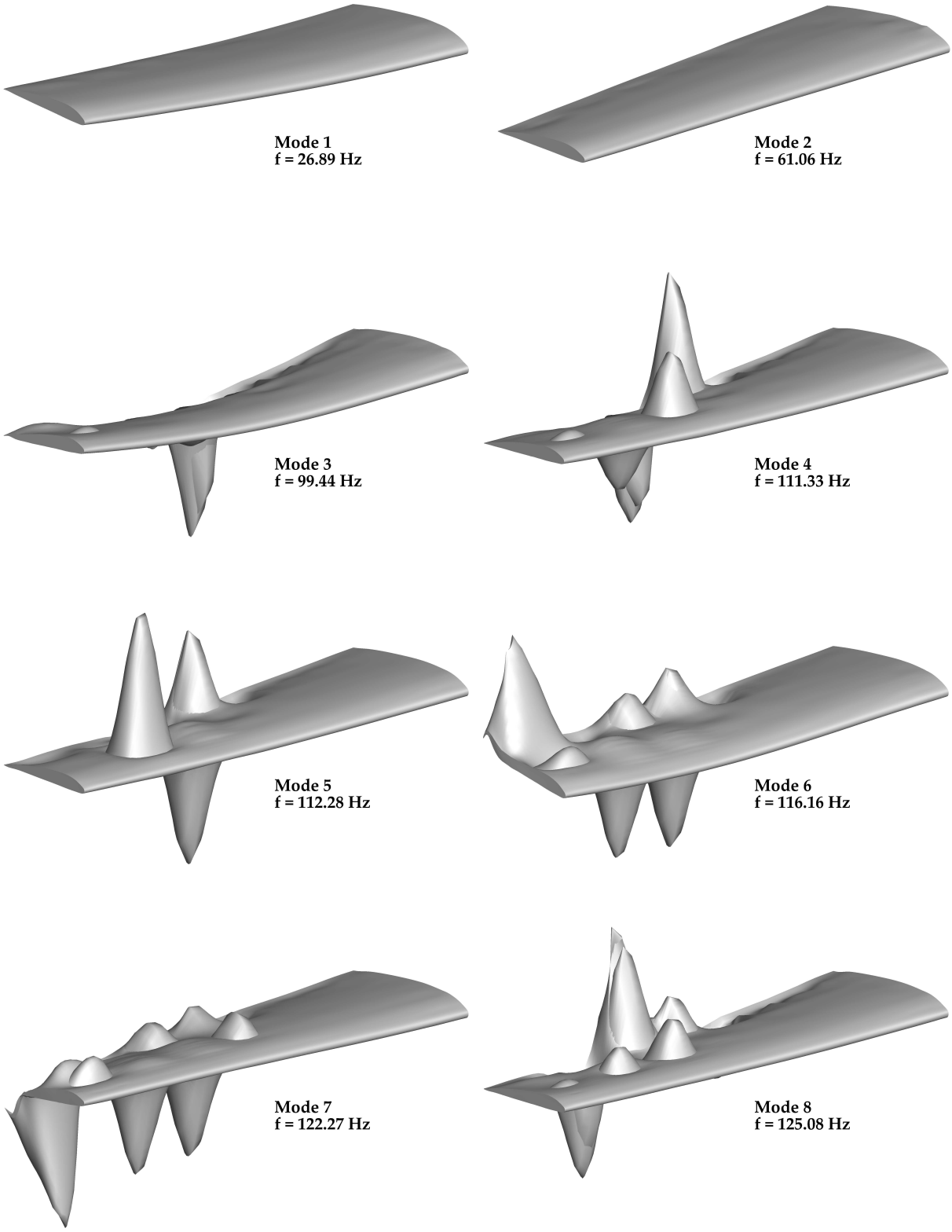

Figure A.17: *RIBES - first eight vibrating modal shapes of the wing.*

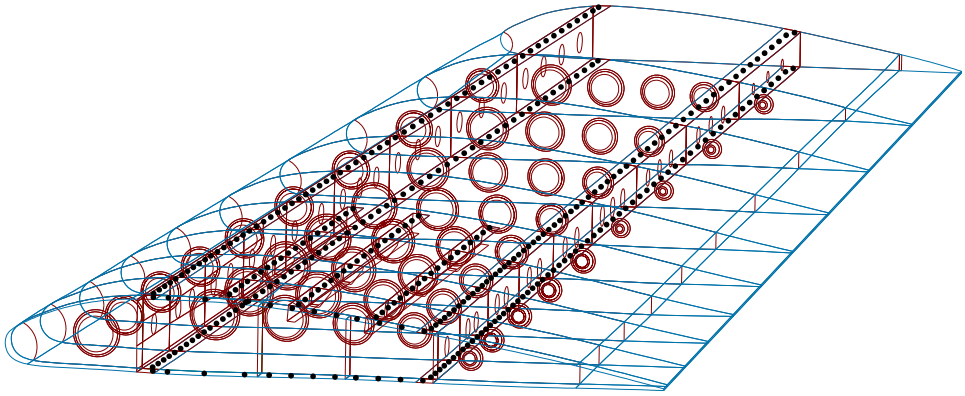

Figure A.18: *RIBES - positions of the FEM modelled junction points.*

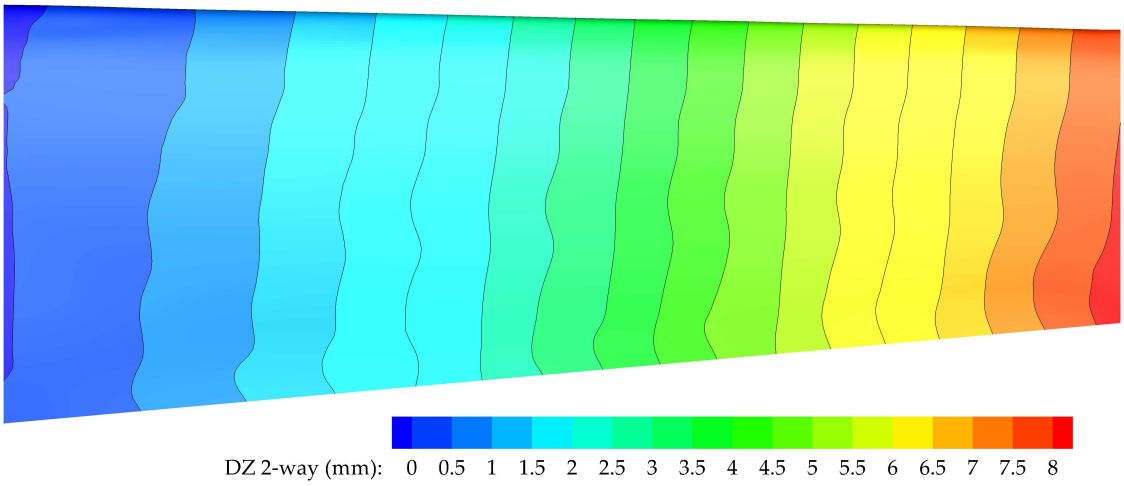

Figure A.19: *RIBES - displacement of the wing computed by 2-way analysis.*

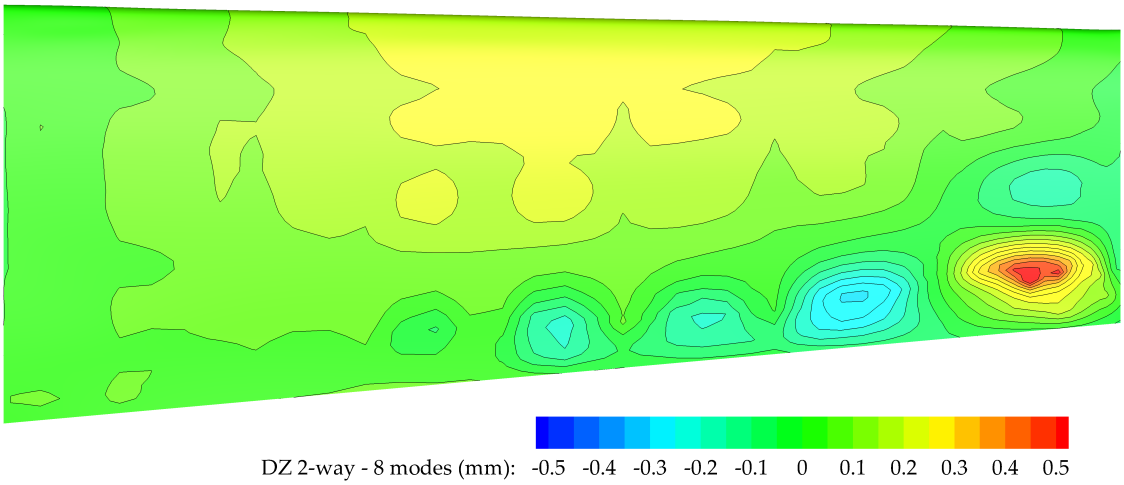

Figure A.20: *RIBES - geometric differences between elastic models solutions.*

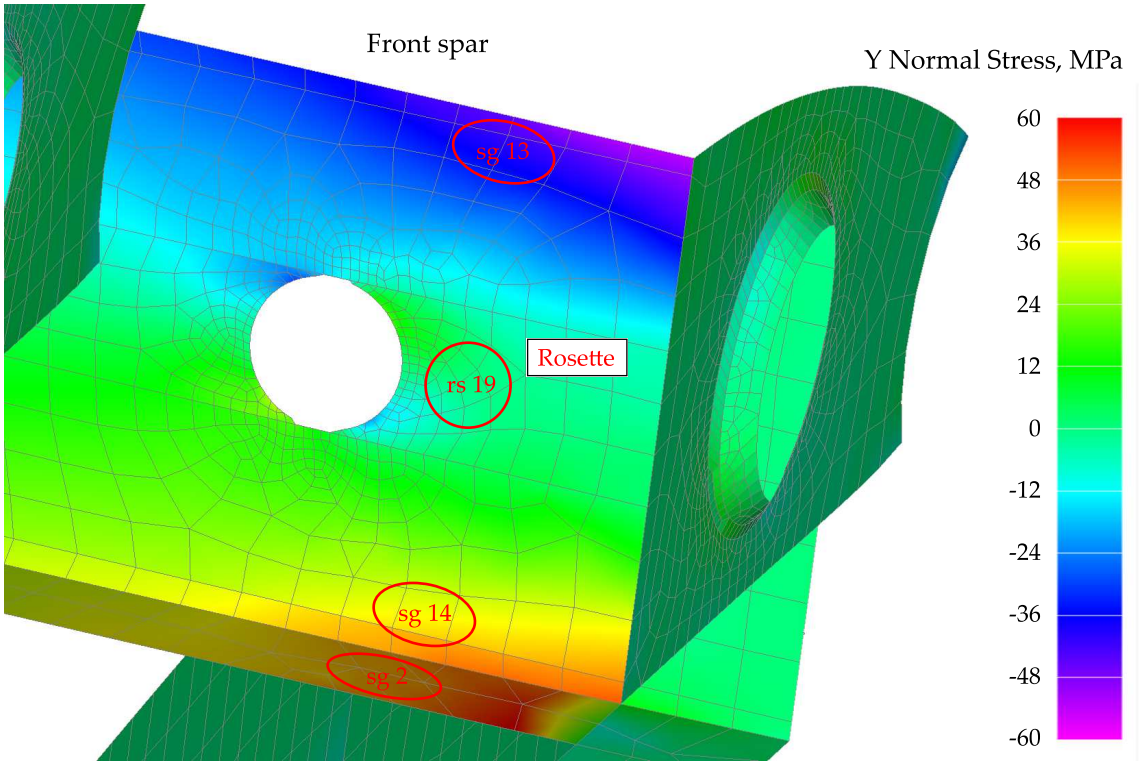

Figure A.21: *RIBES - 2-way FEM solution (strain gauges 2, 13, 14 and rosette 19).*

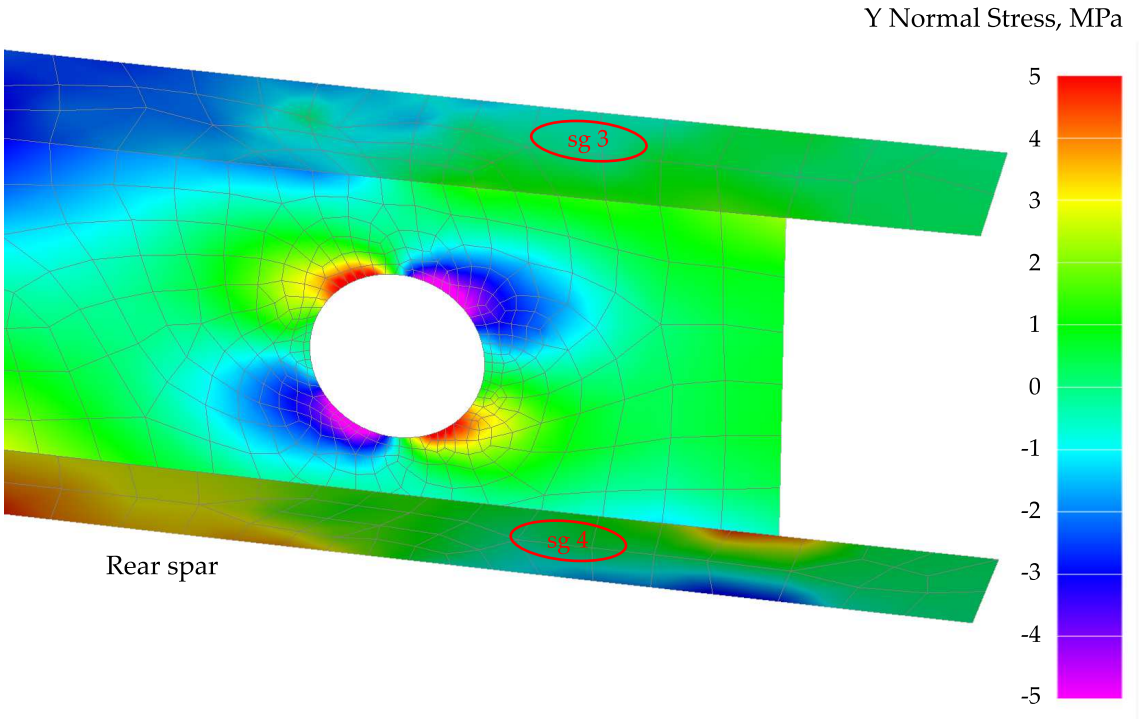

Figure A.22: *RIBES - 2-way FEM solution (strain gauges 3 and 4).*

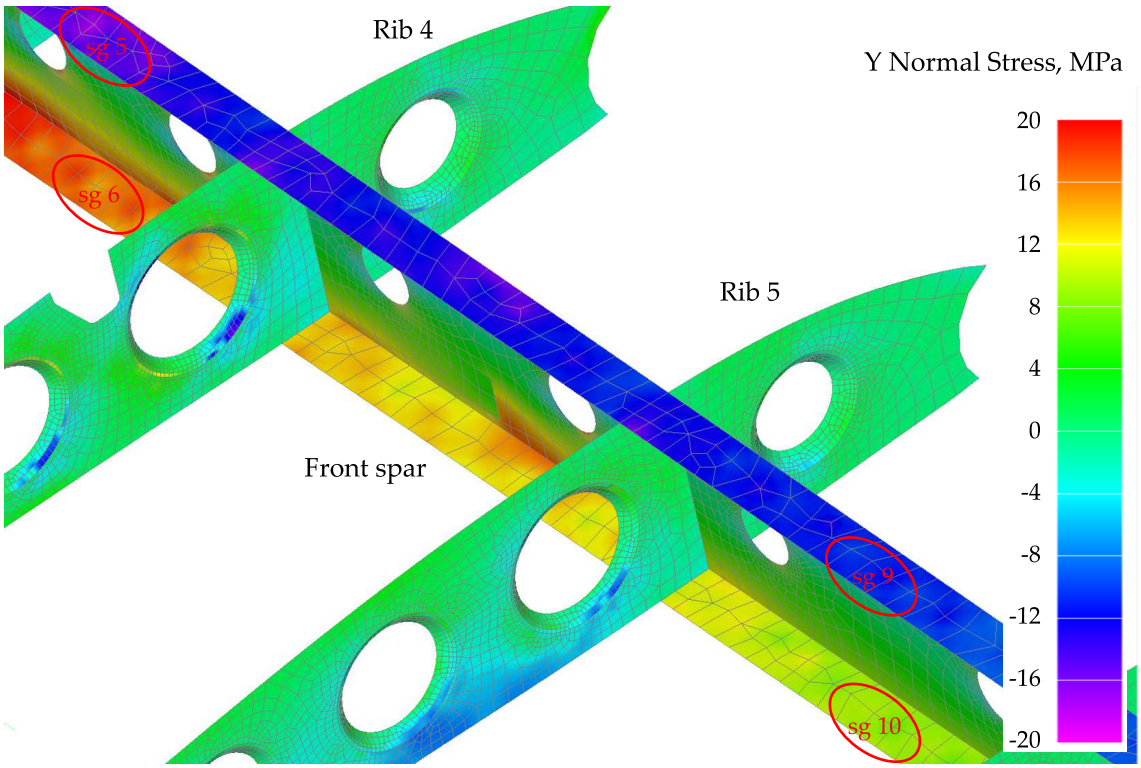

Figure A.23: *RIBES - 2-way FEM solution (strain gauges 5, 6, 9 and 10).*

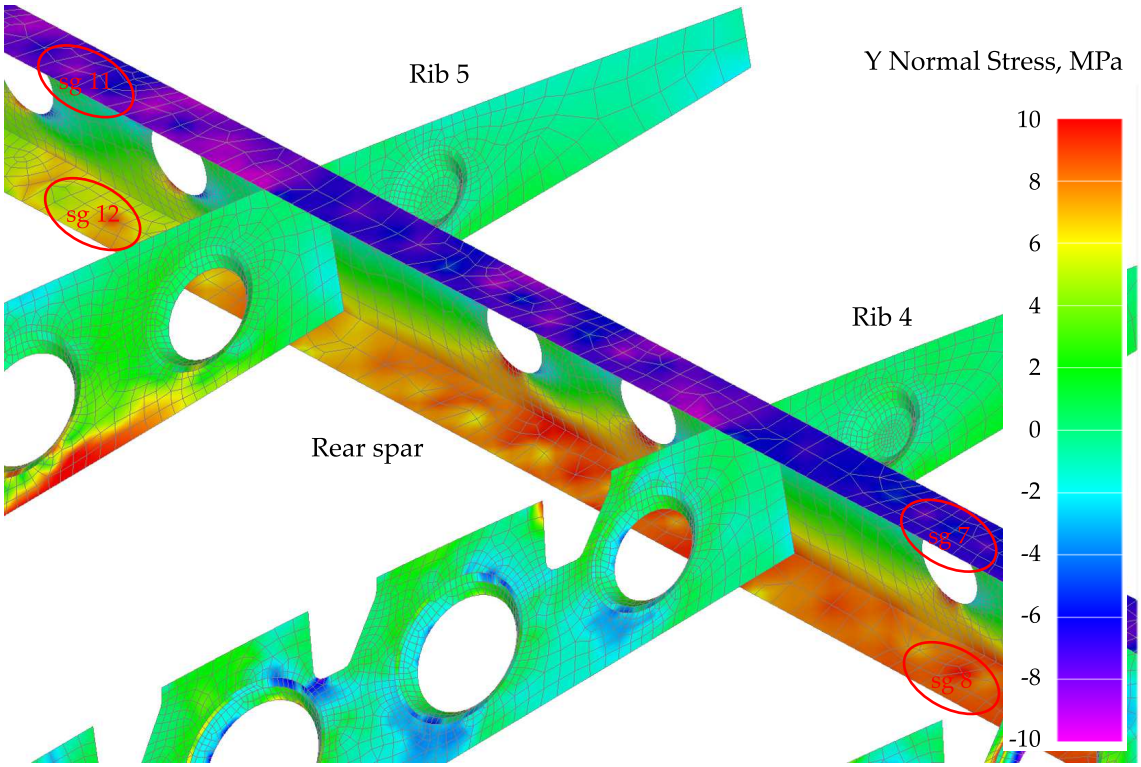

Figure A.24: *RIBES - 2-way FEM solution (strain gauges 7, 8, 11 and 12).*

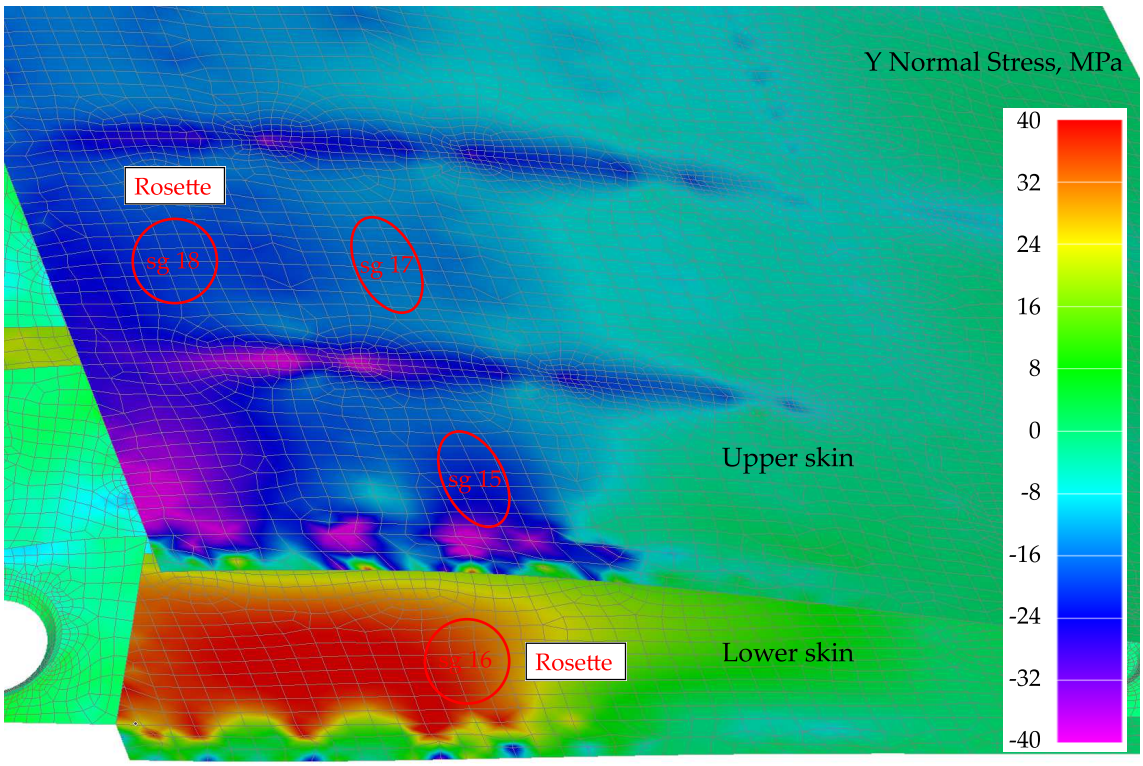

Figure A.25: *RIBES - 2-way FEM solution (strain gauges 15, 17 and rosettes 16, 18).*

Bibliography

[1] Arthur R. Collar. *The first fifty years of aeroelasticity*, chapter 5, pages 12–20. Aerospace, February 1978.

[2] Martin Carlsson. *Design and Testing of Flexible Aircraft Structures*. PhD thesis, Royal Institute of Technology (KTH), Stockholm, Sweden, 2004.

[3] Jan R. Wright and Jonathan E. Cooper. *Introduction to Aircraft Aeroelasticity and Loads*. Aerospace Series. John Wiley & Sons Ltd, The Atrium, Southern Gate, Chichester, West Sussex PO19 8SQ, England, 2007.

[4] Roger W. Pratt. *Flight control systems: practical issues in design and implementation*. Number 57 in IEE control engineering series. Institution of Electrical Engineers, Stevenage, United Kingdom, 2000.

[5] Anthony H.G. Fokker. *Flying Dutchman: The Life of Anthony Fokker*. Ayer Publishing Co., June 1931.

[6] Theodor Theordsen. General theory of aerodynamic instability and the mechanism of flutter. Report 496, NACA, 1936.

[7] Rodney H. Ricketts. Experimental aeroelasticity history, status and future in brief. Technical Memorandum 102651, NASA, April 1990.

[8] Joyce L. Deyoung. Historical evolution of vortex-lattice methods. Conference Paper 76N28164, NASA, January 1976.

[9] Sven G. Hedman. Vortex lattice method for calculation of quasi steady state loadings on thin elastic wings. Repot 105, Aeronautical research institute of Swedew (FFA), Stockholm, Sweden, 1966.

[10] Gene Hou, Jin Wang, and Anita Layton. Numerical methods for fluid-structure interaction - a review. *Communications in Computational Physics*, 12(2):337–377, August 2012.

[11] William B. Kemp Jr. Definition and application of longitudinal stability derivatives for elastic airplanes. Technical Note D-6629, NASA, March 1972.

[12] Edward Albano and William. P. Rodden. A doublet-lattice method for calculating lift distributions on oscillating surfaces in subsonic flows. *AIAA Journal*, 7(2):279–285, February 1969.

[13] Thiemo M. Kier. Comparison of unsteady aerodynamic modelling methodologies with respect to flight loads analysis. In *AIAA Atmospheric Flight Mechanics Conference and Exhibit*, San Francisco, California, USA, 15-18 August 2005.

[14] R. Palacios, H. Climent, A. Karlsson, and B. Winzell. Assessment of strategies for correcting linear unsteady aerodynamics using CFD or test results. In Springer, editor, *CEAS/AIAA/AIAE International Forum on Aeroelasticity and Structural Dynamics*, volume 2, pages 195–210, Madrid, Spain, 2001.

[15] Emiliano Costa. *Advanced FSI analysis within ANSYS FLUENT by means of a UDF implemented explicit large displacements FEM solver*. Ph.D. thesis in mechanical engineering, University of Rome "Tor Vergata", Academic Year 2011/2012. Cycle XXIV.

[16] A. Viré, J. Xiang, F. Milthaler, P. E. Farrell, M. D. Piggott, J. P. Latham, D. Pavlidis, and C. C. Pain. Modelling of fluid-solid interactions using an adaptive mesh fluid model coupled with a combined finite-discrete element model. *Ocean Dynamics*, 62(10):1487–1501, December 2012.

[17] Axelle Viré, Jiansheng Xiang, Matthew Piggott, Colin Cotter, and Christopher Pain. Towards the fully-coupled numerical modelling of floating wind turbines. In *10^{th} Deep Sea Offshore Wind R&D Conference*, volume 35 of *Energy Procedia*, pages 43–51, Trondheim, Norway, 24-25 January 2013. Elsevier.

[18] Franco Mastroddi, Paolo Castronovo, Fulvio Stella, and Marco Evangelos Biancolini. Assessment and development of a ROM for linearized aeroelastic analyses of aerospace vehicles. *accepted for publication on CEAS Aeronautical Journal*, 2017.

[19] Matthew F. Barone and Jeffrey L. Payne. Methods for simulation-based analysis of fluid-structure interaction. Report SAND2005-6573, Sandia National Laboratories, October 2005.

[20] Sukumar Chakravarthy. Importance of accuracy in CFD simulations. In *6^{th} BETA CAE International Conference*, Thessaloniki, Greece, 10-12 June 2015.

[21] Jan B. Vos, Arthur Rizzi, Denis Darracq, and Ernst H. Hirschel. Navier–Stokes solvers in european aircraft design. *Progress in Aerospace Sciences*, 38(8):601–697, November 2002.

[22] Jamshid A. Samareh. Survey of shape parameterization techniques for high-fidelity multidisciplinary shape optimization. *AIAA Journal*, 39(5):877–884, May 2001.

[23] Yannick Rousseau, Igor Men'shov, and Yoshiaki Nakamura. Morphing-based shape optimization in computational fluid dynamics. *Transactions of the Japan Society for Aeronautical and Space Sciences*, 50(167):41–47, 2007.

[24] Arif Masud, Manish Bhanabhagvanwala, and Rooh A. Khurram. An adaptive mesh rezoning scheme for moving boundary flows and fluid-structure interaction. *Computers & Fluids*, 36(1):77–91, January 2007. Challenges and Advances in Flow Simulation and Modeling.

[25] Aukje de Boer, Martijn S. van der Schoot, and Hester Bijl. Mesh deformation based on radial basis function interpolation. *Computers & Structures*, 85(11-14):784–795, June-July 2007. Fourth MIT Conference on Computational Fluid and Solid Mechanics.

[26] Stefan Jakobsson and Olivier Amoignon. Mesh deformation using radial basis functions for gradient-based aerodynamic shape optimization. *Computers & Fluids*, 36(6):1119–1136, July 2007.

[27] A.H. van Zuijlen, A. de Boer, and H. Bijl. Higher-order time integration through smooth mesh deformation for 3D fluid-structure interaction simulations. *Journal of Computational Physics*, 224(1):414–430, May 2007.

[28] Marco E. Biancolini. Mesh morphing accelerates design optimization. *ANSYS Advantage*, 4(1), 2010.

[29] E.M. Papoutsis-Kiachagias, M. Andrejašič, S. Porziani, C. Groth, D. Eržen, M.E. Biancolini, E. Costa, and K.C. Giannakoglou. Combining an RBF–based morpher with continuous adjoint for low–speed aeronautical optimization applications. In *VII ECCOMAS Congress*, Crete Island, Greece, 5-10 June 2016.

[30] Marco E. Biancolini. Fluid structure interaction (FSI) with RBF morph: a generic formula 1 front end. In *International CAE conference*, Verona, Italy, 20-21 October 2011. EnginSoft.

[31] Ignazio M. Viola, Marco E. Biancolini, Matthieu Sacher, and Ubaldo Cella. A CFD-based wing sail optimisation method coupled to a VPP. In *5th High Performance Yacht Design Conference*, Auckland, New Zealand, 10-12 March 2015.

[32] Marco Evangelos Biancolini. *Handbook of Research on Computational Science and Engineering: Theory and Practice*, chapter Mesh Morphing and Smoothing by Means of Radial Basis Functions (RBF): A Practical Example Using Fluent and RBF Morph, pages 347–380. IGI Global, December 2012.

[33] M. Bernaschi, A. Sabellico, G. Urso, E. Costa, S. Porziani, F. Lagasco, C. Groth, U. Cella, M. E. Biancolini, D. H. Kapsoulis, V. G. Asouti, and K. C. Giannakoglou. The RBF4AERO benchmark technology platform. In *VII ECCOMAS Congress*, Crete Island, Greece, 5-10 June 2016.

[34] M. Andrejašič, A. Eržen, E. Costa, S. Porziani, M. E. Biancolini, and C. Groth. A mesh morphing based FSI method used in aeronautical optimization applications. In *VII ECCOMAS Congress*, Crete Island, Greece, 5-10 June 2016.

[35] Emiliano Costa, Marco E. Biancolini, Corrado Groth, Giorgio Travostino, and Gabriele D'Agostini. Reliable mesh morphing approach to handle icing simulations on complex models. In *4th EASN Association International Workshop on Flight Physics and Aircraft Design*, Aachen, Germany, 27-29 October 2014.

[36] D. H. Kapsoulis, V. G. Asouti, K. C. Giannakoglou, S. Porziani, E. Costa, C. Groth, U. Cella, and M. E. Biancolini. Evolutionary aerodynamic shape optimization through the RBF4AERO platform. In *VII ECCOMAS Congress*, Crete Island, Greece, 5-10 June 2016.

[37] M. Andrejašič, A. Eržen, E. Costa, S. Porziani, E.M. Papoutsis-Kiachagias, D. H. Kapsoulis, V. G. Asouti, K. C. Giannakoglou, U. Cella, C. Groth, and M. E. Biancolini. Adjoint and EAs based aerodynamic shape optimization on industrial test cases using RBF4AERO platform. In *4th OpenFOAM User conference*, Cologne, Germany, 11-13 October 2016.

[38] Ubaldo Cella, Marco E. Biancolini, Corrado Groth, Andrea Chiappa, and Domiziano Beltramme. Development and validation of numerical tools for FSI analysis and structural optimization: the EU "RIBES" project status. In *44th AIAS National congress*, number AIAS 2015-562, Messina, Italy, 2-5 September 2015.

[39] Martin D. Buhmann. *Radial Basis Functions: Theory and Implementations*. Cambridge monographs on applied and computational mathematics. Cambridge University Press, 2004.

[40] Suresh K. Lodha and Richard Franke. *Scattered Data Interpolation: Radial Basis and Other Methods*, chapter 16, pages 389–404. Handbook of Computer Aided Geometric Design. North Holland, 2002.

[41] Leonard Meirovitch. *Fundamentals of vibrations*. Waveland Press, Inc, 2010.

[42] Rodney H. Ricketts and Robert V. Doggett Jr. Wind-tunnel experiments on divergence of forward-swept wings. Technical Paper 1684, NASA, Langley Research Center, Hampton, Virginia (US), August 1980.

[43] Cornelius Lanczos. An iteration method for the solution of the eigenvalue problem of linear differential and integral operators. *Journal of Research of the National Bureau of Standards*, 45(4):255–282, October 1950. Research Paper 2133.

[44] Giancarlo Genta. *Vibration Dynamics and Control*. Mechanical Engineering Series. Springer, 2009.

[45] Xiangmin Jiao and Michael T. Heath. Common-refinement-based data transfer between non-matching meshes in multiphysics simulations. *International Journal for Numerical Methods in Engineering*, 61(14):2402–2427, October 2004.

[46] R.K. Jaiman, X. Jiao, P.H. Geubelle, and E. Loth. Conservative load transfer along curved fluidsolid interface with non-matching meshes. *Journal of Computational Physics*, 218(1):372–397, October 2006.

[47] Jamshid Samareh. Discrete data transfer technique for fluid-structure interaction. In *18th AIAA Computational Fluid Dynamics Conference*, Miami, Florida (US), 25-28 June 2007.

[48] Gene Hou and Arunkumar Satyanarayana. Analytical sensitivity analysis of a static aeroelastic wing. In *8th Symposium on Multidisciplinary Analysis and Optimization (AIAA)*, number AIAA 2000-4824, Long Beach,California (US), 6-8 September 2000.

[49] Xiaogang Jin, Hanqiu Sun, and Qunsheng Peng. Subdivision interpolating implicit surfaces. *Computers & Graphics*, 27(5):763–772, October 2003.

[50] Ivo M. Babuška and Jens M. Melenk. The partition of unity method. *International Journal for Numerical Methods in Engineering*, 40(4):727–758, February 1997.

[51] Todd Rowland. Partition of unity. From MathWorld - A Wolfram Web Resource.

[52] Josef Ballmann. Experimental analysis of high reynolds number structural dynamics in ETW. In *46th AIAA Aerospace Sciences Meeting and Exhibit*, number AIAA 2008-841, Reno, Nevada (US), 7-10 January 2008.

[53] Matthew Staten, Steven Owen, Suzanne Shontz, Andrew Salinger, and Todd Coffey. A comparison of mesh morphing methods for 3D shape optimization. In *20th International Meshing Roundtable*, Paris, France, 23-26 October 2011.

[54] Marco E. Biancolini, Emiliano Costa, Ubaldo Cella, Corrado Groth, Gregor Veble, and Matej Andrejašič. Glider fuselage-wing junction optimization using CFD and RBF mesh morphing. *Aircraft Engineering and Aerospace Technology*, 88(6):740–752, 2016.

[55] M.E. Biancolini, C. Biancolini, E. Costa, D. Gattamelata, and P.P. Valentini. Industrial application of the meshless morpher RBF morph to a motorbike windshield optimisation. In *4th European Automotive Simulation Conference*, Munich, Germany, 6-7 July 2009.

[56] Ubaldo Cella, Corrado Groth, and Marco E. Biancolini. *Geometric Parameterization Strategies for shape Optimization Using RBF Mesh Morphing*, pages 537–545. Lecture Notes in Mechanical Engineering. Springer International Publishing, September 2017.

[57] Marco E. Biancolini. RBF morph mesh morphing ACT extension for ANSYS Mechanical. In *Automotive Simulation World Congress*, Tokyo, Japan, 9-10 October 2014.

[58] Thomas C. S. Rendall and Christian B. Allen. Efficient mesh motion using radial basis functions with data reduction algorithms. *Journal of Computational Physics*, 228(17):6231–6249, September 2009.

[59] Thomas C. S. Rendall and Christian B. Allen. Reduced surface point selection options for efficient mesh deformation using radial basis functions. *Journal of Computational Physics*, 229(8):2810–2820, April 2010.

[60] *RBF Morph for FLUENT: User's Guide*, 1.72 edition, September 2016.

[61] *RBF Morph - Modelling Guidelines and Best Practices Guide*, 1.72 edition, September 2016.

[62] Markus Ritter. Static and forced motion aeroelastic simulations of the HIRENASD wind tunnel model. In *53rd AIAA/ASME/ASCE/AHS/ASC Structures, Structural Dynamics and Materials Conference*, number 1633, Honolulu, Hawaii (US), 23-26 April 2012.

[63] P. Chwalowski, J. Heeg, M. Dalenbring, A. Jirasek, and M Ritter. Collaborative HiReNASD analyses to eliminate variations in computational results. In *International Forum on Aeroelasticity and Structural Dynamics*, Bristol, United Kingdom, 24-26 June 2013.

[64] Marco E. Biancolini, Ubaldo Cella, Corrado Groth, and Massimiliano Genta. Static aeroelastic analysis of an aircraft wind-tunnel model by means of modal RBF mesh updating. *ASCE's Journal of Aerospace Engineering*, 29(6), July 2016.

[65] Giovanni Paolo Reina. Theoretical investigation of wing aeroelastic response after store separation. Master's thesis, University of Naples "Federico II", December 2013.

[66] T. Streit, K. H. Horstmann, G. Schrauf, S. Hein, U. Fey, Y. Egami, J. Perraud, I. S. El Din, U. Cella, and J. Quest. Complementary numerical and experimental data analysis of the ETW telfona pathfinder wing transition tests. In *49th AIAA Aerospace Sciences Meeting including the New Horizons Forum and Aerospace Exposition*, number 881, Orlando, Florida (US), 4-7 January 2011.

[67] Yves Le Sant. Overview of the self-illumination effect applied to pressure sensitive paint applications. In *19th International Congress on Instrumentation in Aerospace Simulation Facilities*, number 01CH37215, pages 159–170, Cleveland, Ohio (US), 27-30 August 2001.

[68] Ubaldo Cella and Marco E. Biancolini. Aeroelastic analysis of aircraft wind-tunnel model coupling structural and fluid dynamic codes. *AIAA Journal of Aircraft*, 49(2):407–414, March-April 2012.

[69] ANSYS, Inc. *ANSYS Fluent Theory Guide*, release 17.2 edition.

[70] T. H. Shih, W. W. Liou, A. Shabbir, Z. Yang, and J. Zhu. A new $k-\epsilon$ eddy viscosity model for high reynolds number turbulent flows: Model development and validation. Technical Memorandum 106721, NASA, August 1994.

[71] M. Wolfshtein. The velocity and temperature distribution in one-dimensional flow with turbulence augmentation and pressure gradient. *International Journal of Heat and Mass Transfer*, 12(3):301–318, March 1969.

[72] Jan Roskam and Chuan-Tau Edward Lan. *Airplane Aerodynamics and Performance*. Design, Analysis and Research Corporation (DARcorporation), Lawrence, Kansas 66044 (US), 1997.

[73] Civil Aviation Authority, London. *British Civil Airworthiness Requirements. Section D-Aeroplanes*, October 1976.

[74] T.H.G. Megson. *Aircraft Structures for Engineering Students*. Elsevier, Boston (US), 5 edition, 2012.

[75] John A. Nelder and Roger Mead. A simplex method for function minimization. *The Computer Journal*, 7(4):308–313, 1965.